Universitat Politècnica de Catalunya

and

CERN

Doctoral Program in Nuclear Engineering and Ionizing Radiations

Comparative study of Final Focus Systems for CLIC and other luminosity enhancement studies for future linear colliders

Dissertation presented for the degree of Philosophiae Doctor (PhD) in Physics

Author:
Héctor García Morales

Supervisors:
Dr. Rogelio Tomás García
Dr. Yuri Kubyshin

September 12, 2014
Barcelona

A la memòria del profe Jesús.

Acknowledgments

After three years there have been so many people that helped me in one way or another that it is difficult to not forget anybody. I will do my best.

First of all I would like to thank Dr. Rogelio Tomás for his constant supervision and patience. His high activity is sometimes stressful but very contagious, and one becomes very active as well.

I would like to thank also Dr. Daniel Schulte for providing me a very wide view of the linear accelerators, and also for supporting my application to the CERN PhD program.

Also I want to thank Dr. Yuri Kubyshin for providing me the unique opportunity to collaborate with CERN and for supervising my work from my home institute, the Universitat Politècnica de Catalunya. I am also very grateful to Edu Marin for his unconditional help during my first weeks at CERN.

Out of the proper academic area is where I found the greatest support. To my lunch time mates that at 12:45 knocked on the door of my office to enjoy of a homemade meal while trying to solve the problems of the world. Marga, Patri, Maria, Sylvia, Fátima, Pablo, Alejandro, Alberto, Jaume, Raul, Carlos and Javi. Specially, I would like to thank Octavio from who I learned much more than in the rest of my life about life itself.

Also I would like to mention three more people with who I shared some of the most special moments of the last three years. First of all, I want to be present in this thesis the names of my two California riders: Korina and Alexander. One week sharing car and room in the west coast of the USA, sorting cows in the middle of the dark road to Grand Canyon and eating the best hamburgers of the USA in Hollywood boulevard, suggestion of a homeless. Also mention Juergen, with who I reached the top of Japan after climbing the mount Fuji off season and missing the way back to the starting point.

Some weeks ago, I counted the number of people with who I shared the apartment and I got the non negligible number of 11. From all of them I learned something, sometimes not really good, usually very good. Most of them have a little space reserved on my mind, specially: Alberto, Silvia, Juan, Elena, Juanjo, Xumeu and Quim. Thank you all for sharing place and for not leaving the kitchen so dirty.

I would like to thank also my football team, CERN XV. Those days in which you are stressed by the never ending simulations you are looking forward to forget it for a while and to run and play and, sometimes, win.

I am also very grateful to my home town, Sant Joan Despí, that has provided me the opportunity to spread science among young and old people organizing conferences for me.

Very important is also the role of the family. They make you feel very proud of all the activities you realize. Their constant curiosity about what is going on in science today reinforces your skills in science communication. Also I am very grateful to them for coming to visit Switzerland, for being always ready

to share a fondue at home and to do not care about sleeping in the sofa.

Finally, very special thanks to Georgina, for her constant support and for opening my eyes from outside. Without her some moments had been much worse to overcome. We have demonstrated that everything is possible. These years have set a starting point of a life together.

Can Coll de Pincaró
22nd of March 2014

List of publications

The contents of this thesis and preliminary studies can be found in the following publications as well as some other studies performed in parallel to the main subject of the thesis:

1. H.Garcia and R.Tomas, "Final-focus systems for multi-TeV linear colliders", Phys. Rev. ST Accel. Beams 17, 101001 (2014).
2. ATF2 collaboration, "Experimental validation of a novel compact focusing scheme for future energy frontier linear lepton colliders", Phys. Rev. Lett. **112**, 034802, (2014).
3. R. Tomas, H. Garcia, Y.I. Levinsen and M. Modena, "CLIC Final Focus Opticsâ, ICFA Beam Dynamics Newsletters, Edited by Toshiyuki Okugi (KEK, Japan). Newsletter No. 61 , August 2013. p. 12-24
4. R. Tomas, H. Garcia, Y.I. Levinsen, M. Modena and E. Marin, "CLIC Beam Delivery Systemâ. ICFA Beam Dynamics Newsletters, No. 62, December 2013, p. 42-60.
5. CLIC collaboration, "CLIC Conceptual Design report", (2012), [arXiv:1209.2543].
6. LHeC collaboration, "LHeC Conceptual Design report", (2012), [arXiv:1206.2913].
7. LHeC collaboration, "A Large Hadron Electron Collider at CERN", (2012), [arXiv:1211.4831].
8. LHeC collaboration, "On the Relation of the LHeC and the LHC", (2012), [arXiv:1211.5102].
9. H.Garcia, R.Tomas, D.Schulte, "Lowering the CLIC IP Horizontal Beta Function", IPAC14, (2014).
10. H.Garcia, R.Tomas, L.Medina, "FCC-ee Final Focus with Chromaticity Correction", IPAC14, (2014).
11. M. Modena, A.V. Aloev, H. Garcia, L. Gatignon, R. Tomas, "Considerations for a QD0 with Hybrid Technology in ILC", IPAC14, (2014).
12. J. Pfingstner, H. Garcia, A. Latina, M. Patecki, D. Schulte, R. Tomas, "Localization of Beam Offset Jitter Sources at ATF2, IPAC14, (2014).
13. Y.I. Levinsen, H. Garcia, G. Giambelli, A. Latina, R. Tomas, J. Snuverink, "Tuning of the Compact Linear Collider Beam Delivery System", IPAC14, (2014).
14. J. Snuverink, J. Barranco, H. Garcia, Y.I. Levinsen, D. Schulte, R. Tomas, "CLIC Final Focus System Alignment and Magnet Tolerances", IPAC13, (2013).
15. H.Garcia, A.Latina, R.Tomas, "Traditional Final Focus System for CLIC", IPAC12, (2012).
16. J.L. Abelleira, H.Garcia, R.Tomas, "Final-Focus Optics for the LHeC Electron Beam Line", IPAC12, (2012).
17. H. Garcia, Yu.A. Kubyshin, T. Aumeyr, G.A. Blair, D. Schulte, F. Stulle, "Laser Wire Emittance Measurement Line at CLIC", IPAC11, (2011).

18. Yu.A. Kubyshin, H. Garcia, E. Marin, D. Schulte, F. Stulle, "Simulations of Emittance Measurement at CLIC", PAC-2011 (2011). In: on-line Proceedings of PAC-2011, pp. 2270-2272

19. H.Garcia, "Emittance measurement station for the RTML section of CLIC", Master thesis, UB-UAB-UPC, (2012).

Some other contributions have been reported to the scientific community via talks or presentations not published in proceedings.

Abstract

The 4^{th} of July 2012 was a milestone date in the history of physics of the last decades. The discovery of the Higgs boson at the ATLAS and CMS experiments thanks to the proton collisions delivered by the LHC not only has provided the missing piece of the Standard Model of particle physics, but most probably, it has opened the door to new physics that remains still hidden today. In order to go beyond in the understanding of the very deep laws of nature, new and more precise experiments are required. One of the alternatives that can unravel these mysteries is the e^+e^- linear collider, being the CLIC (Compact Linear Collider) and the ILC (International Linear Collider) the two referents today. These two machines will collide bunches of electrons and positrons of the order of nanometers transverse size to ensure a high quantity of events during bunch crossing. To reach such small beam sizes, a very strong focusing of the beam is required by means of magnetic lenses. This strong focusing together with the fact that particles inside a bunch have slightly different energies from the nominal energy, makes that each particle is focalized into a different point. Effectively, this effect is translated into a beam size increase and it is called chromaticity. This effect must be corrected in order to reach an acceptable collision rate. The Final Focus System (FFS) comprises the task to focalize the beam at the Interaction Point (IP) and to correct chromaticity. There are two main concepts that carry out this task: the so called traditional or dedicated chromatic correction system and the local chromatic correction system. In this thesis both systems are compared in terms of luminosity performance and how the systems are affected when alignment errors are introduced in the different components of the FFS. We demonstrate that, at high energies, an optimized non-local FFS despite of being longer, is faster to tune and therefore, can deliver more integrated luminosity. The results of these studies have been published on Physical Review Special Topics Accelerators and Beams [1]. The possibility of reducing the horizontal β-function for CLIC at 500 GeV center of mass energy has also been explored. This option would allow a luminosity increase or it would also allow to reduce the bunch charge while keeping the same luminosity. Finally, some studies concerning the optimization of the ILC FFS have been done, including the possibility of implementing the traveling focus scheme and the option of using the CLIC FFS lattice as ILC FFS has been considered showing the advantages and drawbacks of both systems.

Resum

La data del 4 de Juliol del 2012 quedará marcada per sempre a la història de la física com una de les més importants de les darreres dècades. El descobriment del bosó de Higgs als experiments ATLAS i CMS mitjançant col·lisions al LHC ha permés col·locar la peça que faltava al Model Estàndard de la física de partícules però al seu torn, ha obert la porta o trobar nova física que encara avui roman desconeguda. Per tal d'anar més enllà en la comprensió de les lleis fonamentals de la natura, es requereixen experiments encara més precisos que els actuals. Una de les alternatives que podria desvetllar aquests misteris són els colisionadors lineals, entre els quals destaquen CLIC (Compact Linear Collider) i ILC (International Linear Collider). Aquestes futures màquines col·lisionaran dos feixos d'electrons i positrons agrupats en paquets del tamany del nanòmetre per tal de produir una quantitat molt gran de col·lisions per segon. Per tal d'assolir tamanys tan sumament petits, es requereix una forta focalització mitjançant camps magnètics. Però també degut a aquesta forta focalització, i degut a que les partícules de cada paquet tenen una energia que es desvia lleugerament de l'energia nominal, cadascuna d'aquestes partícules es focalitza en un punt diferent al punt d'interacció. Aquest fet es tradueix en un increment efectiu del tamany del feix al punt de col·lisió. Aquest efecte, anomenat cromaticitat, s'ha de corregir per tal de no reduir el nombre de col·lisions per sota del nivell acceptable. El sistema de focalització final (FFS, de l'anglès Final Focus System) s'encarrega de crear aquesta forta focalització a la vegada que es corregeix la cromaticitat del feix. Hi ha dos sistemes principals diferenciats que duen a terma aquesta tasca: l'anomenat sistema de correcció dedicat o tradicional i l'anomenat sistema de correcció local. En aquesta tesis es compara l'efectivitat de cada sistema per CLIC a 3 TeV i 500 GeV d'energia al centre de masses, en termes de luminositat i com es veuen afectats pels diferents errors associats a l'aliniació de tots els components que conformen el FFS. També s'explora l'opció de reduir la funció β horitzontal al punt d'interacció per a CLIC a 500 GeV d'energia al centre de masses. Aquesta opció permetria o bé augmentar la luminositat del sistema o bé reduir la càrrega del feix mantenint la mateixa luminositat. Finalment també es msotren alguns estudis d'optimització del FFS realitzats per ILC, incloent la possibilitat d'introduir un traveling focus mitjançant crab cavities i també es considera emprar el disseny del FFS de CLIC per a ILC i es comparen les avantatges i desavantatges d'ambdós sistemes.

Contents

List of Figures

Chapter 1

Future Linear Colliders

At the moment of writing this thesis, the Large Hadron Collider (LHC) is in its first long shut down after three successful years running at 7 and 8 TeV center of mass (c.o.m.) energy and a delivered integrated luminosity of 23 fb^{-1}. A few years after the first long shutdown running at 13-14 TeV c.o.m. energy, the LHC will be again stopped for a second long shutdown. The LHC final run is planned to be by 2023, where, after a luminosity upgrade (HL-LHC) that will increase its luminosity by a factor 10, its discovery potential will be extended. With the LHC era a new door has been opened for the next generation of large particle accelerators. Several future colliders are currently being discussed, from LHC energy upgrade until lepton linear colliders whose construction might start vin the coming years.

In this chapter we give a brief overview of the physics potential of future lepton linear colliders and describe their main advantages over other possibilities. First of all, we summarize the LHC results up to date and we will relate them to the improvements on precision that an e^+e^- collider could achieve and give a description of the main parts of the machine.

1.1 LHC results: the starting point.

The LHC allows the exploration of the electroweak symmetry breaking mechanism and other physical phenomena at the TeV scale, like the CP violation problem, the quark-gluon plasma state and the search of new physics beyond the Standard Model such as Supersymmetry (SUSY) among others. The discoveries made in these fields will make linear colliders a precise tool to further understand the nature of such processes having access to very precise studies. The future linear collider parameters (mainly beam energy) will be determined by the LHC discoveries in the upcoming years. In the next sections the current status and highlights of the different searches of different experiments at the LHC are summarized.

Higgs searches: The 4^{th} of July 2012, in a seminar held at CERN, the collaborations of the experiments CMS and ATLAS presented an update of the Higgs searches status. At a confidence level of 4.9σ for CMS [2] and 5.0σ for ATLAS [3] from the Higgsless Standard Model, signals of a boson with a mass around $m_h = 125\,\text{GeV}$ were found with a strong spin-0 indication and coupling parameters consistent with the properties of the Standard Model Higgs particle. First results on various rare production decay modes have been obtained but more data is needed to observe these modes. Many analyses are ongoing and more updates are constantly presented.

Heavy flavour and CP violation: The experiments of the LHC, led by LHCb, have carried out several important findings and measurements in the heavy flavor sector. New previously unobserved states have been observed for the very first time during the last years like the states X_b, Ξ_b and Λ_s^0. Also the measurement of the quantum numbers of the state $X(3872)$ with $J^{PC} = 1^{++}$, has been determined to the 8σ level [4]. The CP violation of the oscillations in D and B mesons have been measured to

the 9.1σ confidence level discovering the same violation in B_s systems. The CP angle γ is now known with a precision without precedents ($\gamma = (67 \pm 12)^\circ$). Finally, some very rare decays like $B_s \to \mu^+\mu^-$, $B^0 \to K^*\mu^+\mu^-$ and $D_s^+ \to \pi^+\mu^+\mu^-$ have been observed [5] with possible implications on the analysis of new physics.

Quark-gluon plasma: The quark-gluon plasma, present in the very first moments after the Big Bang, is produced in ultra-relativistic heavy ion collisions. The conditions observed at the LHC experiments (ALICE, ATLAS and CMS) are in agreement with the observations carried out at RHIC. It has been confirmed that the hydrodynamics model helps in the understanding of the behavior of the processes occurred during the collision. This behavior is still far from being understood but the p-Pb and Pb-Pb collisions will reveal some of the underlying physics in the near future.

SUSY and Dark matter searches: The Higgs boson is in the center of the particle physics and most of the rest of discoveries will depend in some way on it. One of the problems that arises is the stabilization of the Higgs mass and its divergences when we consider quantum corrections. The most extended antidote for this quantum instability involves a new principle of nature called supersymmetry (SUSY): a new symmetry that unifies bosons and fermions. After data collected during 2011 and 2012, SUSY searches at the LHC did not find any clear evidence of any light superpartner (squark or gluino) and it has pushed their masses limits beyond 1 TeV within constrained models [6]. However, they still provide rather limited constraints on a more general theory of supersymmetry.

In general, no New Physics beyond the Standard Model has been observed but it is possible to find new particles and interactions during the second run at 14 TeV. These already performed and expected discoveries will motivate the construction of a very precise machine like a linear collider.

1.2 Why linear colliders?

Electron (or positron) circular colliders have an important inconvenient: synchrotron radiation. When charged particles are bent in dipole magnets, they emit photons and therefore lose energy. The energy loss depends on the bending radius, the particle mass and on the particle energy. More energy implies more radiation and lighter particles emit more than heavy particles. Therefore, either a huge circular accelerator is constructed ($\sim 80 - 100$ km for a circular collider of about 300 GeV) in order to reduce the bending angle and thus reduce synchrotron radiation emission) or a linear accelerator to minimize the synchrotron radiation impact allowing the exploration of the multi-TeV energy range is considered.

The physics potential of next linear colliders has been extensively studied since the Stanford Linear Collider (SLC) era [7, 8]. The Standard Model Higgs particle will have distinctive signals and SUSY and other alternative models also have many possibilities of being found and studied. The advantage of a linear collider with respect to LHC relies on the general cleanliness of the events where two elementary particles with known kinematics and spin (in case of polarized beams) define the initial state. A very high resolution of the detector is possible due to the relatively low absolute rate of background events. Summarizing, the Linear lepton Collider (LC) has the following main advantages with respect to hadron colliders:

- Clean experimental environment.
- Background processes well calculated and measured.
- Ability to scan systematically in c.o.m. energy.
- Possibility of high degree of e^- and e^+ polarization (restricted to ILC).
- Incisive measurements via jet/flavor tagging.
- Possibility for $\gamma\gamma$, e^-e^-, $e^-\gamma$ colliders

Due to all these points a linear lepton collider presents a better performance in terms of precision of the measurements with respect to circular hadron colliders. In the next sections the accelerator complex and the main experiments are described.

1.3 Physics prospects for e^+e^- colliders

The complementarity of the LC and the LHC has been established over many years by a dedicated worldwide collaborative effort. If new particles are found by the LHC, the LC will be essential in determining the properties of these new particles and unraveling the underlying structure of the new physics.

The Standard Model has been confirmed via its $SU(3)_C \times SU(2)_L \times U(1)_Y$ gauge structure and the precise measurement of its parameters has been achieved through a combination of analyses from LEP, SLC, HERA, B-factories, Tevatron and now the LHC. The next Linear Collider could even go further in the complete description of the nature of the elementary particles, with precisions never reached [9–12]. In the next sections some of these points are briefly summarized.

1.3.1 Higgs Physics and the Electroweak Symmetry Breaking

The Higgs mechanism is responsible for electroweak symmetry breaking and accounts for the generation of the masses of all the other elementary particles. The observation of a signal compatible with a low-mass Higgs boson at the LHC represents one of the most significant discoveries of science in the last decades. Therefore, a precise measurement of its properties is fundamental to complete the map of the particle physics.

The key features of the Higgs physics program at the LC include:

- Precise measurement of the couplings of the Higgs to the gauge bosons and fermions and, in particular, an absolute measurement of its coupling to the Z boson independent of its decay modes.
- Precise measurements of its mass, decay width, spin and CP properties.
- Measurement of the trilinear Higgs self-coupling, providing direct access to the Higgs potential.

The LC measurements would establish whether the Higgs boson has the properties predicted by the SM, or is part of an extended Higgs sector such as in SUSY models or whether it has a completely different physical origin which would be the case for a composite Higgs.

Higgs production at a Linear Collider

At a LC, the main Higgs production channels are through the Higgs-trahlung and vector boson fusion processes (Fig. 1.1). At relatively low c.o.m. energies the Higgs-strahlung process, $e^+e^- \to HZ$, dominates with a peak cross section at approximately 30 GeV above the HZ production threshold. At higher c.o.m. energies, the WW fusion process $e^+e^- \to H\nu_e\bar{\nu}_e$ becomes increasingly important.

1.3.2 Top quark sector

The top quark plays a very special role in the SM. It is the heaviest of the fundamental fermions and therefore the most strongly coupled particle to the electroweak symmetry breaking sector and hence intimately related to the Higgs mechanism. The precision study of the electroweak couplings of the top quark can reveal the presence of composite structure of the Higgs particle. A LC will measure the mass of the top quark in a direct way that is not possible at hadron colliders, fixing a crucial input to particle physics calculations.

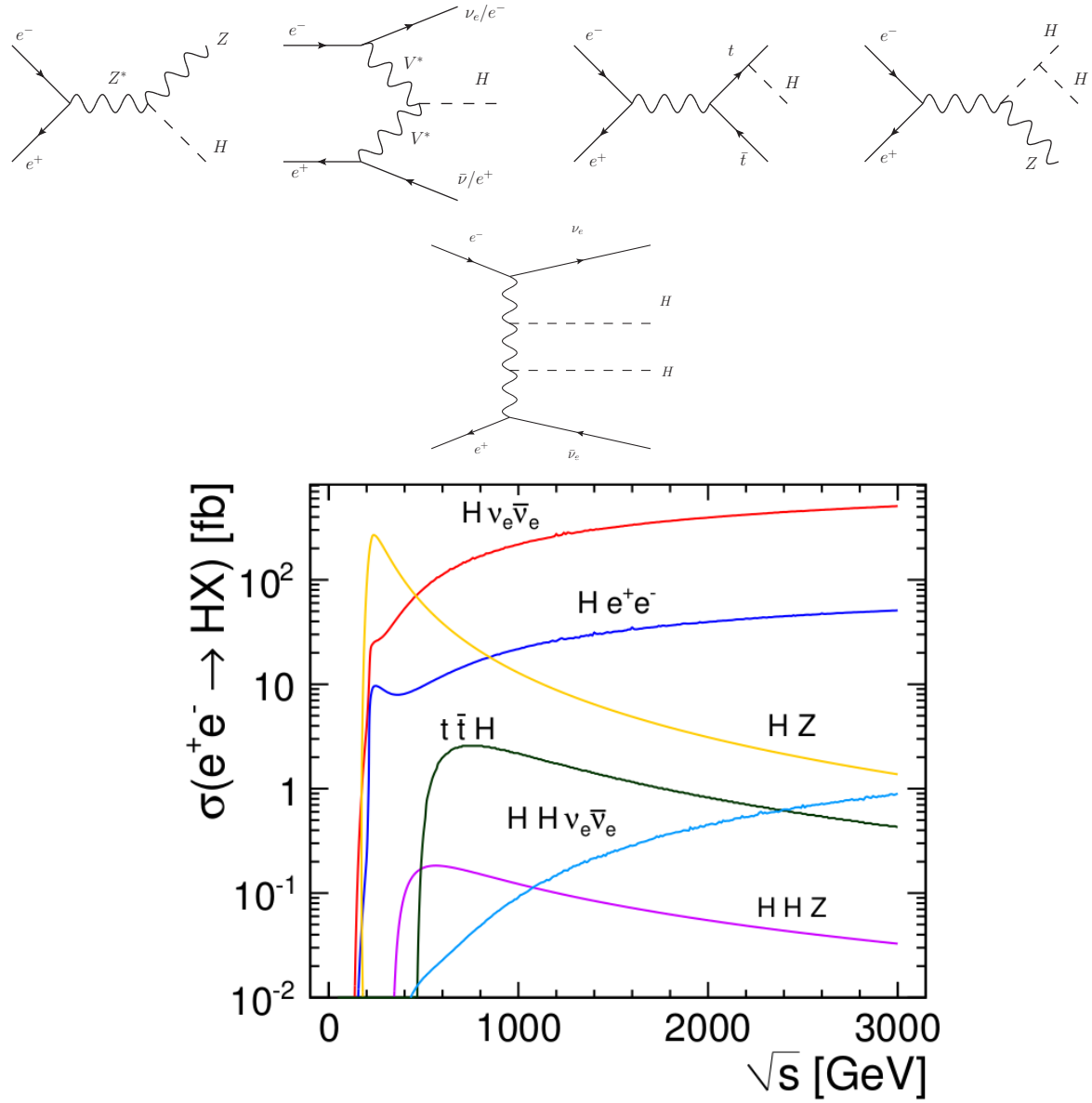

Figure 1.1: Feynman diagrams for production mechanism of the SM Higgs boson at CLIC and cross sections as a function of $\sqrt{s}$ for $m_h = 120$GeV.

1.3.3 New Physics

The LHC is expected to probe directly possible new physics beyond the Standard Model (BSM) up to a scale of a few TeV. While its data should provide answers to several of the major open questions in the present picture of elementary particle physics, it is important to start examining how this sensitivity can be further extended at a next generation of colliders. It is expected that new physics could be of supersymmetric nature. However, beyond supersymmetry, there is a wide range of other scenarios invoking new phenomena at the TeV scale. This new phenomena is aimed to explain the origin of electroweak symmetry breaking at stabilizing the Standard Model or at embedding the SM in a theory

Table 1.1: CLIC Design parameters at two different stages of the program: 500 GeV and 3 TeV center of mass energy.

Parameter	**Units**	3 TeV	500 GeV
Center of mass energy E_{CM}	GeV	3000	500
Repetition rate f_{rep}	Hz	50	50
Bunch population N_e	10^9	3.72	6.8
Number of bunches n_b		312	354
Bunch separation Δt_b	ns	0.5	0.5
Accelerating gradient G	MV/m	100	80
Bunch length σ_z	μm	44	72
IP beam size σ_x^*/σ_y^*	nm	40/1	200/2.26
Normalized emittance (IP) ϵ_x/ϵ_y	nm	660/20	2400/25
Luminosity $\mathcal{L}_{\mathrm{T}}$	$10^{34}\mathrm{cm}^{-2}s^{-1}$	5.9	2.3
Estimated power consumption P_{wall}	MW	589	272
Site length	km	48.3	13.0

of grand unification.

If supersymmetry is responsible for the existence of the Terascale and a light Higgs boson, then signals of superpartner particles should be seen at the LHC. Since supersymmetry is an organizing principle of nature, it can be realized in an infinite variety of ways but the LHC will not be able to deeply study the couplings and the spins of these new particles, the LC becomes a precision tool to provide an unequivocal answer.

If there is an extra dimension space where only gravitons can propagate, the weakness of the gravitational interaction can be explained. The Kaluza-Klein modes of the graviton can couple strongly to the SM particles, and these may be produced as spin-resonances at the LC.

1.4 Linear e^+e^- collider projects

There exist two proposals for an e^+e^- linear collider that follow the physics requirements explained above: CLIC and ILC, both described in more detail below.

1.4.1 CLIC

The Compact Linear Collider (CLIC) [9–13] aims to collide electrons and positrons at $\sqrt{s} = 3$ TeV with a luminosity of about $6 \cdot 10^{34}\mathrm{cm}^{-2}\mathrm{s}^{-1}$. To accomplish this task at a reasonable cost, the CLIC study proposes a two beam acceleration scheme featuring an accelerating gradient of the order of 100 MV/m. The RF power for acceleration is extracted from a low-energy and high-intensity beam (drive beam) and fed into the main beam via copper structures called PETS (Power Extraction and Transfer Structures). This mechanism allows a shorter accelerator than the one using superconducting technologies.

CLIC studies have been mainly focused on a 3 TeV c.o.m. energy design and the demonstration of the feasibility of the technology. A design for 500 GeV has also been developed opening the door to a possible staged scenario. CLIC site for $\sqrt{s} = 3$ TeV is about 48 km while for 500 GeV it is about 13 km. A general layout is shown in Fig. 1.2 for the 3 TeV (top) and for the 500 GeV case (bottom). The main parameters at both energies are summarized in Table 1.1.

The most critical areas for the CLIC design have been identified and they are: the ability to achieve the high main linac gradient of 100 MV/m, the generation, stabilization and deceleration of the drive beam, the generation of ultra-low emittances in the damping ring and their preservation up to the Interaction

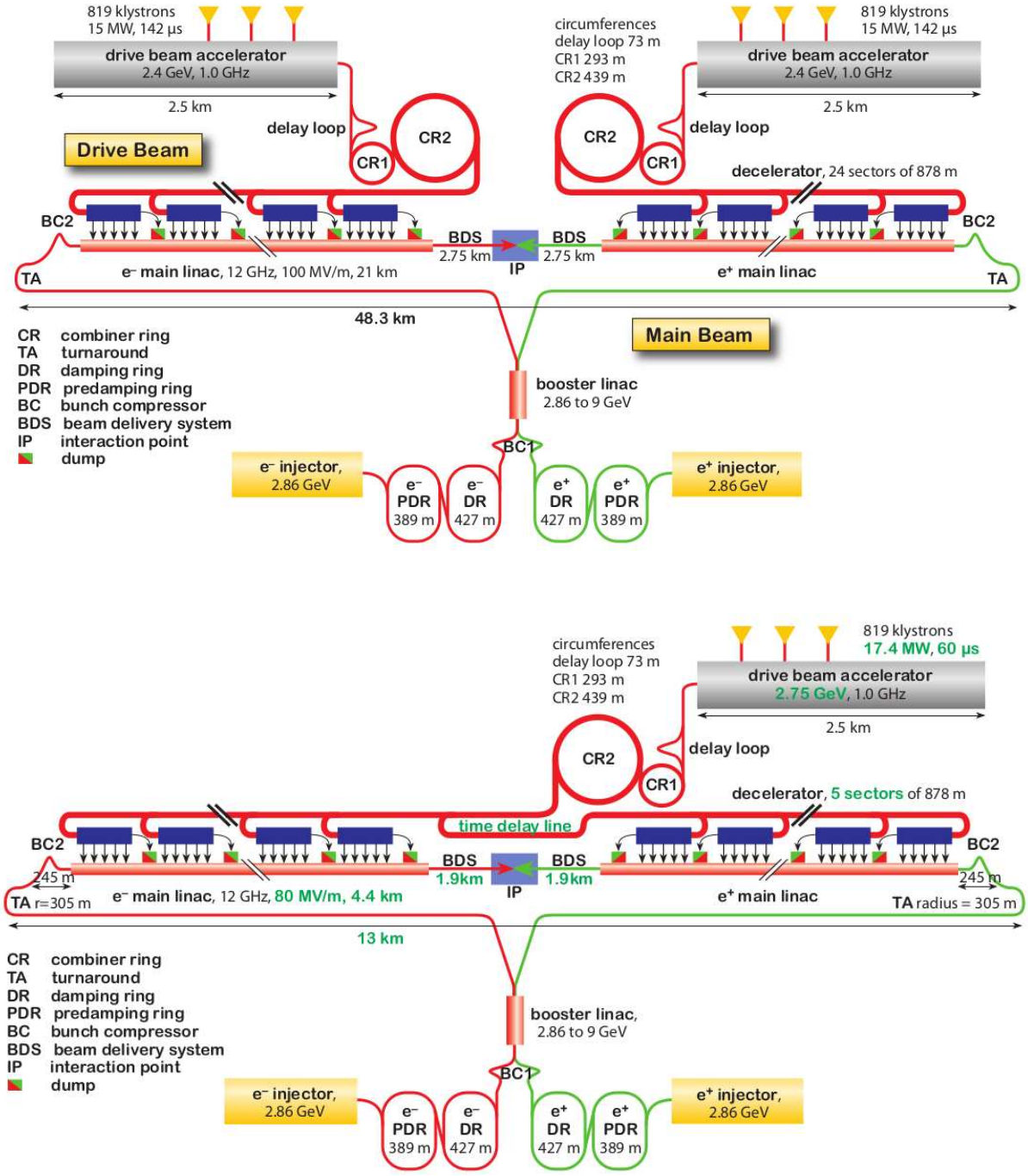

Figure 1.2: CLIC basic layout for 3 TeV system (top) and for 500 GeV system (bottom)

Point and the ability to protect the machine against damage while still providing a high availability. All these issues are being demonstrated by a sophisticated R&D program having established an international collaboration of 41 institutions and many facilities around the world, exploring the technological frontiers to demonstrate the CLIC technology feasibility. Another very important issue is the generation of the nanometer beam sizes at the IP and the chromatic correction performed at the Final Focus System (FFS).

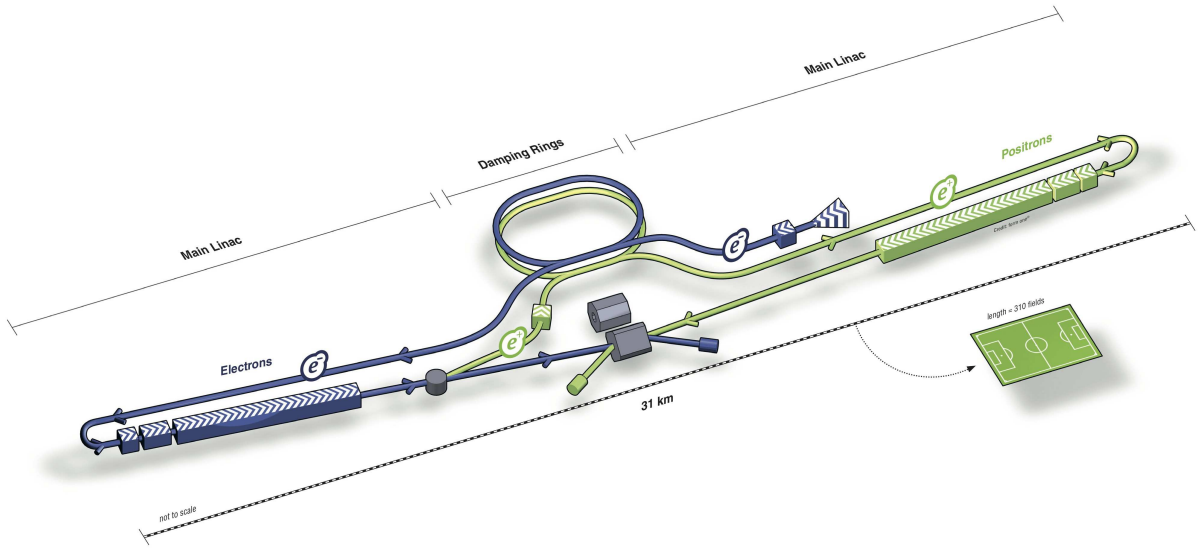

Figure 1.3: Schematic overview of the ILC layout with the interaction region placed in the middle of the site.

This last task is under experimental verification in the Accelerator Test Facility 2 (ATF2) at KEK in Japan. The recent achievements will be explained in the next chapters.

1.4.2 ILC

The International Linear Collider (ILC) [14, 15] is a proposed e^+e^- collider for a c.o.m. energy range between 200 and 500 GeV with an upgrade path towards an energy of 1 TeV. ILC is based on 1.3 GHz superconducting radio-frequency accelerating cavities with a required accelerating gradient of 31.5 MV/m. This characteristic represents the main difference with respect to CLIC and represents the main technological challenge of ILC. The development of this technology goes back to the work developed by the TESLA collaboration The same type of cavities are being produced for the European XFEL X-ray laser facility at DESY. The main parameters of ILC accelerator are summarized in Table 1.2

1.4.3 Main parts of a linear collider

CLIC and ILC projects are composed of similar main subsystems:

- Electron and positron sources: The electron source is a laser driven photo-injector, where circular polarized photons illuminate a GaAs cathode producing an electron current. In ILC, positrons are produced with the high energy electron beam. This is guided through a helical undulator. Circular polarized photons are extracted towards a thin rotating target and produce $e^{\pm}$ pairs. Particles coming from the source are bunched, pre-accelerated and transported in such a way that the beam fits into the Damping Ring dynamic aperture. CLIC positron source provides only unpolarized positrons thanks to a 5 GeV electron beam colliding with hybrid targets.

- Damping Rings: The pre-accelerated electron and positron beams have emittances that are too large to reach the small beam sizes in the collision. The beams are stored in the damping rings where superconducting wigglers make the beam to radiate photons along the beam direction. This effect reduces emittance by several order of magnitude in a few hundreds of milliseconds.

Table 1.2: ILC Design parameters for the 500 GeV center of mass energy program.

Parameter	**Units**	ILC
Center of mass energy E_{CM}	GeV	500
Repetition rate f_{rep}	Hz	5.0
Bunch population N_e	10^9	20
Number of bunches n_b		1312
Bunch separation Δt_b	ns	554
Accelerating gradient G	MV/m	31.5
Bunch length σ_z	μm	300
IP beam size σ_x^*/σ_y^*	nm	474/5.9
Normalized emittance (IP) ϵ_x/ϵ_y	nm	10000/35
Luminosity $\mathcal{L}_{\mathrm{T}}$	$10^{34}\mathrm{cm}^{-2}s^{-1}$	1.8
Estimated power consumption P_{wall}	MW	
Site length	km	31

- Main Linac: After the extraction of the beam from the damping rings, the beam is transported along the linac. The accelerating cavities placed in the linac increase the energy of the particles up to the final energy keeping the normalized emittance growth as low as possible.
- Beam Delivery System (BDS): The BDS transports the beam from the end of the main linac to the interaction point. It is responsible for the beam diagnostics, collimation and squeezing the beam down to the nanometer scale size in the Final Focus System (FFS). The FFS is extensively explained along the thesis.

1.4.4 Test Facilities

The linear collider R&D program comprises several test facilities that verify the technological developments required for the accelerator construction. For example, the CLIC Test Facility 3 (CTF3) aims to demonstrate the feasibility of the two beam acceleration technology. FFTB and ATF2 are Final Focus Test facilities in order to reproduce similar chromaticities like those of the future linear colliders. FFTB operated during the nineties and ATF2 is nowadays running with a great success.

CLIC Test Facility 3 (CTF3)

The CLIC Test Facility was built to demonstrate the generation of a high intensity beam and the feasibility of this novel two-beam acceleration concept. In the CLIC experimental area (CLEX) two main experiments are taking place: the two-beam acceleration and the stable deceleration of the drive beam [16,17]. The drive beam is generated by a thermionic gun, which emits electrons in a consensus stream. To generate the required intensities, the beam is divided in sub-trains that are combined in a delay loop to multiply the intensity a factor 2. The beam is sent then to a combiner ring that recombines again the trains of the beam and the beam intensity increases by a factor 4 (a factor 8 in total). After the recombination the beam is sent to two different experiments: the Two-Beam Test Stand (TBTS) with the aim to demonstrate the two-beam acceleration system and a second experiment designed to show a stable and efficient transport of a heavily decelerated beam.

Final Focus Test Beam (FFTB)

The Final Focus Test Beam (FFTB) [18–20] was an experimental test line developed at SLAC in the 90's with the aim to squeeze the beam to the tens of nanometer level, a demagnification close to the one required in ILC, using the optics based on the dedicated chromaticity correction scheme. The FFTB was located at the end of the SLAC linac, which was delivering electron and positron beams with an

energy of about 46.6 GeV. At that time the SLC damping ring provided a normalized vertical emittance of $7 \cdot 10^{-7}$ m which however increases up to $2 \cdot 10^{-6}$ m after the beam reached the end of the SLC linac. The FFS facility extended over 200 m formed by several separated sections. The first one was the beta matching section (BM) [21] for matching the incoming optical functions from the end of the SLC line to those of the FFTB. This section was followed by two separated chromaticity correction sections, for the horizontal and for the vertical plane. Each one contained sextupole magnets located at high dispersion regions in order to compensate the chromaticity produced by the final quadrupole magnets. The geometric aberrations were controlled by placing sextupoles in pairs at locations with the same dispersion but in opposite phase advance. The final doublet (FD) was embedded in the final transformer (FT), it demagnified the beam size at the focal point.

In May 1994 by relaxing the horizontal focusing in order to reduce the background signal, the smallest vertical spot size of 70 ± 7 nm was observed in the Shintake monitor located at the virtual Interaction Point [19, 20]. This result has been recently overcome by the ATF2 test facility explained briefly below and more in detail in the following chapters.

The ideas developed during the FFTB operation are studied in detail in the following chapters and applied to the CLIC Final Focus System.

Accelerator Test Facility (ATF)

The Accelerator Test Facility (ATF) at KEK [22], in Japan, is a prototype damping ring (DR) that already has succeeded in obtaining the required emittances that satisfy ILC specifications. The ATF DR delivers beams with vertical emittance of 12 pm.rad (with a minimum achieved emittance of 4 pm.rad [23]) and it injects a beam with an energy of 1.3 GeV to the ATF2 final focus test beam line [24], which was constructed in 2008 with the purpose to demonstrate the local chromaticity correction FFS scheme [25]. ATF2 measures about 90 meters long from the extraction point in the ATF damping ring to the virtual interaction point, where a beam size monitor is located. The line is composed of the extraction section, a matching section, the Final Focus System based on the local chromaticity correction scheme and the IP. Quadrupoles and sextupoles composing the line are mounted on three-axis movers in order to mitigate ground motion and thermal instabilities.

The primary goal of ATF2 is to achieve a 37 nm vertical beam size at the IP and its stabilization at the nanometer level. During the 2013 run the smallest beam size achieved was $\sigma_y^* = 65$ nm and its reproducibility several times [26] setting a new record. This beam size has been pushed down recently until the $\sigma_y^* = 44$ nm [27, 28].

Chapter 2

Beam Dynamics

Accelerator physics covers a wide variety of topics from the very theoretical treatment of the beam dynamics to the design and construction of the real accelerator. For the studies here presented, we will focus on the physics related to the beam and its interaction with the accelerator, namely, the beam dynamics. The concepts presented here are just an introduction to the needed tools used in the next chapters. For more details there are a lot of references that the reader can follow, for example [29].

2.1 Linear Beam Dynamics

An accelerator is mainly composed of dipole magnets, to bend and guide the beam and by quadrupoles, to focalize it. In accelerator physics the Frenet-Serret coordinate reference system is commonly used (Fig. 2.1). This system follows the beam reference path. The longitudinal position along the trajectory is denoted by s, the transverse positions are given by x in the horizontal plane and y in the vertical plane. The longitudinal position within the bunch is denoted by z.

The general differential equation for transverse on momentum linear uncoupled motion is described by the Hill's equation,

$$u'' + K_u(s)u = 0 \tag{2.1}$$

where u stands for the transverse coordinates x or y, $K_u(s)$ the focusing functions in analogy with a harmonic oscillator, in which now the spring constant K depends on the longitudinal position s. For instance, $K > 0$ and $u = x$ represents a focusing quadrupole while $K < 0$ represents a defocusing quadrupole. A drift space is represented by $K = 0$ since no force is acting on the particle.

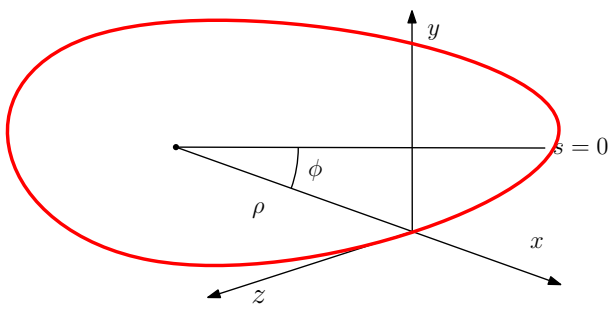

Figure 2.1: Frenet-Serret reference system along the design orbit.

According to the Floquet theorem, the solution with periodic boundary conditions of the Hill's equation (2.1) reads:

$$u(s) = A_u\sqrt{\beta_u(s)}\sin(\phi_u(s) + \phi_{u.0}) \tag{2.2}$$

where A_u and $\phi_{u.0}$ are constants given by the initial conditions, β_u modulates the amplitude of the beam and ϕ is the phase advance given by,

$$\phi_u(s) = \int_0^s \frac{ds'}{\beta_u(s')} \tag{2.3}$$

There are other related functions like the α and γ-functions defined by

$$\alpha_u \equiv -\frac{1}{2}\frac{d\beta_u}{ds} \tag{2.4}$$

$$\gamma_u \equiv \frac{1+\alpha_u^2}{\beta_u}. \tag{2.5}$$

The set of this six functions $(\beta_{x,y}, \alpha_{x,y}, \gamma_{x,y})$ are called the Courant-Snyder functions and, together with the phase advance, they can describe the complete linear motion for on momentum particles. One of the important results relies in that, at any location s of the ring, a trajectory in the phase space (u, u') has an area bounded by an ellipse with equation,

$$\epsilon = \gamma u^2 + 2\alpha u u' + \beta u'^2. \tag{2.6}$$

The expression (2.6) is called the Courant-Snyder invariant and it is equal to the equation of an ellipse that encloses an area $\pi\epsilon$ where ϵ is the so called beam emittance. And from this expression we can define the rms linear transverse beam size,

$$\sigma_u(s) = \sqrt{\beta_u(s)\epsilon^u_{\text{rms}}(s)} \tag{2.7}$$

Beam emittance defined by (2.6) varies when beam energy changes. One can define an invariant under acceleration, the *normalized emittance*, given by

$$\epsilon_n = \gamma\epsilon, \tag{2.8}$$

where γ is the relativistic factor $\gamma = E/m_e c^2$.

Particles with different energy are affected differently by the bending magnetic fields, i.e., particles with higher energy have a larger bending radius than the particles with lower energy. For that reason the so called dispersion function is defined like,

$$D(s) \equiv \frac{dx(s)}{dp/p} \tag{2.9}$$

where Δx is the transverse displacement from the reference orbit (horizontal in this case) and $\delta = \Delta p/p$ is the relative momentum deviation.

2.2 Nonlinear Beam Dynamics

In the previous section we have introduced the main concepts of the linear motion of the particles circulating through the different elements of the accelerator. As we will see, due to the presence of nonlinear fields such as sextupolar and other multipolar magnets or due to the very high strength of some quadrupoles a treatment of the beam dynamics beyond the linear regime is required. For that reason, in the next sections we introduce some concepts that describe the nonlinear beam motion based on two different formalisms: the Taylor maps and the Lie algebra formalism.

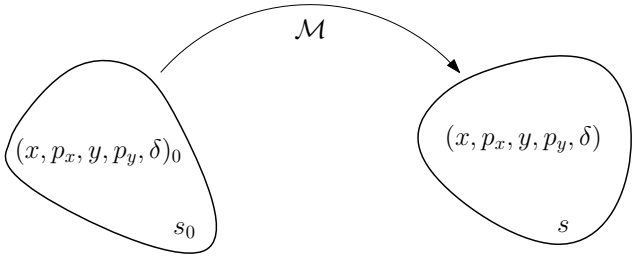

Figure 2.2: Diagram showing the application of map $\mathcal{M}$ of a set of initial coordinates at position s_0 to a set of final coordinates at position s.

2.2.1 Taylor Maps

Let $z = (x, p_x, y, p_y, \delta)$ the five-dimensional vector in the Frenet-Serret reference system shown in Fig. 2.1 that describes the particle in the five-dimensional phase space, where x and y are the transverse coordinates and p_x and p_y the corresponding transverse momenta. The energy spread is given by $\delta \equiv \frac{\Delta p}{p}$ where p is the reference momentum. Let z_0 the initial set of coordinates and $\mathcal{M}$ the map that transforms this initial set to the final set of coordinates described by the vector z_f (see Fig. 2.2). Mathematically it can be expressed by,

$$\mathcal{M} : z_0 \to z_f, \quad z_f = \mathcal{M} z_0 \tag{2.10}$$

The map $\mathcal{M}$ represents a symplectic mapping. In the linear case, the transfer map can be represented by a matrix R. In the nonlinear case, we can also represent the map by a general expression

$$z_f = \mathcal{M} z_0 = \sum_{ijklm} X_{ijklm} x^i p_x^j y^k p_y^l \delta^m, \tag{2.11}$$

where X_{ijklm} are the coefficients of the mapping between initial (z_0) and final coordinates (z_f). The order of the coefficients is given by $q = i + j + k + l + m$ and the linear part can be identified by $X_{ijklm} = R$ with $q = 1$, where R is the transfer matrix commonly used in the linear matrix approach [29]. One can truncate the above expansion at a given order but the simplecticity is not necessarily preserved if truncation is above the first order.

2.2.2 Lie algebra formalism

The Lie operator formalism [30] is a robust and powerful tool to solve analytically a wide range of beam dynamics problems with a high degree of nonlinearity. Also physically it is very appropriate since it preserves symplecticity in the solution of the nonlinear equations and avoids nonphysical errors of numerical algorithms. Here we present the basic motivation and properties of this formalism and how it will be applied in the following sections to understand optical aberrations following physical arguments.

Lie Transformations in mechanics

Consider a particle in an electromagnetic field. Let $\mathbf{z} = \{\mathbf{q}, \mathbf{p}\}$ the generalized coordinates in the 6-D phase space. For a given set of initial conditions the particle's motion is governed completely by Hamilton's equations:

$$\dot{q}_i = \frac{\partial H}{\partial p_i}; \quad \dot{p}_i = -\frac{\partial H}{\partial q_i}, \tag{2.12}$$

where H is the Hamiltonian of the system.

The Poisson bracket arises when we consider the change in time of a dynamical variable f, where f is any smooth function of the dynamical variables $\mathbf{q}$ and $\mathbf{p}$ along a trajectory. By the chain rule we have the relation,

$$\frac{df}{dt} = \frac{\partial f}{\partial t} + \sum_i \left(\frac{\partial f}{\partial q_i}\dot{q}_i + \frac{\partial f}{\partial p_i}\dot{p}_i \right). \tag{2.13}$$

We introduce the Poisson bracket $[f, g]$ of any two functions f and g defined by:

$$[f, g] = \sum_i \left(\frac{\partial f}{\partial q_i}\frac{\partial g}{\partial p_i} - \frac{\partial f}{\partial p_i}\frac{\partial g}{\partial q_i} \right), \tag{2.14}$$

Eq. (2.13) can be written in the compact form,

$$\frac{df}{dt} = \frac{\partial f}{\partial t} + [f, H] \tag{2.15}$$

particularly, if we take $f = H$ one gets $\frac{dH}{dt} = \frac{\partial H}{\partial t}$ and if H does not explicitly depend on time $\frac{dH}{dt} = 0$ which expresses the conservation of some quantity H, usually the energy of the system.

Definition 2.2.1 *We define a Lie operator* $: f :$ *in a Hamiltonian vector field by the rule,*

$$: f : g \equiv [f, g] \tag{2.16}$$

where g *is any function of* $\mathbf{z}$ *and* $[,]$ *denotes the Poisson bracket defined in (2.14)*

Definition 2.2.2 *A Lie transformation is the exponential adjoint Lie operator:*

$$\mathcal{L} \equiv \exp(: f :) = \sum_{n=0}^{\infty} \frac{1}{n!}(: f :)^n \tag{2.17}$$

that acts on a function g *as:*

$$\mathcal{L}g = \exp(: f :)g = g + [f, g] + \frac{1}{2!}[f, [f, g]] + \ldots. \tag{2.18}$$

If we identify the function in the exponential operator with $f = -tH$ where H is the Hamiltonian of the system and t is the independent variable, and we apply the corresponding Lie transformation to the canonical variables $\mathbf{z} = \{\mathbf{q}, \mathbf{p}\}$ when these functions do not explicitly depend on time taken at t_0 we obtain,

$$\exp(-t : H :)\mathbf{z}(t_0) = \sum_{n=0}^{\infty} \frac{t^n}{n!}\frac{d^n\mathbf{z}}{dt^n} \mid_{t_0} = \mathbf{z}(t_0 + t) \tag{2.19}$$

where one can identify the result with the usual definition of the translation of a system by a time t using the Taylor series expansions of the function at the time t_0. Since in accelerator physics the time coordinate t is replaced by the trajectory s, the time evolution must be replaced by the evolution along the ring or the beamline, but the formalism itself applies in the same way.

BCH theorem

An accelerator is composed by a concatenation of elements, usually drift spaces, quadrupoles. As we will see, each element has its own Hamiltionian, and the Lie transformation along the sequence of elements is just the ordered product of the different transformations in each element. The basic formula that allows to concatenate exponential operators is called the Baker-Campbell-Hausdorff (BCH) formula. This formula reads,

$$e^{:f:}e^{:g:} = e^{:h:}, \tag{2.20}$$

where g and f are fully differentiable functions of the dynamical variables and

$$h = f + g + \frac{1}{2}[f, g] + \frac{1}{12}[f - g, [f, g]] + \dots . \tag{2.21}$$

Finally, using the BCH formula, we can express the whole sequence of elements in one unique term that contains all the information of the system,

$$\prod_i \exp(- : l_i H_i :) = \exp(- : L H_{\text{eff}} :), \tag{2.22}$$

where L is the total length of the system and H_{eff} is the effective Hamiltonian that represents the complete series of elements.

Similarity transformations

The algebra of Lie transformations is non-commutative and the reordering of the product of the elements of such transformations can be performed using similarity transformations. The similarity transformation can be interpreted as a simple coordinate transformation,

$$q_i \to q_i + [f, q_i] + \frac{1}{2!}[f, [f, q_i]] + \dots , \tag{2.23}$$

$$p_i \to p_i + [f, p_i] + \frac{1}{2!}[f, [f, p_i]] + \dots . \tag{2.24}$$

If f is a quadratic function of q and p, the change of coordinates is linear and can be expressed in a matrix form. This corresponds to the Lie algebra equivalent of the familiar change of coordinates in the algebra of matrices:

$$M' = RMR^{-1}. \tag{2.25}$$

If we consider a series of transformations, we can reorder this series by successive applications of the similarity transformations. We can reorder a series of mixed linear f_i and non-linear g_i transformations. It is possible to move all the non-linear terms together by successively moving them through the linear terms as follows:

$$e^{:g_1:} e^{:f_1:} e^{:g_2:} e^{:f_2:} = e^{:g_1:} e^{:f_1:} e^{:f_2:} e^{:g_2\left(e^{:f_2:} z\right):} = e^{:f_1:} e^{:f_2:} e^{:g_1\left(e^{:f_2:} e^{:f_1:}\right):} e^{:g_2\left(e^{:f_2:} z\right):}. \tag{2.26}$$

The non-linear transformations keep the same structure although the coordinates on which they act are now different. Note that since the f_i are linear transformations the familiar tools of matrix algebra can be applied. The BCH theorem can be used to express in a single non-linear term all the non-linear terms coming from different contributions so that the whole series is reduced to one linear transformation times one non-linear term.

Applications to Optics

The Lie exponential formalism explained above is easy to apply to explain the beam motion passing through a beamline composed by drifts spaces, bending magnets, quadrupoles and higher order multipoles. Taking definition (2.2.2) one can describe the dynamics of the system identifying the function f with the Hamiltonian of the system and g with the initial coordinate we want to transform. Therefore, all the information is stored in the Hamiltonian of all the elements that compose the beamline and using the BCH formula (2.21) one can describe the whole system with just one expression.

The following truncated Hamiltonians describe the dynamics of a particle in respectively a bending magnet, a quadrupole and a sextupole [31].

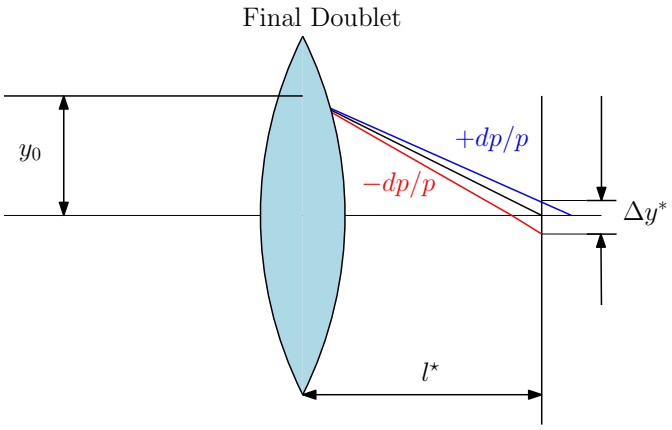

Figure 2.3: Scheme of the chromatic aberration introduced by the final doublet. The black line represents the on-momentum particle while the red and the blue ones represent a particle with a bit less energy and a bit more energy respectively and how the focalize to different points. This effect is seen at the IP as a beam size dilution.

Dipoles

$$H = \frac{1}{1+\delta}\left(-\frac{x\delta}{\rho} + \frac{1}{2\rho^2}x^2\right) + \frac{1}{2}\left(x'^2 + y'^2\right) \tag{2.27}$$

Quadrupoles

$$H = \frac{1}{2(1+\delta)}K_q\left(x^2 - y^2\right) + \frac{1}{2}\left(x'^2 + y'^2\right) \tag{2.28}$$

Sextupoles

$$H = \frac{1}{3!(1+\delta)}K_s\left(x^3 - 3xy^2\right) + \frac{1}{2}\left(x'^2 + y'^2\right) \tag{2.29}$$

where ρ is the curvature radius of the bending magnet and $\delta = \frac{dp}{p}$ is the energy spread. The constants K_q and K_s determine the quadrupole and the sextupole gradient and the phase space is determined by the spatial coordinates x and y and the momentum coordinates $x' = p_x/p_s$ and $y' = p_y/p_s$ being $p_{x,y}$ the canonical transverse momentum and p_s the longitudinal momentum.

2.3 Chromaticity

Much like in the classical Newton's experiment of light diffraction, where he could split white light into different colors of the spectra due to the difference in refraction index for different wavelengths, we can see that only particles with the nominal design momentum will be focused exactly at the IP. Off-momentum particles will be focused at different longitudinal positions, effectively increasing the beam size at the IP. This effect is called chromaticity by analogy with light optics and can be seen schematically in Fig. 2.3.

Commonly in the literature the vertical chromaticity originated at the FD is quantified by the approximation,

$$\frac{\Delta y^*_{\text{rms}}}{\sigma^*_{y,0}} \approx \frac{l^*}{\beta^*_y}\sigma_\delta \approx \xi_y \sigma_\delta, \tag{2.30}$$

where ξ_y is the term called chromaticity, l^* is the length of the last drift between the last quadrupole and the IP, β^*_y is the vertical beta-function at the IP and σ_δ is the energy spread of the beam. Chromaticity

for a single quadrupole can be calculated using the expression

$$\xi_{x,y} = \int \beta_{x,y}(s)K(s)ds, \tag{2.31}$$

where $K(s)$ is the strength of the quadrupole and $\beta_{x,y}$ the horizontal and vertical β-function at the quadrupole location. The chromatic dilution of the vertical beam size is given by

$$\sigma_y^* \approx \sigma_{y,0}^* \sqrt{1 + \xi_y^2 \sigma_\delta^2}, \tag{2.32}$$

and it may be very large, tens or thousands of times the nominal beam size. One can rewrite the above expression for chromaticity in the map formalism [51] for a Gaussian energy distributed beam,

$$\xi_y^2 = \frac{1}{\beta_y^*}\left(X_{y,00101}^2 \beta_{y0} + X_{y,00011}^2 \frac{1}{\beta_{y0}}\right) \tag{2.33}$$

where X_y are the coefficients of the transfer map given by Eq. (2.11) between the beginning of the line and the IP. The terms β_{y0} and β_y^* are the vertical β-functions at the starting point and at the Interaction Point (IP) respectively.

Of course, this effect must be compensated in some way to avoid beam size and luminosity dilution. The idea is to compensate this effect using sextupoles. Due to the nonlinearity of the sextupolar field, sextupoles can focalize particles with different energies to the same point compensating the aberration introduced by quadrupoles. Let us consider a combination of one quadrupole and one sextupole, with Hamiltonian introduced in (2.28) and (2.29) respectively taking into account just the terms related to the proper fields. We assume as valid the thin lens approximation, i.e. the particle position does not change within the element and therefore we do not need to consider the x' and y' dependence of the Hamiltonian. For small values of δ we can obtain the expression,

$$H_q = \frac{1}{2}k_q(x^2 - y^2) - \frac{1}{2}k_q\delta(x^2 - y^2), \;\; H_s = \frac{1}{3!}k_s(x^3 - 3xy^2). \tag{2.34}$$

In order to compensate the chromatic aberration, we need to locate the sextupole in a dispersive region to separate in space particles with different energy. This task is done by a horizontal bending magnet located upstream of the FD. In terms of the Hamiltonian, this can be interpreted as a change of coordinates given by

$$x \to x + \eta_x\delta \tag{2.35}$$

$$y \to y \tag{2.36}$$

where η_x is the horizontal dispersion at the sextupole location. We consider two cases. In the first one only the sextupole is in a dispersive region while quadrupole remains in a dispersion-free region. Hamiltonians can be rewritten,

$$H_q = \frac{1}{2}k_q(x^2 - y^2) - \frac{1}{2}k_q\delta(x^2 - y^2) \tag{2.37}$$

$$H_s = \frac{1}{3!}k_s(x^3 - 3xy^2) + \frac{1}{2}k_s\eta_x\delta(x^2 - y^2) + \frac{1}{2}\eta_x^2\delta^2 x + \frac{1}{3!}\eta_x^3\delta^3 \tag{2.38}$$

We need to merge the expressions (2.37) and (2.38) in one single Hamiltonian using the BCH formula (2.21). Since we have assumed no dependence on $p_{x,y}$ the terms $[H_q, H_s]$ vanish and the single Hamiltonian is just the sum of the quadrupole and sextupole Hamiltonian $H = H_q + H_s$. The chromatic term coming from the Hamiltonian is canceled by the second term in (2.38) if we take $k_q = k_s\eta_x$. The remaining terms are the proper focusing term from the quadrupole $\frac{1}{2}k_q(x^2 - y^2)$, a geometric term coming from the sextupole $\frac{1}{3!}k_s(x^3 - 3xy^2)$ that will is compensated introducing a second sextupole with opposite phase, a second order dispersion term $\frac{1}{2}\eta_x^2\delta^2 x$ and finally a purely chromatic term $\frac{1}{3!}\eta_x^3\delta^3$ that has no

effect on the dynamics of the particles.

If we consider now the case where the quadrupole is also in a dispersive region with dispersion value η_x the quadrupole Hamiltonian is

$$H_q = \frac{1}{2}k_q(x^2 - y^2) - \frac{1}{2}k_q\delta(x^2 - y^2) + k_q\eta\delta x - k_q\eta_x\delta^2 x + \frac{1}{2}k_q\eta_x^2\delta^2 - \frac{1}{2}k_q\eta_x^2\delta^3. \tag{2.39}$$

Again, the last two terms do not have effect on the dynamics since they have no dependence on the coordinates. Two new terms proportional to x appear. The second order dispersion term $-k_q\eta_x\delta^2 x$ is half compensated with the second order dispersion term coming from the sextupole. In order to fully compensate this term, sextupoles must double its strength but then an overcompensation of the chromaticity is applied. For that reason the entire chromaticity of the FFS must be generated upstream of the FD in a non-dispersive region.

The reason we have separated the analysis in two different cases is because there are two different approaches in order to compensate the chromatic effect, the traditional scheme, based on dedicated chromatic correction sections for each plane; and the local correction scheme, based on the local correction of the chromaticity. Each of them represents the cases described above.

2.4 Final Focus Systems

The Final Focus System (FFS) is a part of the Beam Delivery System (BDS) of a linear collider. The BDS also includes the energy and betatron collimation systems, diagnostics section (including very precise energy spectrometer and polarimeter), main extraction line, tune-up and extraction line. The large chromaticity generated by the Final Doublet (FD) requires dedicated cancellation as well as other associated aberrations not coming directly from the FD such as sextupole geometric aberrations. In order to minimize the emittance growth and energy spread due to synchrotron radiation in bending sections in the FFS and BDS in general, the bending magnets must be long and weak determining the total length of the whole system. The need to collimate the beam halo also affects the design and total length of the collimation section and also determines whether the collimation system spoilers and absorbers need to be survivable or consumable. All these and some other requirements are taken into account in the design of the BDS of a linear collider.

The main task of a linear collider Final Focus System [32,33] is to focalize the beam to the small sizes required at the Interaction Point (IP). To achieve this, the FFS forms a large and almost parallel beam at the entrance of the Final Doublet (FD), which contains two strong quadrupole lenses. Typically, two different concepts of FFS have been developed: a dedicated non-local chromaticity correction scheme, with a dedicated correction section for each plane and an alternative where chromaticity is corrected locally at the FD. In the next sections both schemes are widely described.

Almost all of this thesis is devoted to the description, comparison, optimization and simulation of different Final Focus Systems for CLIC and ILC.

2.4.1 Dedicated Chromaticity Correction Scheme

One of the first designs of the FFS for linear colliders contains four sections: the matching telescope (MS), the horizontal chromaticity correction section (CCX), the vertical chromaticity correction (CCY) and the final telescope (FT) where the Final Doublet (FD) is located. The chromaticity compensation sections consisted of symmetric optics which created two locations with large beta-functions in both planes as well as maximum of dispersion function, where sextupoles are placed. The transfer matrix between sextupoles was designed to be $M = -\mathcal{I}$ in order to cancel geometric aberrations produced by sextupoles for

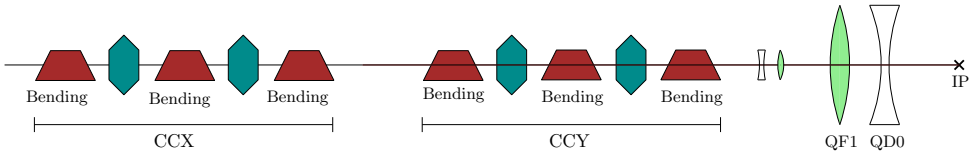

Figure 2.4: Basic layout of the traditional chromaticity correction scheme showing only vertical chromatic correction. In general, the traditiona scheme contains two separated correction section for horizontal and veritcal planes.

on-energy particles, while creating additional focusing/defocusing effect for off-energy particles, to compensate the FD chromaticity as explained in previous sections. The two pairs of sextupoles separated by a $-\mathcal{I}$ transformation were typically non-interleaved, to minimize the third and higher order aberrations. All earlier designs followed this principle. Designs like this one are present in FFTB [21], the JLC FF optics [34], VLEPP optics [35] and the NLC [36]. In Fig. 2.4 a schematic view of such system with the two chromatic correction sections is shown.

Although its simplicity, this system is rather long, increasing its cost, with long bending sections that induce important quantities of synchrotron radiation diluting the beam size at the IP. Since the chromatic compensation is done far away from the main chromaticity source, the Final Doublet, any disturbance to the beam due to, for example, synchrotron radiation created between sextupoles and IP would disturb the correct compensation of the chromaticity. Another important issue is the bandwidth limitation due to the chromatic breakdown of the $-\mathcal{I}$ transformation between sextupoles. This in particular creates large aberrations for off-energy particles and especially for particles in the beam tails. This scheme was considered in the former designs of the CLIC FFS design [37].

2.4.2 Local Chromaticity Correction Scheme

An alternative design was suggested in 2001, performing a local correction of the chromaticity [25]. In this design, the chromaticity is canceled locally by two sextupoles interleaved with the FD. The dispersion needed in the FD region is generated by a bending magnet upstream. The parasitic second order dispersion present in Eq. (2.39) is canceled locally provided half of horizontal chromaticity arrives from upstream of the FD. The geometric aberrations introduced by the FD sextupoles are canceled by adding two more sextupoles placed in phase with them and upstream of the bending magnet. The higher order aberrations are canceled by means of the optimization of the transfer matrices between sextupoles. The design feature comes from the fact that two sextupoles placed in the FD cannot simultaneously cancel three parameters: the x and y chromaticity and the x-second order dispersion, however, introducing a new free parameter, the amount of horizontal chromaticity arriving upstream of the FD, allows to cancel all three major lower order aberrations simultaneously. The general layout of such scheme is shown in Fig. 2.5.

The first FFS based on the local chromatic correction principle has been used in the later designs of the NLC FFS, which previously was designed using the traditional scheme. It was found that the local scheme was 6 times shorter than traditional scheme [25]. Moreover, the energy bandwidth of the local correction scheme was found to be better than in the non-local correction. It was found that the later scheme has much less aberrations and it does not mix betatron phases of non-core particles, which has important implications on the beam halo generation and its impact on the collimation system. The drawback for the improved performance was a more difficult design process, which is caused by the fact that good cancellation of higher order aberrations required optimal selection of the first order optics. In spite of these difficulties, a semi algorithmic procedure has been found and its recipe is given in [38].

This newer scheme is currently considered for the ILC and CLIC baseline designs and it is being tested

at ATF2, where recently vertical spot sizes of about 44 nm have been reached [26–28] representing the experimental validation of this scheme.

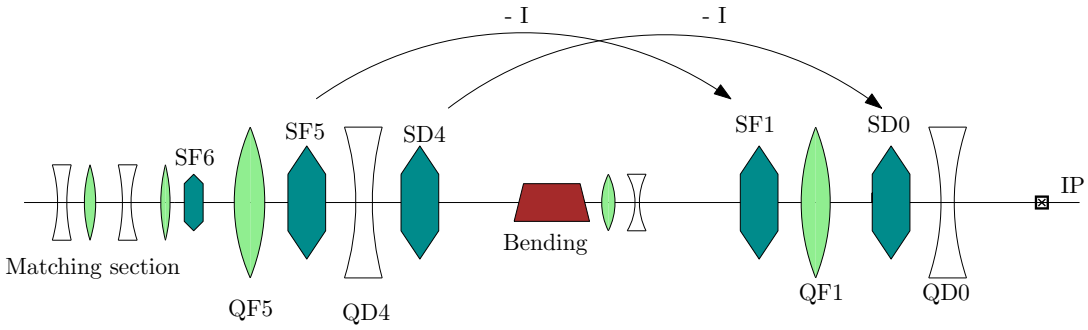

Figure 2.5: Basic layout of the local chromaticity correction scheme, with the two pairs of interleaved sextupoles.

2.5 Luminosity

Luminosity ($\mathcal{L}$) is proportional to the number of collisions that are produced when two beams cross each other. The expression that relates luminosity, cross section (σ) of some event and number of events produced (R) of such kind is given by,

$$R = \mathcal{L}\sigma \tag{2.40}$$

Luminosity will depend, of course, on the bunch population N (assuming an equal number of particles for both beams) and their density distributions within the bunches. Luminosity is determined by the overlap of the core distributions given by the integral,

$$\mathcal{L} = KN^2 \int \rho_{e^+}(x,y)\rho_{e^-}(x,y)dxdy \tag{2.41}$$

where K is the kinematic factor given by $K = \sqrt{(\vec{v}_1 - \vec{v}_2)^2 - (\vec{v}_1 \times \vec{v}_2)^2/c^2}$ and $\vec{v}_{1,2}$ are the velocity vector of the incoming beams, $\rho(x,y)$ is the bunch density distribution of e^- adn e^+ bunches. Assuming Gaussian distributed beams and head-on collisions, luminosity in a linear collider can be reduced to an expression like,

$$\mathcal{L} = \frac{N^2 f_{\text{rep}} n_b}{4\pi\sigma_x^*\sigma_y^*} H_D, \tag{2.42}$$

where f_{rep} is the repetition frequency, n_b the number of bunches per pulse, N the number of particles per bunch and $\sigma^*_{x,y}$ the core horizontal and vertical spot size respectively. Finally, H_D is the enhancement factor due to the pinch effect, the mutual attraction of both beams close to the IP that acts like a strong focalization enhancing the luminosity value. This value is $H_D \approx 2$ for CLIC at 3 TeV [12].

Eq. (2.42) is a first approximation but it is modified when we consider more detailed effects like collisions with crossing angle or the hourglass effect due to the finite length of the bunches. Both are described briefly in the next sections.

2.5.1 Crossing-angle and crab cavity

A horizontal crossing angle between the beams at the IP is introduced in the linear colliders BDS to cleanly extract the spent beam and to allow the IR quadrupoles to fit into the available space (see Fig.

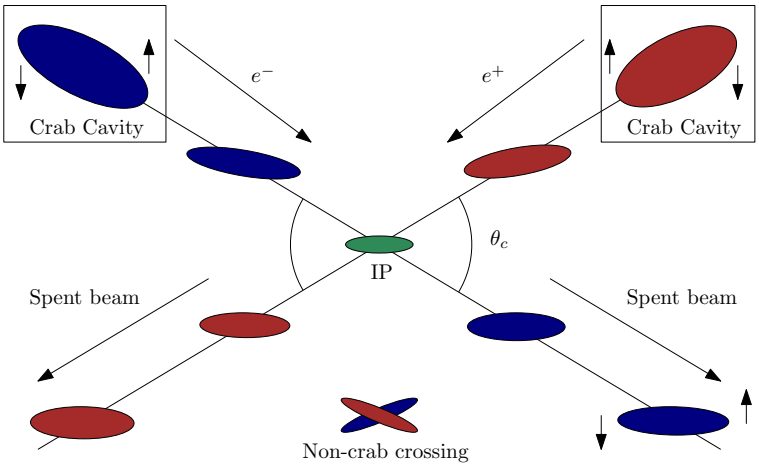

Figure 2.6: Crossing angle scheme and Crab Cavities location.

2.6). This crossing scheme produces a luminosity loss with respect to the head on collision according to,

$$\mathcal{L} \approx \mathcal{L}_{\text{head on}} \frac{1}{\sqrt{1+\Theta}}, \tag{2.43}$$

where Θ is the Piwinski angle, given by,

$$\Theta \equiv \frac{\tan(\theta_c/2)\sigma_z}{\sigma_x}, \tag{2.44}$$

where θ_c is the full crossing angle, σ_z the bunch length and σ_x the horizontal beam size. Since, this luminosity reduction might be significant, some way to compensate this effect while keeping the crossing angle is required. This task is performed by crab cavities. They apply a transverse kick in such a way that the head and the tail of the bunch are kicked in opposite directions resulting into a global rotation of the bunch. The sign of the tilt is such that the two bunches are in line during collision. The final result is that, in the bunch reference system, they interact with zero crossing angle and the luminosity loss due to the crossing angle is recovered.

2.5.2 Hourglass effect

Since the β-functions have their minimum at the IP and increase with the distance, to consider the beam size constant along the whole collision length in some cases is not a good approximation. In a low-β region the β-function varies with the distance s to the minimum (see Fig. 2.7) as:

$$\beta(s) \approx \beta^* \left(1 + \left(\frac{s}{\beta^*}\right)^2\right) \Rightarrow \sigma(s) = \sigma^* \sqrt{1 + \left(\frac{s}{\beta^*}\right)^2}, \tag{2.45}$$

and therefore the beam size increases approximately linearly with the distance to the IP. Because of the shape of the β-function this effect is called the hourglass effect. This is specially important when the β-function is comparable to the bunch length σ_z and not all the particles collide at the minimum of the transverse beam size and therefore a luminosity reduction is observed. In order to reevaluate the expression for the luminosity, we have to take into account the variation of the beam size (β-functions) in the overlapping integral to calculate luminosity. Assuming a symmetric collider with $\sigma_y^* \ll \sigma_x^*$ we obtain a reduction with respect to the nominal luminosity $\mathcal{L}_0$ [39],

$$\frac{\mathcal{L}}{\mathcal{L}_0} = \sqrt{\frac{2}{\pi}} a e^b K_0(b), \tag{2.46}$$

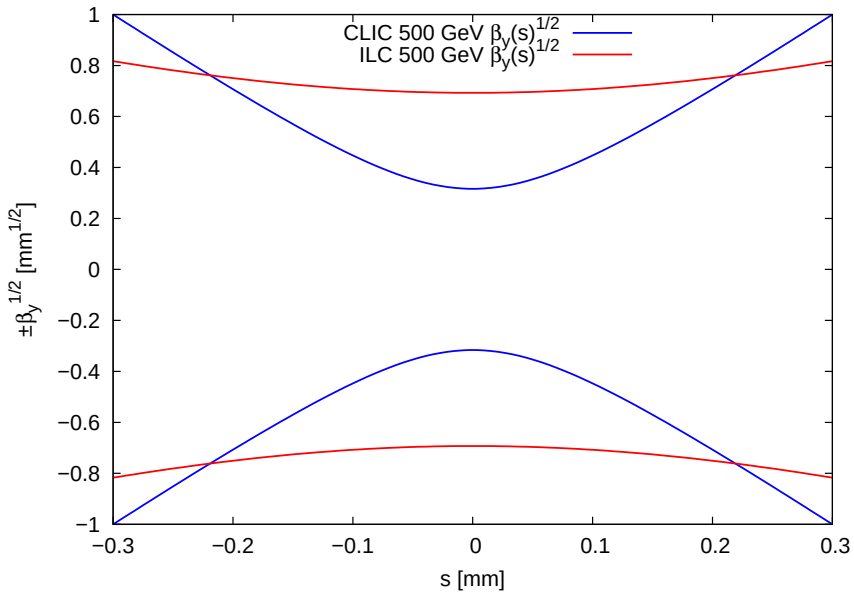

Figure 2.7: Hourglass effect for CLIC and ILC at 500 GeV c.o.m. energy. CLIC $\beta_y^* = 0.1$ mm and ILC $\beta_y^* = 0.48$ mm

where,

$$a = \frac{\beta_y^*}{\sqrt{2}\sigma_z}, \; b = a^2\left[1 + \left(\frac{\sigma_z}{\sigma_x^*}\tan(\theta_c/2)\right)^2\right] \tag{2.47}$$

where K_0 is a Bessel function. This effect gives the optimal value of the vertical β-function at the IP that maximizes luminosity which is usually $\beta_y^* \approx \sigma_z$.

2.5.3 Beam-beam effects

The dynamics of the particles is strongly modified when the beams approach to each other close to the IP and they feel the strong electromagnetic field of the opposite beam [40].The magnitude of the beam-beam effects is often quantified by the so-called disruption parameter $D_{x,y}$ defined as the ratio between the rms bunch length σ_z and the effective focal length $f_{x,y}$ [39],

$$D_{x,y} \equiv \frac{\sigma_z}{f_{x,y}} = \frac{2Nr_e\sigma_z}{\gamma\sigma_{x,y}^*(\sigma_x^* + \sigma_y^*)}, \tag{2.48}$$

where N denotes the number of particles per bunch, γ the relativistic Lorentz factor, and r_e the classical electron radius. If the disruption parameter is small, the beam acts like a thin lens while if it is large, the focal length is shorter than the bunch length leading to a pinch enhancement that can lead to instabilities that can reduce the luminosity in presence of some offsets.

During the collision, particles emit synchrotron radiation in the field of the opposing beam. This radiation is called beamstrahlung and it is characterized by the Υ parameter, which is proportional to the average critical energy [39],

$$\Upsilon = \frac{2\hbar\omega_c}{3E} \approx \frac{5}{6}\frac{\gamma r_e^2 N}{\alpha\sigma_z(\sigma_x + \sigma_y)}, \tag{2.49}$$

where E is the beam energy, $\alpha \approx 1/137$ is the approximation of the fine structure constant, $\omega_c \equiv 3c\gamma^3/(2\rho)$ is the critical frequency characterizing the synchrotron light spectrum, with ρ the bending radius, γ the

Lorentz factor, c is the speed of light and σ_z the bunch length.

$$N_\gamma \approx \frac{5\alpha\sigma_z}{2\gamma\bar{\lambda}_e}\frac{\Upsilon}{(1+\Upsilon^{2/3})^{1/2}} \approx 2\frac{\alpha r_e N}{\sigma_x+\sigma_y}, \tag{2.50}$$

where the last approximation applies if $\Upsilon \leq 1$. The number of emitted photons N_γ should not be much higher than one photon per particle in order to avoid very high backgrounds deposited in the detector.

Flat beams and luminosity

Energy loss due to the Beamstrahlung emission is one of the factors that can reduce the luminosity performance of a linear collider due to high bunch intensities at the IP. Although very small beam sizes increase luminosity, they also increase the number of emitted photons. From Eq. (2.42) and Eq. (2.50) one can deduce that it is desirable to reduce the value of $\sigma_x^*\sigma_y^*$ while keeping $\sigma_x^*+\sigma_y^*$ small enough. The solution is to create flat beams where usually $\sigma_x^* \gg \sigma_y^*$ and therefore the number of photons only depends on the horizontal beam size.

Therefore, because of the Beamstrahlung emission, there will be pairs of particles that will collide at energies different from the nominal c.o.m. energy. In order to evaluate this effect, we define the *peak luminosity* $\mathcal{L}_{1\%}$ and the *total luminosity* $\mathcal{L}_T$. The total luminosity takes into account the luminosity delivered by all the collisions, even if they collide at different energy from the nominal. Peak luminosity only takes into account the luminosity delivered by those collisions produced above the 99% of the nominal energy (denoted as $\mathcal{L}_1\%$). For a Beamstrahlung free collision $\mathcal{L}_T = \mathcal{L}_{1\%}$ while for collisions taking into account Beamstrahlung emission $\mathcal{L}_T > \mathcal{L}_{1\%}$ and a long tail spectra of collisions out of the nominal energy appears.

2.6 Synchrotron radiation

Synchrotron radiation is one of effects that can dilute the beam size and the luminosity in a collider, specially at high energies. This radiation comes from charged particles that suffer a transverse acceleration (changing the direction of motion) and the emission is produced mostly on the plane defined by the particle trajectory.

There are two cases where the synchrotron radiation emission is important in a linear collider: radiation in bending magnets and radiation in quadrupoles, this last effect drives to the Oide effect.

2.6.1 Radiation in bending magnets

Linear colliders suffer from synchrotron radiation in some bending sections due to the very high energy of the particles, mainly in the FFS where bending magnets are needed to generate dispersion for the correction of chromatic aberrations [41].

The horizontal emittance dilution due to synchrotron radiation can be estimated using:

$$\frac{\langle x^2\rangle}{\beta^*} = 4.13\cdot 10^{-11}[\mathrm{m^2GeV^{-5}}]E^5\mathcal{I}, \tag{2.51}$$

where E is the beam energy and $\mathcal{I}$ is the integral given by

$$\mathcal{I} = \int_0^L \frac{\mathcal{H}(s)}{|\rho_x(s)^3|}\cos^2\Phi(s)ds \approx \sum_i L_i\frac{\mathcal{H}_i}{|\rho_{x,i}|^3}\cos^2\Phi_i, \tag{2.52}$$

where L_i is the length of the bending magnet and ρ_i is the bending radius of the i-th dipole magnet and $\mathcal{H}$ is given by

$$\mathcal{H} = \frac{D_x^2+(D_x'\beta_x+D_x\alpha_x)^2}{\beta_x}, \tag{2.53}$$

and $\Phi = \Delta\phi(s\to L)+\arctan(-\alpha-\beta\eta'/\eta)$. The approximation in Eq.(2.52) of the integral by the sum is valid if we split all the bending magnets in short enough slices.

2.6.2 Oide effect

There is an essential limitation on the focusing of electron and positron beams due to synchrotron radiation emission in the quadrupoles, mainly the ones conforming the final doublet of a linear collider [41, 42]. Therefore, there exists a fundamental limit in the minimum spot size at the IP and the final luminosity. The minimum spot size is determined by the emittance of the beam at the entrance of the final focus and the FD parameters, the β^* at the IP and the beam energy. The minimum spot size is given by the expression,

$$\sigma_y^{*2} = \beta_y^* \epsilon_y + \frac{110}{3\sqrt{6\pi}} r_e \lambda_e \gamma^5 F\left(\sqrt{K}L, \sqrt{K}l^*\right)\left(\frac{\epsilon_y}{\beta_y^*}\right)^{5/2}, \tag{2.54}$$

where the function $F\left(\sqrt{K}L, \sqrt{K}l^*\right)$ is defined by:

$$F\left(\sqrt{K}L, \sqrt{K}l^*\right) \equiv \\ \equiv \int_0^{\sqrt{K}L} |\sin\phi + \sqrt{K}l^* \cos\phi|^3 \left[\int_0^{\phi} \left(\sin\phi' + \sqrt{K}l^* \cos\phi'\right)^2 d\phi'\right]^2 d\phi. \tag{2.55}$$

and L is the quadrupole length, l^* is the length of the last drift, K the quadrupole strength and r_e the classical electron radius.

This limit must be taken into account carefully since for CLIC, the nominal spot size is usually very close to the minimum and sometimes, mainly for high energy cases, an optimization of the quadrupole length is needed to keep this limit below the nominal beam size.

2.7 Tolerances

The very small beam sizes required at the IP are translated in very tight tolerances in the last sections of the accelerator, namely the FFS. Small perturbations to nominal values of the magnet strength, position and tilt for example, yield a not perfect focusing at the IP and therefore the increase of the beam size at this point. A misaligned quadrupole focalizes the beam in a different point and a degradation of the beam size at the collision point. All these constraints impose a serious limits to the collider performance and special and effective tuning techniques must be applied in order to reduce their impact.

2.8 Tuning

When we consider realistic imperfections, the machine performance decreases dramatically, typically, the beam size increases and luminosity drops substantially about 6 orders of magnitude. The tuning is the procedure which brings the system performance to its design values. Since the initial errors are unknown, the tuning requires a statistical study. Usually more than 100 machines with randomly distributed errors are considered in computer simulations. The simulated tuning reproduces a realistic tuning procedure in a machine and it is composed of several techniques briefly described below. More information about beam control techniques can be found in [43].

2.8.1 Simplex-Nelder Algorithm

The Simplex-Nelder algorithm is the numerical method commonly used for optimization in nonlinear systems. This technique minimizes a merit function in a multi-dimensional space. For the Final Focus optimization, the merit function is usually the beam size at the IP or the luminosity while the multi-dimensional space is composed of the available machine parameters. Due to the large number of variables to be tuned the convergence of the algorithm could be very slow and is not guaranteed.

2.8.2 Beam Based alignment (BBA)

Some methods are based on the measurement of the beam orbit and its deviation from the nominal path to apply the required changes in the physical elements of the beam line. To implement these techniques a set of Beam Position Monitors (BPM) and correctors are needed. Small dipoles and quadrupole displacements are used as correctors. Two main steering techniques are applied: one-to-one orbit correction and dispersion free steering [43].

One-to-one correction

The orbit correction technique known as one to one steering techniques, minimizes the BPM readings seeking for the flat orbit through the beam line. The beam is deflected to pass through the BPM center and, assuming that the BPM is not offset with respect to the quadrupole, this would show zero displacement. Notice that one-to-one steering generates dispersion and it will contribute to emittance dilution.

Mathematically, in a transport line the beam centroid position measured downstream at location s_j obeys

$$x_j = \sum_{i=0}^{j} \sqrt{\beta_i \beta_j}\theta_i \sin(\phi_j - \phi_i), \tag{2.56}$$

which has contributions from each dipole kick θ_i and depends on the β-functions at the location of the disturbances and at the observation point and on the phases ϕ_i and ϕ_j.

Assuming a set of N BPMs in the beam line, the orbit measured by the monitors is represented by the vector $\vec{b}_N$, while a vector $\vec{C}_M$ represents the strength of M correctors present in the beam line. Activating each corrector one at a time and recording the orbit excitation at all BPMs, the response matrix R_c of the correctors is determined. The orbit corrector algorithm gives optimum strength of the correctors by solving

$$\vec{b}_N + R_c \cdot \vec{C}_M = 0, \tag{2.57}$$

where $\vec{b}_n$ is the vector of the initial BPM readings before correction.

One-to-one steering is usually used during initial commissioning of an accelerator as it is one of the simplest and fastest of all steering algorithms.

Dispersion Free steering

The Dispersion Free Steering (DFS) technique aims to correct the orbit and to match the dispersion $\vec{\eta}$ to its nominal value $\vec{\eta}_0$. The dispersion is measured using two beams with slightly different energies, namely $E \pm \Delta E$, where ΔE is usually a few % of the nominal energy E. The beams with different energies produce two different orbit readings, $\vec{b}_{\Delta E_+}$ and $\vec{b}_{\Delta E_-}$. The measured dispersion is then given by

$$\vec{\eta} = \frac{\vec{b}_{\Delta E_+} - \vec{b}_{\Delta E_-}}{2\Delta E}. \tag{2.58}$$

The matrix D describes the dispersion response of the system to the correctors and it is obtained by activating each corrector sequentially and recording the dispersion deviation from the design value at the BPMs. The optimum strength of the correctors is obtained by solving the equation

$$\begin{pmatrix} \vec{b}_n \\ \vec{\eta} - \vec{\eta}_0 \end{pmatrix} + \begin{pmatrix} R_c \\ D \end{pmatrix} \cdot \vec{C}_M = 0. \tag{2.59}$$

where $\vec{C}_M$ represents the vector containing the strengths of the M correctors.

Dispersion-free-steering is an algorithm which corrects the dispersive errors from misaligned quadrupoles. This technique proved crucial for maintaining stable linac emittances at the SLC [44].

Tuning knobs

A knob is a combination of available variables (quadrupole strength, corrector strength, sextupole positions, ...) that are simultaneously changed with the proper ratio and relative sign in such a way that only the aberration of interest is corrected. Knobs were used to minimize the spot sizes at the SLC interaction point and to produce the maximum luminosity. The spot sizes at the IP are routinely optimized by correcting the most important low-order aberrations including waist shift, dispersion and skew coupling using the knobs which consisted of orthogonal linear combinations of the strengths of normal quadrupoles and skew quadrupoles.

Nowadays, there are some facilities that use this correction system like ATF2 and it is one of the basic tools for tuning simulations for linear collider luminosity optimization where transverse sextupole positions are used as knobs. The ATF2 FFS has five sextupoles (SF6, SF5, SD4, SF1 and SD0) and therefore, there are ten free parameters to adjust (5 per plane). A displaced sextupole generates a normal and a quadrupole field that can compensate some aberrations present at the IP. The general method to construct such knobs is the Singular Value Decomposition (SVD) which is a procedure for solving systems of linear equations with either too many or too few variables. The problem can be cast into a matrix equation of the form,

$$\begin{pmatrix} \Delta\beta_x \\ \Delta\alpha_x \\ \Delta\mu_x \\ \Delta\eta_x \\ \Delta\eta'_x \\ \Delta\beta_y \\ \Delta\alpha_y \\ \Delta\mu_y \\ \Delta\eta_x \\ \Delta\eta'_x \end{pmatrix} + \begin{pmatrix} B_{11} & B_{12} & \dots & B_{1N} \\ B_{21} & B_{22} & \dots & B_{2N} \\ & \dots & \dots & \\ B_{M1} & B_{M2} & \dots & B_{MN} \end{pmatrix} \begin{pmatrix} \Delta K_1 \\ \Delta K_2 \\ ... \\ \Delta K_N \end{pmatrix} = 0. \tag{2.60}$$

where the first vector is the vector that contains the observable quantities to be corrected, the B matrix is the response matrix that relates the knobs K with the observables [43].

The response matrix B may be obtained using the optics model or it may be determined by measuring the optics directly from the machine. To optimally constrain the solution, the number of adjustable parameters N should be larger or equal to the number of constraints M. The use of nonlinear knobs (knobs based on nonlinear responses) was also explored in SLC [61] and are currently being considered in the ATF2 operation.

Chapter 3

Comparison of traditional and compact Final Focus Systems

Along the introductory chapter, the two main Final Focus System schemes, one with local and non-local chromatic correction, have been described. In this chapter a full comparison of the performance of both schemes for CLIC running at 3 TeV and 500 GeV c.o.m. energies is done. In this chapter, we focus the study on the correction of the nonlinear aberrations, luminosity performance and tuning simulation.

3.1 FFS Optics Design

As we have seen, both schemes are relatively different from the point of view of the optics design and on how chromaticity is corrected. In this section we describe in detail the lattice configurations of both systems for CLIC at 500 GeV and 3 TeV c.o.m. energy.

The optics corresponding to the local chromaticity correction lattice scheme are taken from the lattice repository [53,54] and no major changes have been done except for a minor rematching of the quadrupole strengths in order to slightly change the value of the β-functions at the IP and the corresponding sextupole strength rematching.

The work of this thesis has been focused on the optimization of the traditional FFS. The optics for the traditional chromatic scheme has been firstly generated by FFADA (Final Focus System Automatic Design and Analysis) [45]. FFADA is a program which allows the user to automatically design a generic final focus system corresponding to a set of some basic beam and machine input parameters. It also derives the properties of the designed system in terms of momentum acceptance, tracking, collimation requirements and Oide effect. The FFADA output is a file written in MAD8 that is converted to MADX [46] afterwards.

Once the linear optics is perfectly matched to the desired values using MADX, nonlinear optimization of sextupoles is required. This nonlinear optimization of sextupole strengths is carried out using MAPCLASS [47,48]. MAPCLASS is a code written in Python conceived to optimize the linear and nonlinear aberrations of Final Focus Systems. MAPCLASS needs the output of MADX-PTC [52] to obtain the coefficients of the map and uses optimization algorithms like the Simplex minimization algorithm to compensate the high order aberrations. Newer versions of MAPCLASS can run independently of PTC generating the transfer map and evaluating the beam size at the IP [49].

3.1.1 Traditional Chromaticity correction scheme

The Traditional Chromaticity correction scheme is composed of four main sections: the matching section (MS), the horizontal chromatic correction section (CCX), the vertical correction section (CCY) and the final transformer (FT). The following describes both, the lattice for CLIC at 3 TeV and 500 GeV c.o.m. energy.

Table 3.1: CLIC Design parameters at two different stages of the program, 500 GeV and 3 TeV center of mass energy [12]. The energy spread σ_δ represents the full width of a flat distribution.

Parameter [Units]	3 TeV	500 GeV
Center of mass energy $E_{\rm CM}$, [GeV]	3000	500
Repetition rate $f_{\rm rep}$, [Hz]	50	50
Bunch population N_e [10^9]	3.72	6.8
Number of bunches n_b	312	354
Bunch separation Δt_b, [ns]	0.5	0.5
Accelerating gradient G, [MV/m]	100	80
Bunch length σ_z, [μm]	44	72
IP beam size σ_x^*/σ_y^*, [nm]	40/1	200/2.26
Beta function (IP) β_x^*/β_y^*, [mm]	7/0.068	8/0.1
Norm. emittance (IP) ϵ_x/ϵ_y, [nm]	660/20	2400/25
Energy spread σ_δ, [%]	1.0	1.0
Luminosity $\mathcal{L}_{\rm T}$ [$10^{34}{\rm cm}^{-2}s^{-1}$]	5.9	2.3
Power consumption $P_{\rm wall}$, [MW]	589	272
Site length, [km]	48.3	13.0

- Matching section (MS): The MS is composed of four quadrupoles that match the incoming optical functions $(\beta_x, \beta_y, \alpha_x, \alpha_y)$ from the collimation section to the nominal values at the IP.
- Horizontal chromatic correction section (CCX): The CCX section is composed of 10 quadrupoles. Two of them are placed at the entrance and the exit of the section with the same strength with a length of 0.5 m. The other 8 quadrupoles have the same absolute strength and a length of 1.0 m, and the alternate focusing and defocusing quadrupoles. In between of such quadrupoles, long and weak bending magnets create the required dispersion for the chromatic correction. In the high-β regions 4 sextupoles are placed in pairs at both sides of a quadrupole. The length of the sextupoles is 0.5 m but this length might be increased or shortened once the final strength of the sextupole is optimized and in case of a very high pole tip field. There is enough space to increase sextupole length without affecting the general layout of the scheme.
- Vertical chromatic correction section (CCY): The CCY section follows the same structure of the CCX section. In this case the product of β_y at the sextupole times the sextupole strength must be higher than in the horizontal correction section since the vertical chromaticity at the IP is also larger than in the horizontal plane. In this section, sextupole strength and length must be chosen appropriately in order to avoid very high magnetic fields.
- Final Transformer (FT): This is a dispersion free region that applies the final demagnification of the beam by means of the Final Doublet (FD). This is the main source of chromatic aberrations due to the high strength of the quadrupole magnets that compose the FD. It contains the last drift that determines the distance from the last quadrupole to the IP, L^*.

The optics layout [53,54] and the optical functions for this scheme are shown in Fig. 3.1 top for 3 TeV and in Fig. 3.2 top for 500 GeV. A top view of the layout at 3 TeV is also shwon in Fig. 3.3.

Brinkmann optics

In order to increase the energy acceptance of the FFS, Brinkmann proposed in [55] to add extra sextupoles all along the chromatic correction sections. This allows to relax the main sextupoles and to increase the energy acceptance. We follow this approach in order to increase the luminosity of the system adding 4 more sextupoles in each chromatic correction section. Two pairs of octupoles, in the FD region

and a second pair upstream, are also added in order to correct the remaining geometrical aberrations introduced by the sextupoles. As we will see, the introduction of extra sextupoles, although it increases the luminosity,makes more complex the tuning of such machines.

3.1.2 Local Chromaticity correction scheme

The local chromaticity correction scheme is more difficult to design from scratch [38] and it does not present the clear modular structure of the traditional correction scheme. Nevertheless we can differentiate four main sections.

- Matching section (MS): As in the previous case, it is composed of four quadrupoles that match the incoming optical functions to the nominal values at the IP.
- Second doublet (SD): A second quadrupole doublet is used to put a pair of sextupoles interleaved with them in order to cancel the geometric aberrations introduced by the pairs of sextupoles in the FD region.
- Bending section (BS): The bending section is located between the two quadrupole doublets and generates the required dispersion for the correct cancellation of the chromatic aberrations. The dispersion has its peak in the FD region.
- Final Transformer (FT): Unlike the traditional FFS, in this case the FD is not a dispersion free region since a pair of sextupoles, SF1 and SD0, is interleaved with the two final quadrupoles, QF1 and QD0. The dispersion vanishes at the IP but its derivative does not.

The lattice designs following such scheme for 3 TeV and 500 GeV are taken from the existing designs from the lattice repository [57, 58] and we just have to rematch the incoming functions to slightly vary the parameters at the IP but always keeping the main sctructure of the design. The optics layout and the optical functions for this scheme is shown in Fig. 3.1 bottom for 3 TeV and in Fig. 3.2 bottom for 500 GeV.

3.2 Final Focus Systems Optimization

The nonlinear optimization of the Final Focus System consists of matching the strengths of the quadrupoles, sextupoles and higher order multipoles in order to reduce the transverse beam size compensating nonlinear aberrations. In Table 3.2 the chromaticity for both systems at different energies is computed using Eq. (2.33) and compared to the beam size increase. One can see that at 3 TeV the chromaticity is much larger for the initial design of the traditional scheme than for the local scheme. This is due to the fact that a maximum length for the FFS of 1.5 km is imposed, half of the length of the proposed FFS in [60], in order to reduce the total cost of the system. This requires very high intermediate β-functions for chromatic compensation increasing the total chromaticity of the system. The large β-functions can be compared in Fig. 3.1. At 500 GeV the peak β-functions are comparable and therefore the value of chromaticity similar. In the next sections we optimize the traditional scheme reducing the β-functions at the intermediate quadrupoles in order to reduce chromaticity.

The length of the last drift (L^*) and the length and strength of the last quadrupole (QD0) are summarized in Table 3.3 for both schemes. At 3 TeV, the local correction scheme uses six sextupoles following the scheme given in [25] and two octupoles and one decapole in the FD region, as presented in [12], Fig. 3.1 (top). At 500 GeV five sextupoles are used for the chromatic correction, Fig. 3.2 (top). The traditional scheme uses, for both energies, four pairs of main sextupoles (two pairs in CCX and two pairs in CCY) and eight more weak sextupoles to increase the momentum bandwidth following the idea presented in [55]. Two pairs of octupoles are also introduced, a pair in the FD region and a second pair upstream in opposite phase with the first one. The layout of such systems is shown in Fig. 3.1 (bottom) and Fig. 3.2 (bottom). Since no dodecapoles or higher order multipoles are present in the beamlines,

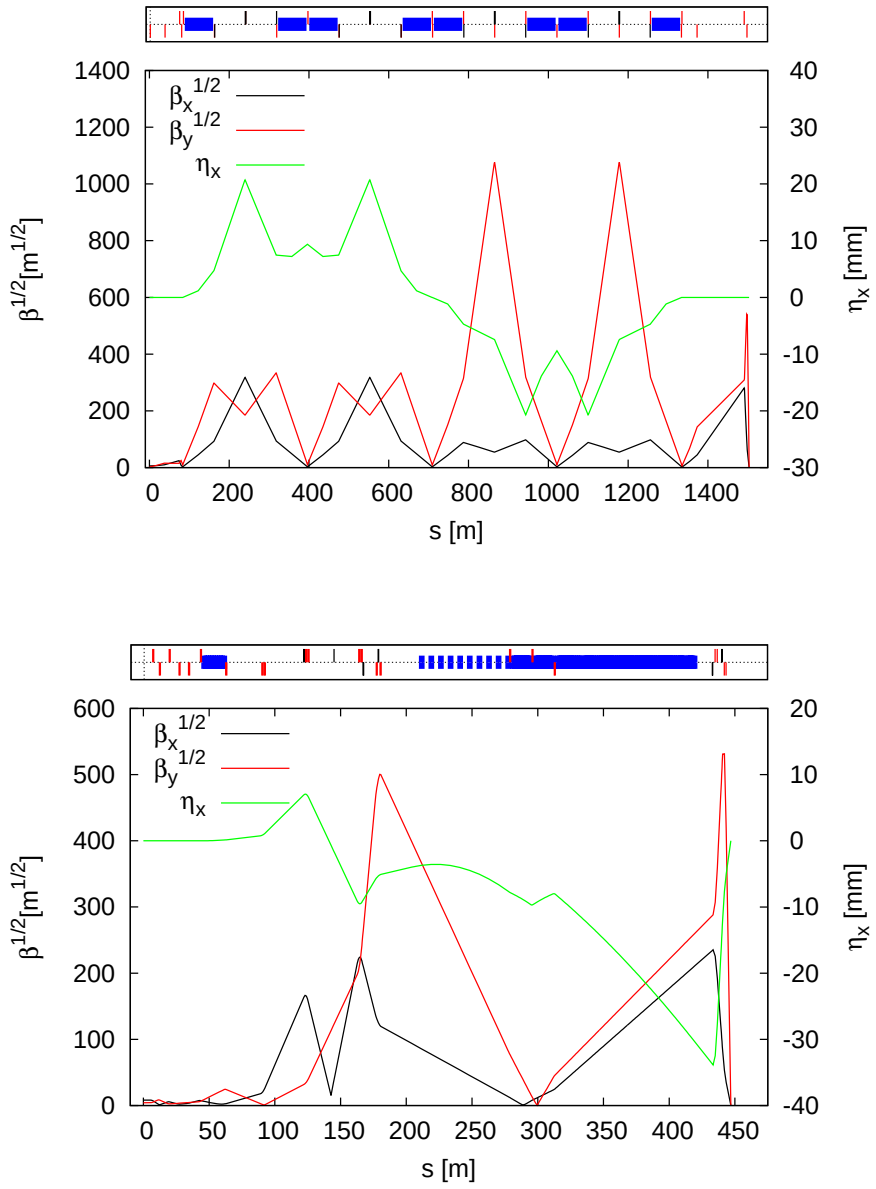

Figure 3.1: Optics of the CLIC 3 TeV local correction scheme (bottom) and dedicated correction scheme (top) final focus system showing horizontal and vertical β-functions and dispersion function.

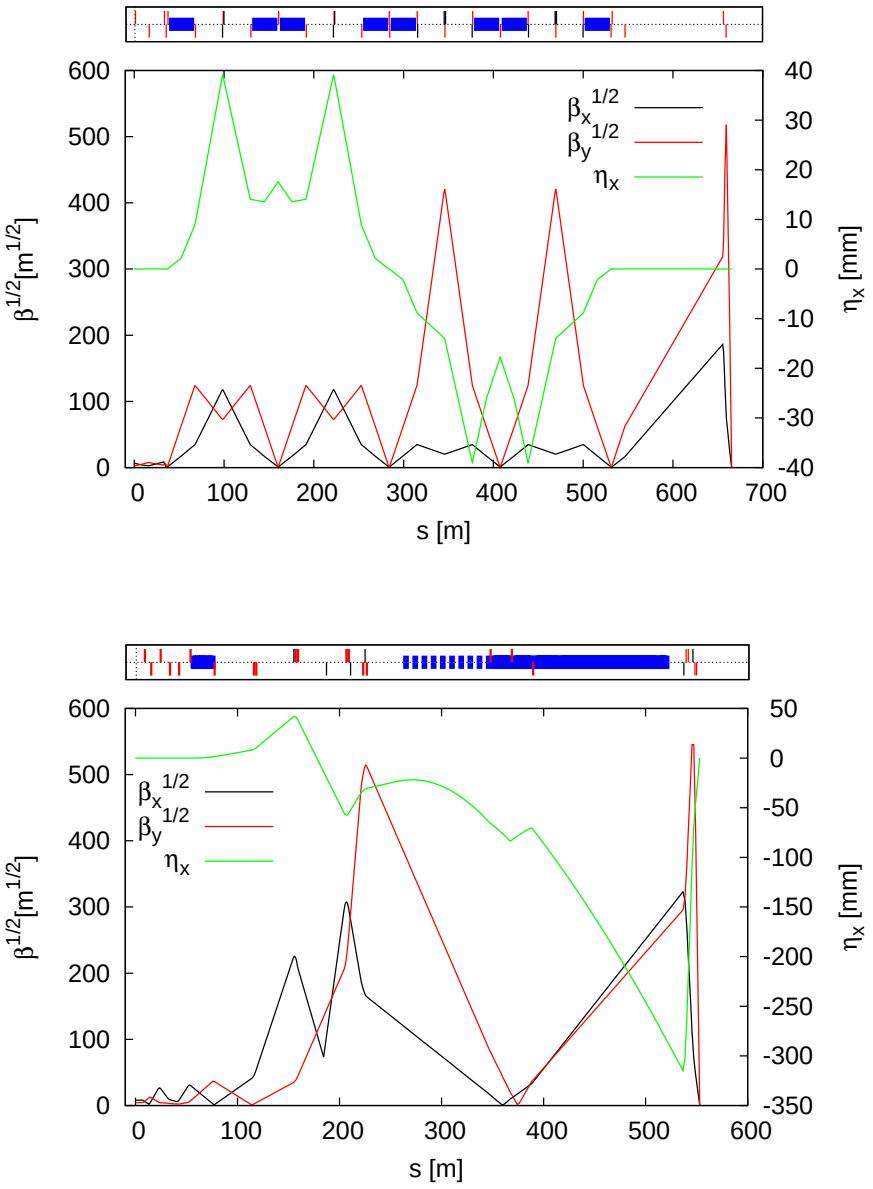

Figure 3.2: Optics of the CLIC 500 GeV local correction scheme (bottom) and dedicated correction scheme (top) final focus system showing horizontal and vertical β-functions and dispersion function.

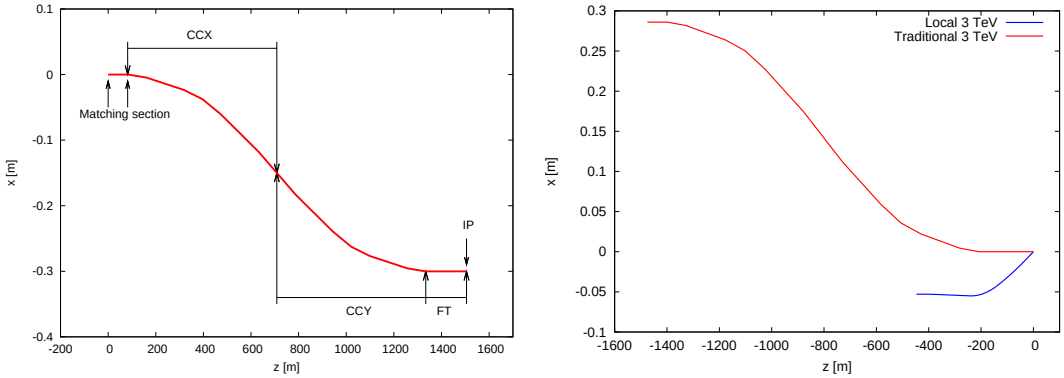

Figure 3.3: Top view of the Final Focus geometry for the Traditional scheme at 3 TeV (left) and the comparison with the local scheme (right) with the IP in the point where the two lines converge.

Table 3.2: Chromaticity calculated using Eq. (2.33) and beam size increases due to uncorrected aberrations. We see an agreement for $\sigma_\delta = 1\%$ between formula and simulation.

Scheme	Energy [GeV]	L_{FFS} [m]	ξ_y	$\sigma_y^*/\sigma_{y,0}^*$
Local	3000	447	23786	237.7
Traditional	3000	1505	31258	312.1
Local	500	553	19231	197.8
Traditional	500	660	22186	227.9

contributions beyond order 6 become negligible. One can see this on Fig. 3.9 where beyond order 6, contributions of higher order aberrations are very low. The results are in agreement with the nonlinear optimization obtained in [47] for the 3 TeV case.

3.2.1 Reducing the β-function at the sextupoles

Since dispersion at the sextupole location is limited by synchrotron radiation, the β-functions at that locations must be high enough to keep the sextupole strength below the maximum achievable magnetic field while keeping the sextupole length in a technically reasonable value (0.5-1 m). From previous results at 3 TeV, one can see that the values of β_y at the sextupole locations are of about 1400 km. Such high values drive a higher chromaticity of the system as we can see in Table 3.2 and Table 3.4 and also might reduce the tuning performance since regions with high β-functions are more sensitive to errors. In order to reduce these effects, one can lower the β_y value at the sextupole locations. Since the product βk_s must

Table 3.3: Final doublet characteristics for both schemes at 3 TeV and 50 GeV c.o.m. energy.

Scheme	E_{cm} [GeV]	L^* [m]	L_{QD0} [m]	K_{QD0} [m^{-1}]	L_{QF1} [m]	K_{QF1} [m^{-1}]
Local	3000	3.5	2.7	-0.32	3.26	0.13
Traditional	3000	3.5	2.7	-0.32	3.27	0.11
Local	500	4.3	3.3	-0.26	4.0	0.11
Traditional	500	4.3	1.3	-0.54	0.88	0.42

Table 3.4: Sextupole strength comparison for different configurations of β_y^s and sextupole lengths.

Scheme	L_s [m]	k_s [m^{-2}]	β_y^s [km]	$B_s^{\max}$ at 5 mm [T]	ξ_y	$\mathcal{L}_T$ [$10^{34}\,cm^{-2}s^{-1}$]
High β	0.5	11.6	1000	0.93	31258	7.5
Low β	0.5	44.0	260	3.51	23469	7.2
Low β	0.85	20.5	259	1.63	23469	7.4
Int. β	0.7	18.1	536	1.44	26335	7.4

be preserved, this will imply stronger sextupoles. Therefore, a compromise between tuning performance and sextupole strength must be found. As first iteration, we reduce the β_y-function until reaching a similar value of the β_y-function at the FD region. This implies a reduction of the β_y-function at the sextupole locations by almost a factor 4. The resulting optics after reduction of the β-functions is shown in Fig. 3.4.

After nonlinear optimization a similar performance compared to the case with high β-functions at the sextupoles in terms of luminosity is reached. The main issue is that for sextupoles of 0.5 m in length, due to the decrease of the β-functions at the sextupoles, the required gradient exceeds the normal conducting regime and therefore a superconducting sextupole is needed. This option is technically being explored and it does not seem a challenge beyond our capabilities. Another possibility is to increase the sextupole length in order to reduce the gradient. We consider sextupoles of 0.85 m, already in the normal conducting regime. Although the dynamics of the system in terms of the compensation of nonlinearities is similar to the case with shorter sextupoles, it will have an important impact on the tuning performance.

A second alternative was studied as a halfway between the two systems considered previously. In order to avoid such strong sextupole fields that require the use of superconducting technologies, we double the β-functions at the sextupole locations with respect to the last case. This allows relaxing sextupole strengths and using normal conducting technologies. In Table 3.4 the sextupole strengths and the corresponding pole tip fields at 5 mm are shown for different vertical β-functions at the sextupoles and different sextupole lengths. The performance of this last system is the best in the normal conducting regime.

3.2.2 Apertures and pole tip field

With the available warm technology magnets with a peak field of 2 Tesla are achievable. This magnetic field is calculated at the aperture, i.e, the inner radius of the magnet. This radius needs to be sufficiently large to host the beam and the halo coming from the collimator. The aperture is defined to be the largest value between $15\sigma_x$ (15 times the horizontal beam size at that location) and $50\sigma_y$ (50 times the vertical beam size at that location).

The magnetic field of the different elements determines the technical feasibility of the different elements of the line. According to the calculated aperture (Ap), the peak magnetic field in a quadrupole can be estimated using,

$$B_q[T] = 3.33p[\mathrm{GeV/c}]k_q Ap. \tag{3.1}$$

Similarly for a sextupole in the horizontal plane,

$$B_x^s[T] = 3.33p[\mathrm{GeV/c}]k_s\frac{Ap^2}{2} \tag{3.2}$$

where p is the momentum of the beam, k_q and k_s are the quadrupole and sextupole gradients respectively and Ap is the required aperture determined by the beam sizes.

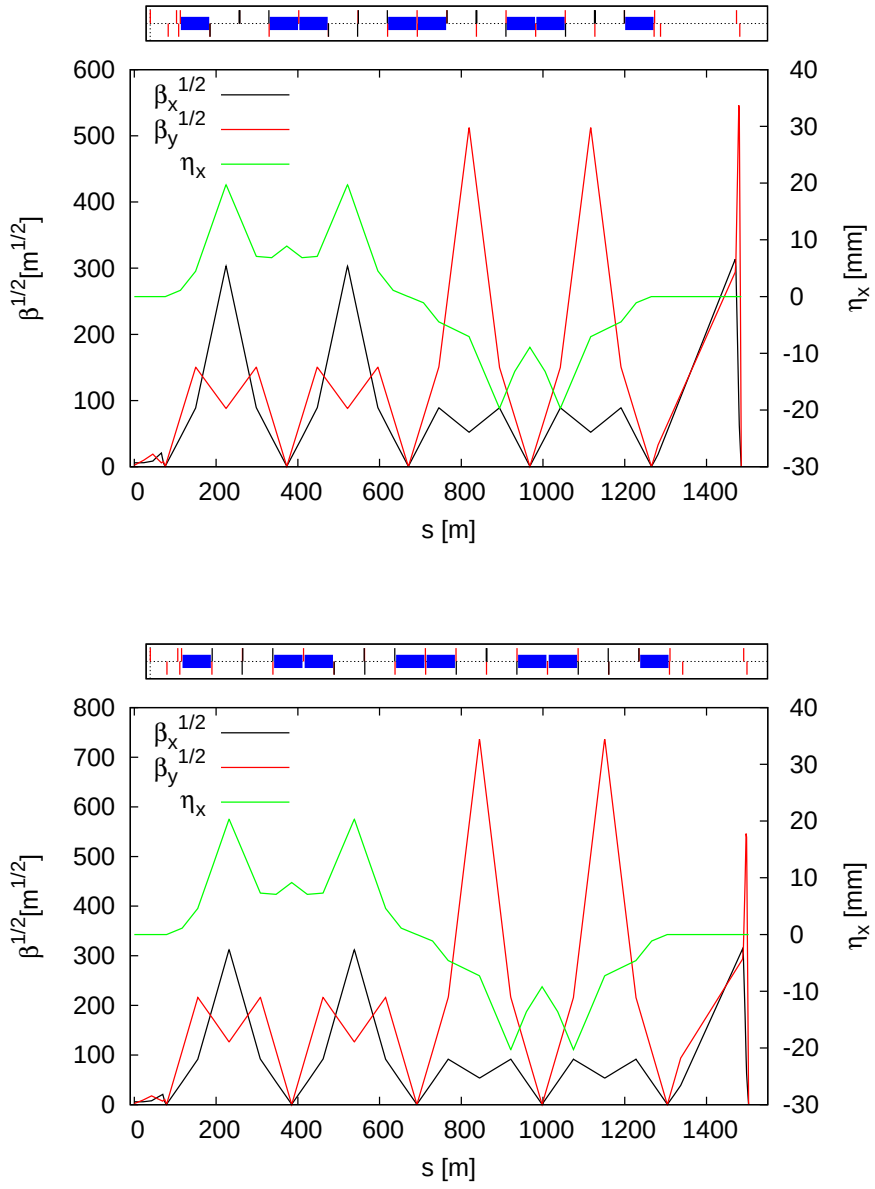

Figure 3.4: Optics for two configurations of the CLIC 3 TeV dedicated correction scheme FFS with reduced β_y-function at the sextupoles of CCY showing horizontal and vertical β-functions and dispersion function.

3 TeV

The results for the apertures and quadrupole tip field at $15\sigma_x$ and $50\sigma_y$ for the Traditional correction scheme are shown in Fig. 3.5 and for the local scheme are shown in Fig. 3.6. In both cases we observe that apertures are below 5 mm and the pole tip field remains always below 2 T.

500 GeV

The results for 500 GeV c.o.m energy for the Traditional correction scheme are shown in Fig. 3.7 and for the local scheme are shown in Fig. 3.8. The first thing one can observe is that in the Traditional design, although apertures are smaller than in the 3 TeV case, the FD quadrupoles are of about 2 T. This is due to the fact that, as we can see in Table 3.3, the Final Doublet quadrupoles are shorter compared to the local scheme. This is translated into a higher gradient and therefore a higher magnetic field. Since there is room to allocate longer quadrupoles, in principle, it will not create major issues if lower magnetic gradients are preferred.

In the case of the Local chromatic scheme, we observe a very large aperture in the FD region. This is caused by the high dispersion present in the horizontal plane. Nevertheless, the pole tip field remains below 1 T all along the line.

3.2.3 Synchrotron radiation

Synchrotron radiation in bending sections (required to create the needed dispersion for chromaticity correction) is one of the major issues that creates beam size dilution at the IP, more notably at high energies. Another effect related to the synchrotron radiation is the so called Oide effect [42]. There exists a limit in the beam demagnification due to the radiation in the Final Doublet quadrupoles. Both effects contribute to the beam dilution: radiation in bending magnets mainly dilutes the horizontal beam size while Oide effect affects mainly the vertical beam size.

Table 3.5: Synchrotron radiation contribution due to bending magnets and quadrupole magnets effect in % of the RMS beam size.

Scheme	E_{cm} [GeV]	$\Delta\sigma_x/\sigma_{x0}$ (Bend) [%]	$\Delta\sigma_y/\sigma_{y0}$ (Quads) [%]
Local	3000	15.0	110
Traditional	3000	10.2	78.8
Local	500	0.2	1.6
Traditional	500	0.1	47.7

Bending magnet strength must be optimized to provide enough dispersion for the chromaticity correction but low enough to keep synchrotron radiation effects low. Therefore, a scan of the bending angle is done during the design and optimization. In Table 3.5 the effects of synchrotron radiation in the transverse beam sizes after optimization are summarized. At 3 TeV, the horizontal beam size blow up is kept under control since the strength of the bending magnets has has been optimized with that purpose. The vertical beam size is strongly affected by the radiation in the last quadrupoles but this effect is not fully reflected in luminosity since the impact is mostly present in the tails of the beam (i.e. increasing the rms beam size) but the core of the beam remains practically unperturbed and therefore, luminosity is not seriously affected.

At 500 GeV, the effect of the synchrotron radiation is very low in the horizontal plane since the energy is relatively low and the bending magnets weak enough. In the vertical plane the local scheme presents also a very low impact on the beam size. This is not the case of the traditional scheme. We have observed that this is caused by the short length of the last quadrupole compared to the one used in

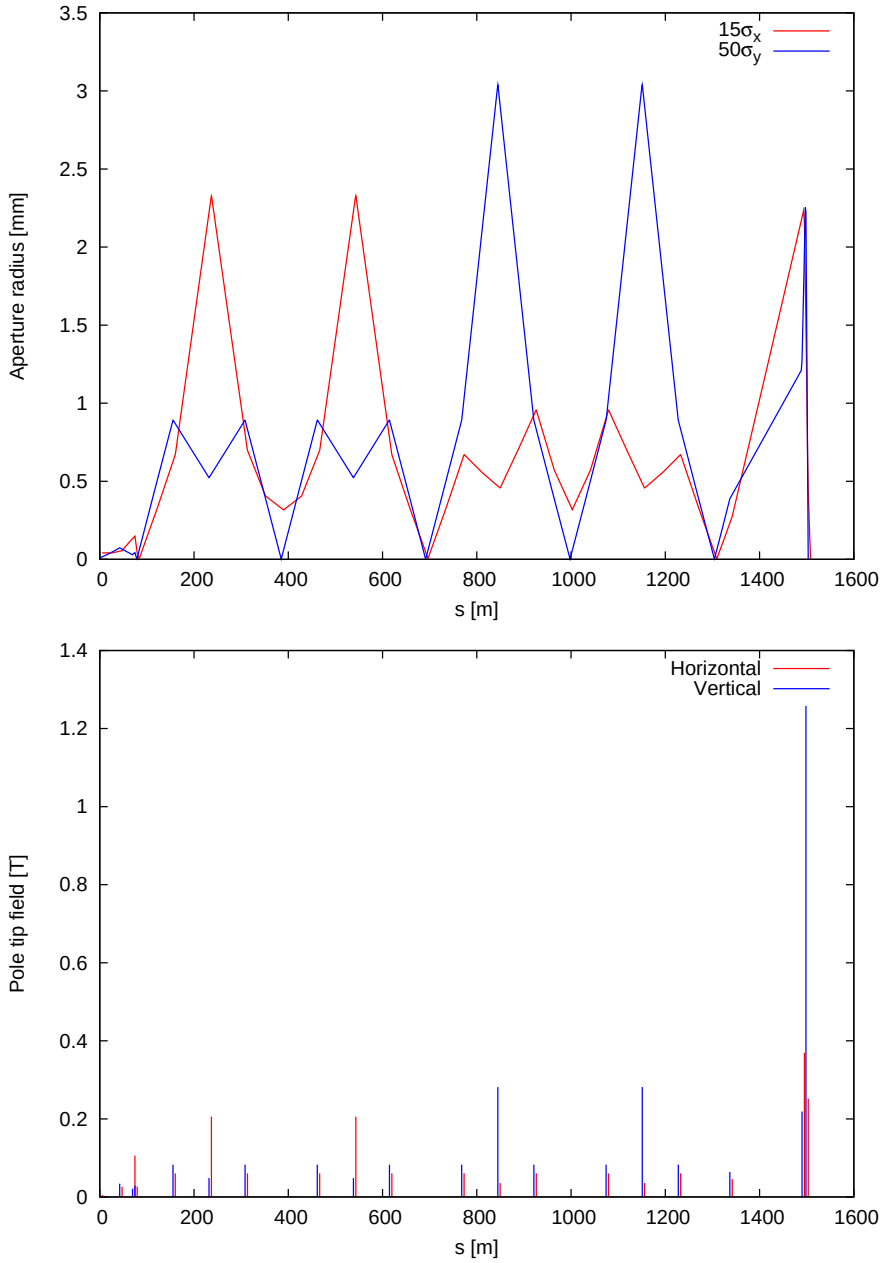

Figure 3.5: Apertures and quadrupole pole tip field at $15\sigma_x$ and $50\sigma_y$ for the traditional chromatic correction scheme at 3 TeV c.o.m. energy

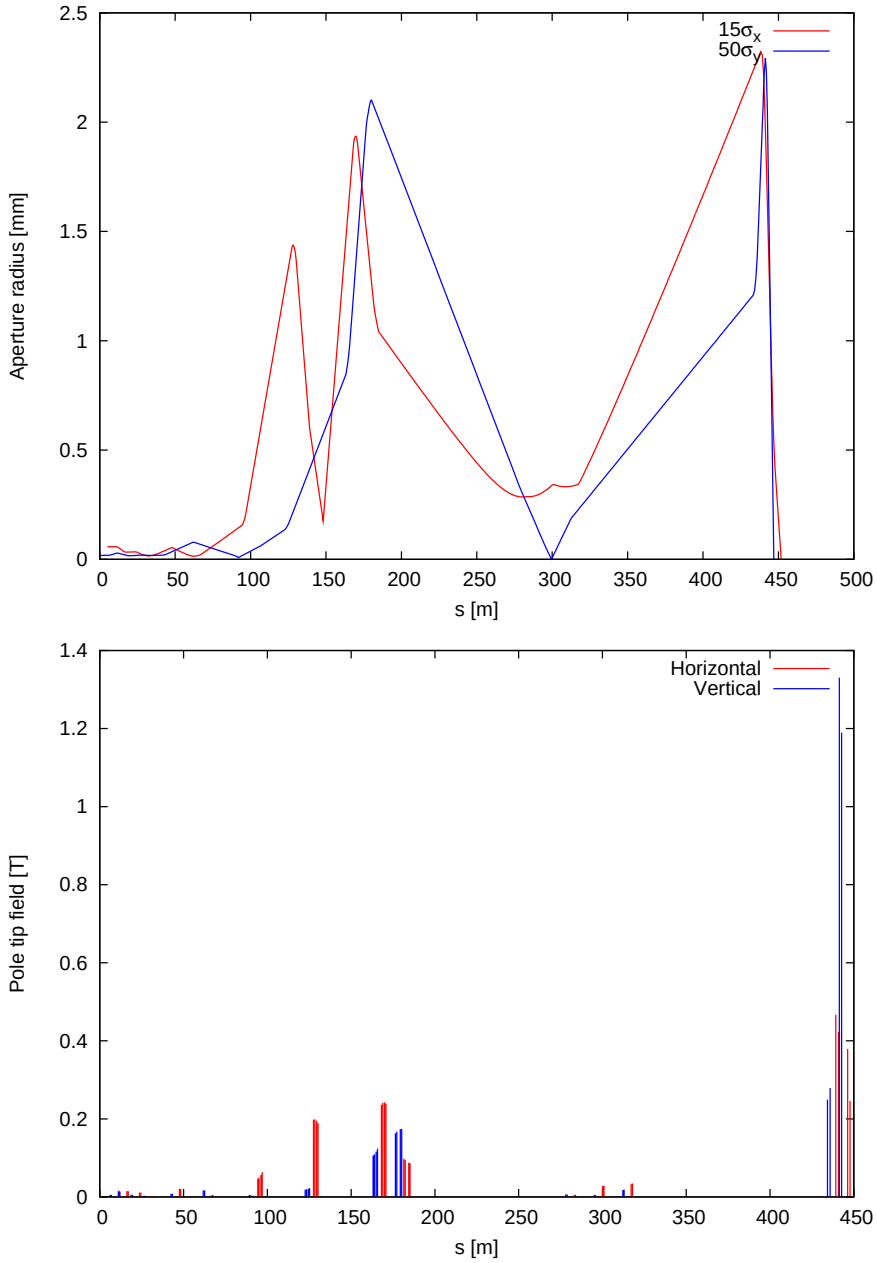

Figure 3.6: Apertures and quadrupole pole tip field at $15\sigma_x$ and $50\sigma_y$ for the local chromatic correction scheme at 3 TeV c.o.m. energy

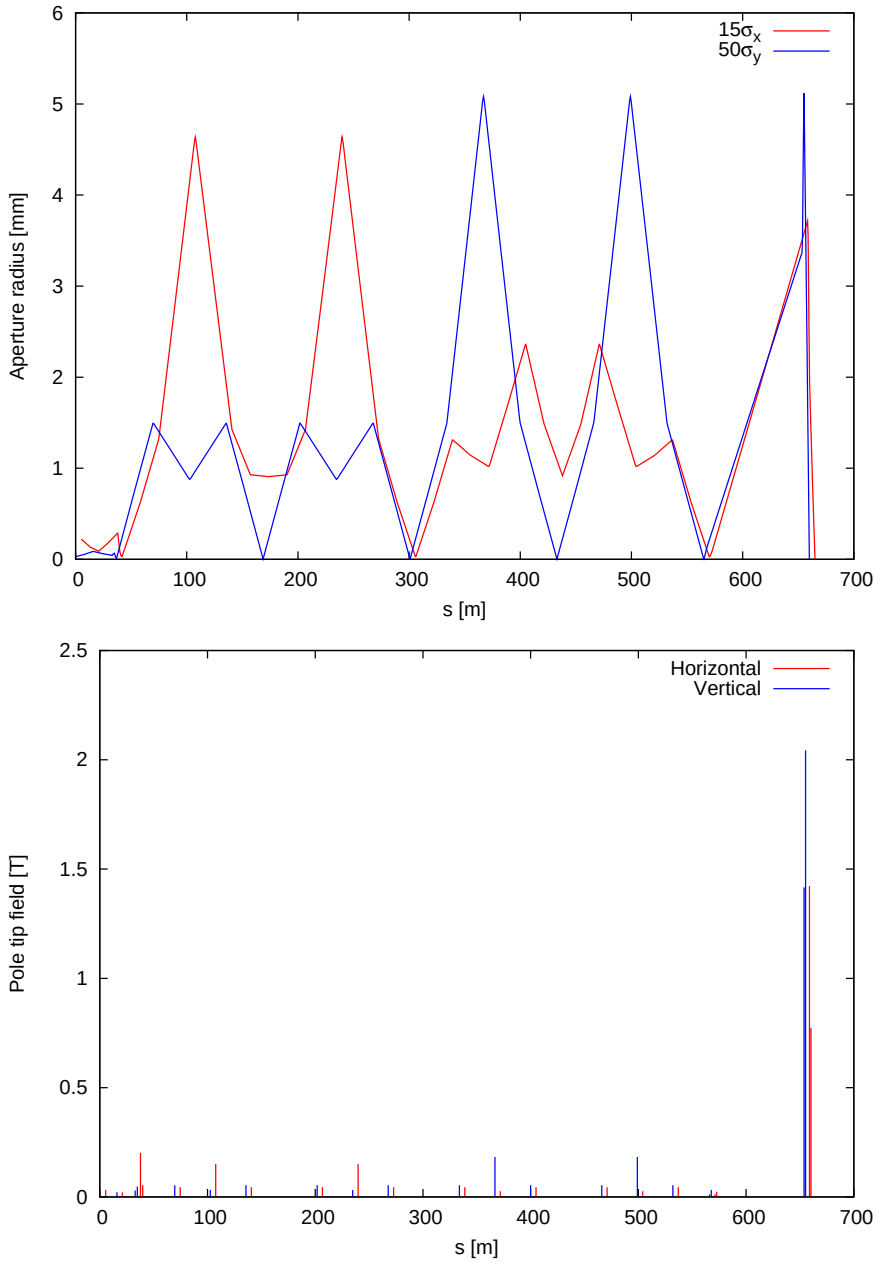

Figure 3.7: Apertures and quadrupole pole tip field at $15\sigma_x$ and $50\sigma_y$ for the traditional chromatic correction scheme at 500 GeV c.o.m. energy

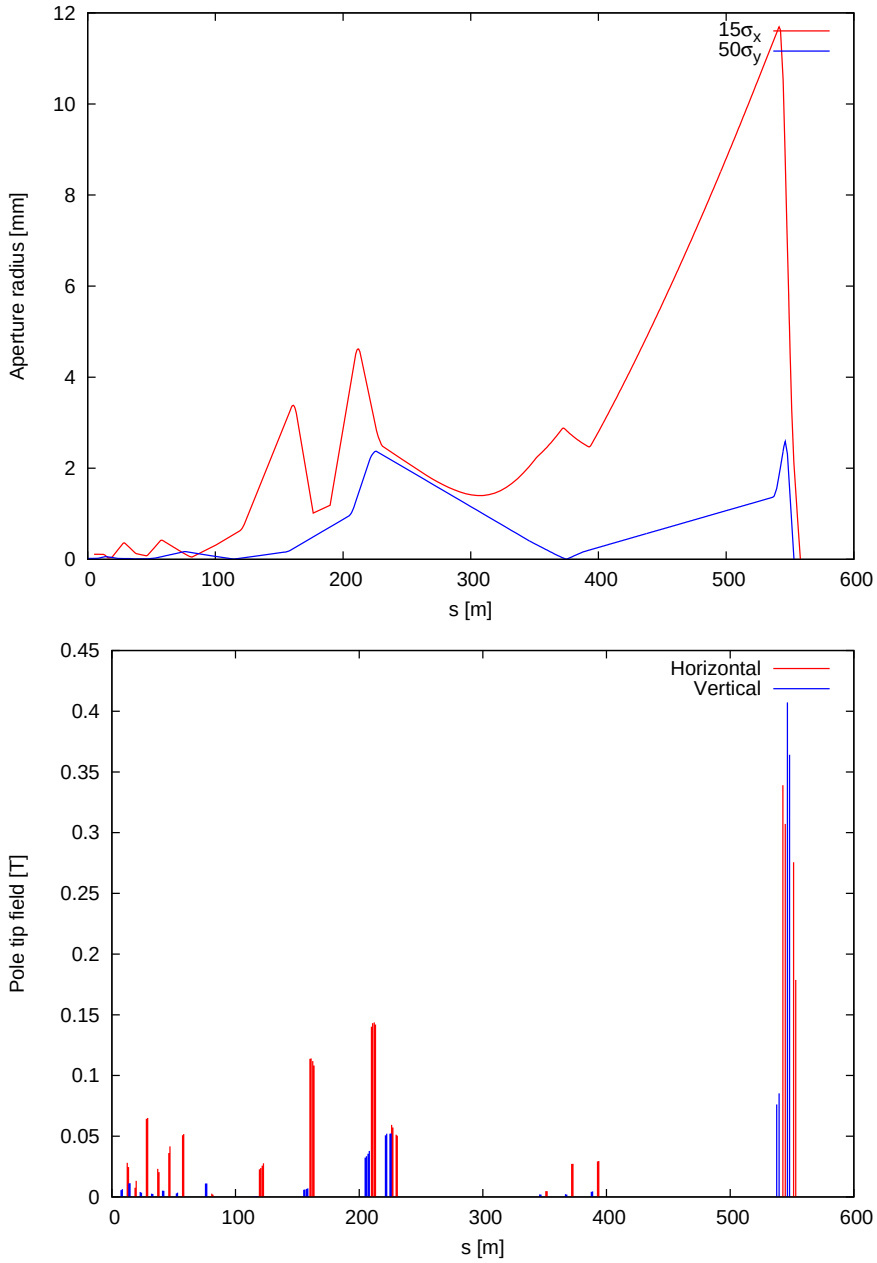

Figure 3.8: Apertures and quadrupole pole tip field at $15\sigma_x$ and $50\sigma_y$ for the local chromatic correction scheme at 500 GeV c.o.m. energy

Table 3.6: Total and peak luminosity (from particles with at least 99% of the nominal energy) computed using GuineaPig for local and traditional systems at high an low energies. The last column shows the contribution of the synchrotron radiation in the peak luminosity.

Scheme	Energy [GeV]	$\mathcal{L}_{\mathrm{T}}$ [$\mathrm{cm}^{-2}\mathrm{s}^{-1}$]	$\mathcal{L}_{1\%}$ [$\mathrm{cm}^{-2}\mathrm{s}^{-1}$]	$\mathcal{L}_{1\%}/\mathcal{L}_{1\%}^{(\mathrm{w/o\ SR})}$
Local	3000	7.8	2.4	0.79
Traditional	3000	7.5	2.4	0.76
Local	500	2.3	1.4	0.99
Traditional	500	2.2	1.3	0.94

the local scheme. Although, as it has been explained before, it does not cause a big impact on the final luminosity, its length should be increased in order to fully optimize the system.

3.3 Luminosity performance

Simulations of beam collisions and luminosity computation is performed with GuineaPig [71] [72]) after tracking particles through the FFS with PLACET [73]. Both electron and positron lines are considered symmetrical and the beam offset at the IP is automatically corrected.

The values of luminosity after beam tracking through the Final Focus System and collision simulation are summarized in Table 3.6. At 3 TeV, the optimization of both schemes give a luminosity above the value given in Table 3.1. This extra luminosity can be used as a budget for imperfections. The traditional scheme gives a 4% lower total luminosity with respect to the local scheme. This comes mainly from the impact of nonlinear aberrations in the horizontal plane as can be observed in Fig. 3.9 (top) ofter an optimization of the beam size order by order. Due to the length limitation of the traditional scheme explained above and the weakness of the bending magnets in order to reduce synchrotron radiation effects, the dispersion function at the sextupole positions is not enough for a better chromatic correction. At 500 GeV, the nonlinear optimization of the beam size is also performed presenting similar results for both schemes as can be seen in Fig. 3.9. Total luminosity given by simulations of the local scheme is exactly the same value shown in Table 3.1. As in the previous case, the traditional scheme presents a lower performance in terms of total luminosity with respect to the local scheme but only by a 4% less total luminosity but achieving the same peak luminosity. At low energies, both schemes present similar performance keeping their length within a reasonable value.

3.3.1 Energy acceptance

The primary design of the Final Focus System is made considering that the beam energy is exactly the nominal value. However, some small departures of the beam energy from its nominal value can occur due to a great variety of causes: losses by radiation or instabilities in the source and the linac, for example. The beam energy jitter coming from the linac is expected to be up to 0.1% of the nominal energy [63]. The strength of the magnet that a particle sees depends on the energy of the particle: more energetic particles will bend less than less energetic particles. Therefore, the performance of the systems designed for the nominal energy might be seriously affected if variations in energy are important enough. The energy acceptance, or energy bandwidth, is the range of energies that a system like the FFS is able to accept before decreasing its performance drastically. Ideally, we want the FFS to have the largest energy acceptance. Realistically, this acceptance is very limited. In this section we compare the energy acceptance of the different designs at different energies. The beam energy is varied from $E = E_0(1-0.01)$ to $E = E_0(1+0.01)$. In the case $E_0 = 1500$ GeV it corresponds to $E \in [1485, 1515]$ GeV and for $E_0 = 250$ GeV to $E \in [247.5, 252.5]$ GeV.

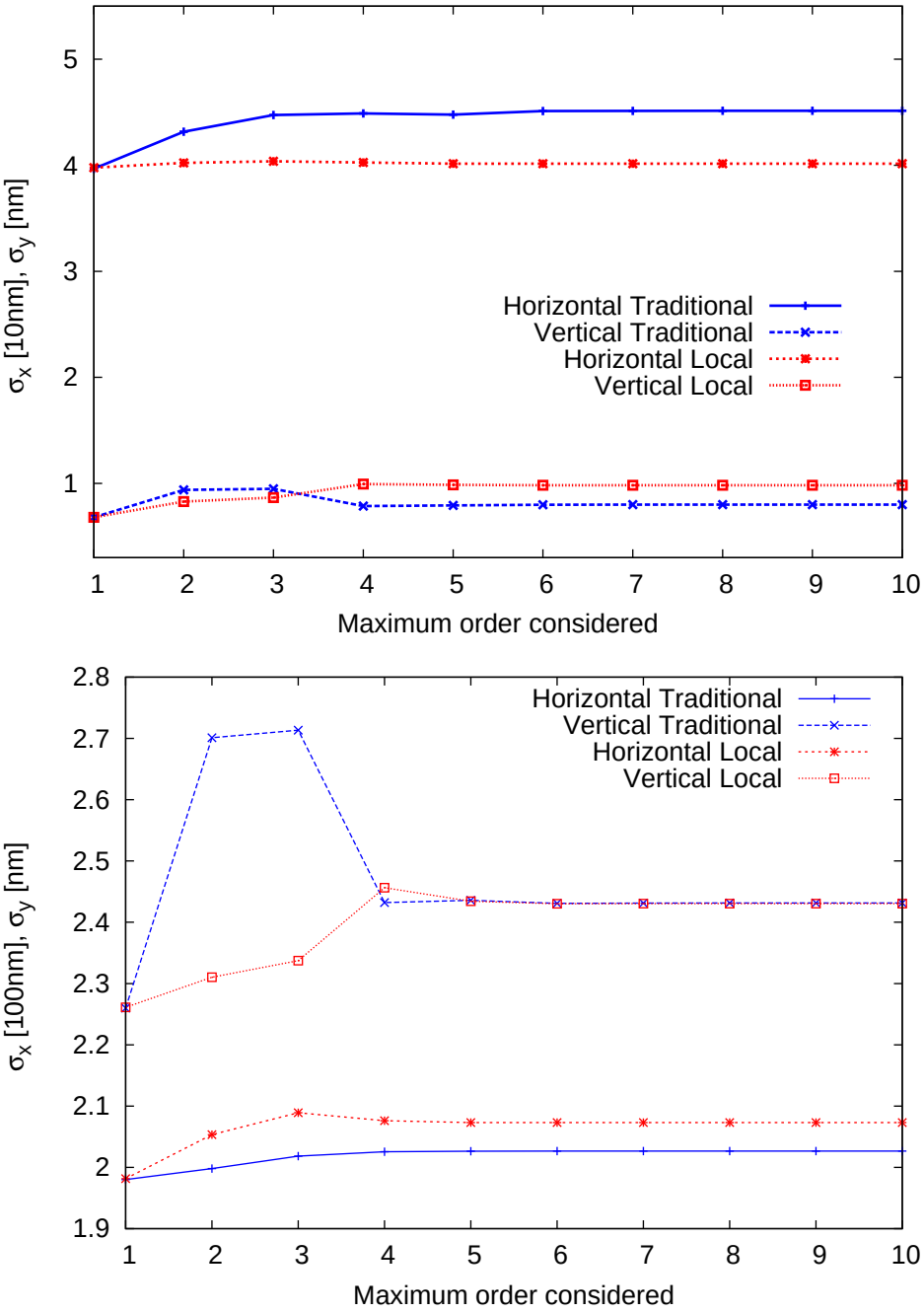

Figure 3.9: High order optimization using MAPCLASS for CLIC FFS at 3 TeV (top) and 500 GeV (bottom).

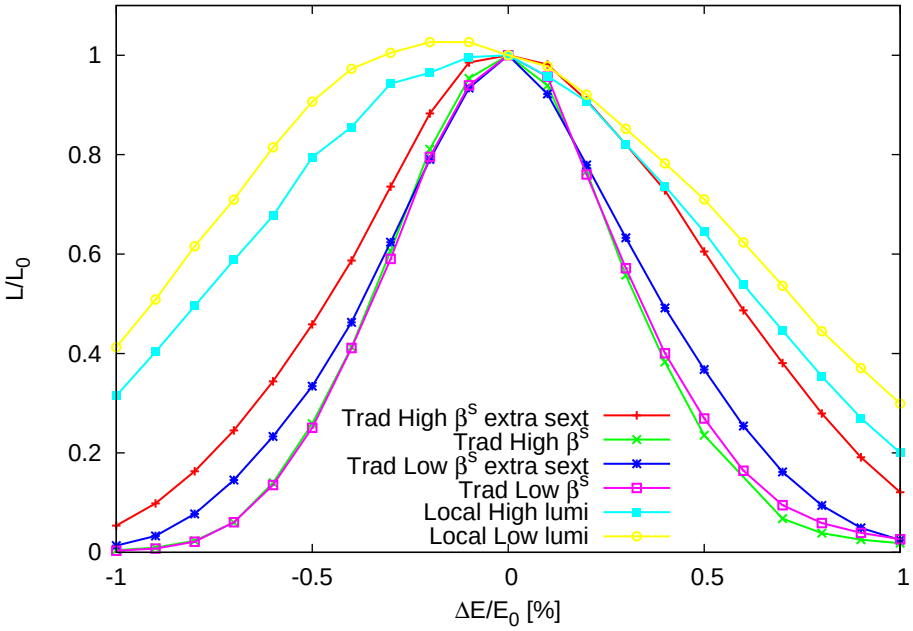

Figure 3.10: Energy bandwidth for CLIC FFS at 3 TeV. Two different lattices are considered for the local scheme called High and Low luminosity respectively. The first presents a higher total luminosity but a more reduced bandwidth while the latter has been optimized to increase energy bandwidth paying the cost in terms of luminosity reduction. In all the cases, the beam contains always some energy spread using a flat distributed beam with $0.01E_0$ width.

3 TeV

In Fig. 3.10 the luminosity delivered by the FFS is shown as a function of the beam energy for different systems. The local chromatic correction scheme presents a better energy acceptance while the different cases of the traditional present a narrower curve. For the traditional case we compare the pure dedicated correction system with the extended version including more sextupoles following the idea of Brinkmann explained in previous chapter. Indeed, the extra sextupoles increase the momentum acceptance of the system in a non negligible way.

500 GeV

As in the previous case, in Fig. 3.11 we see how the luminosity decreases rapidly when the beam has a difference in the energy with respect to the nominal value. Due to the fact that sextupoles are placed close to the FD and the odd dispersion scheme, the local correction scheme presents a wider energy bandwidth than the traditional scheme. In any case, the results are similar to the ones shown for the high energy case.

3.3.2 Increasing the energy bandwidth

The weak point of the traditional scheme, even with the extra sextupoles following Brinkmann's idea, is the reduced energy bandwidth compared to the local system. An idea to increase the energy acceptance of the traditional scheme [74] is to place a sextupole in the minimum of the β-functions before the FD. At this location, the vertical β-function is seriously affected for off momentum particles and therefore a beam size dilution at the IP. The last bending magnet is displaced towards the IP in order to keep some residual dispersion at the sextupole location. The sextupole strength must be optimized to adapt

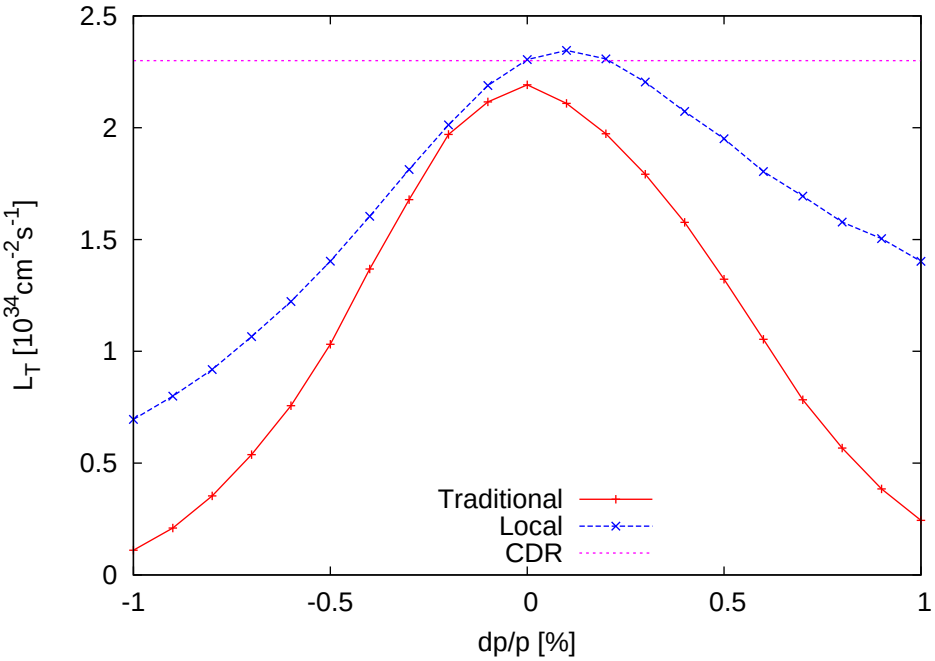

Figure 3.11: Energy bandwidth for CLIC FFS at 500 GeV. The beam energy profile is a flat distribution of $0.01E_0$ width.

the optics for off momentum particles. In case that an even more increased bandwidth is needed, it is possible to improve it by placing a sextupole in the betatron waist position upstream of the FD and move last dipoles in order to let some dispersion at the sextupole location following the idea exposed in [74].

Jitter in energy coming from the linac

The expected energy jitter of the beam coming from the linac and arriving to the FFS is about $\Delta E/E \approx 0.1\%$. According to the results shown previously, a deviation of 0.1% from nominal energy yields a luminosity decrease of about 4% in the local scheme and of about 8% in the traditional scheme at 3 TeV. A detail of the energy bandwidth at 3 TeV is shown in Figure 3.12.

3.4 Beam halo

A major issue facing the functioning of a high current accelerator is beam halo formation. The halo is formed by a small intensity distribution of particles surrounding the core of the beam and they can cause unacceptable amounts of backgrounds in the detector as well as damage in the different elements of the beamline in case this halo escapes from the beam aperture. In order to reduce the number of particles lost and to design the collimation system, a precise control of the beam halo is mandatory. In order to observe the effect of the FFS on the beam halo we track an elliptical transverse distribution of particles with dimensions of the collimation aperture, i.e. $15\sigma_x$ horizontally and $50\sigma_y$ vertically, with a flat distributed energy spread of 1.4%. Figure 3.13 shows the halo distributions at the entrance of the FD for traditional and local FFS at CLIC 3 TeV. Unlike in [25] we observe that the optimized traditional chromatic correction scheme presents a more compact halo distribution compared to the local system.

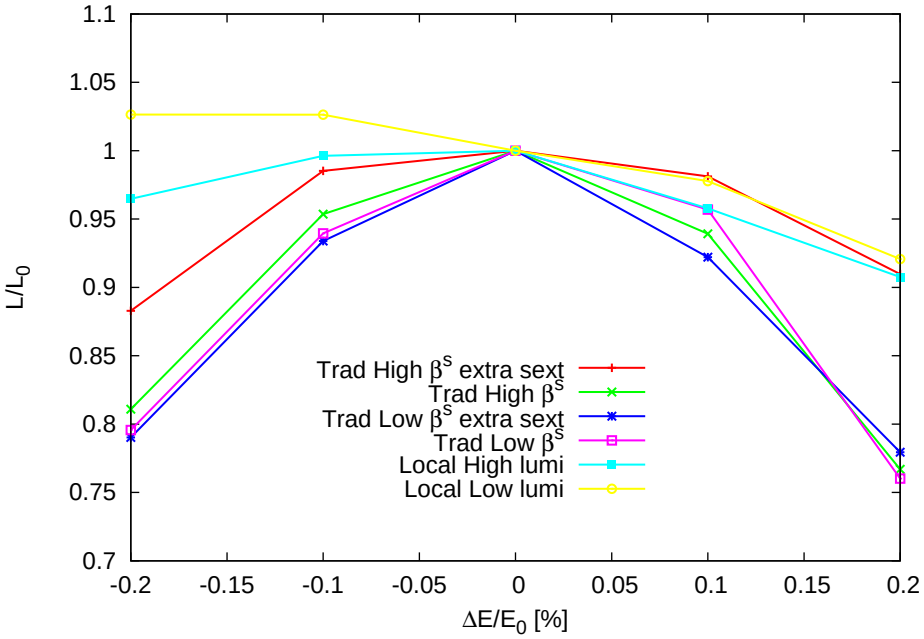

Figure 3.12: Detail of the energy bandwidth for CLIC FFS at 3 TeV.

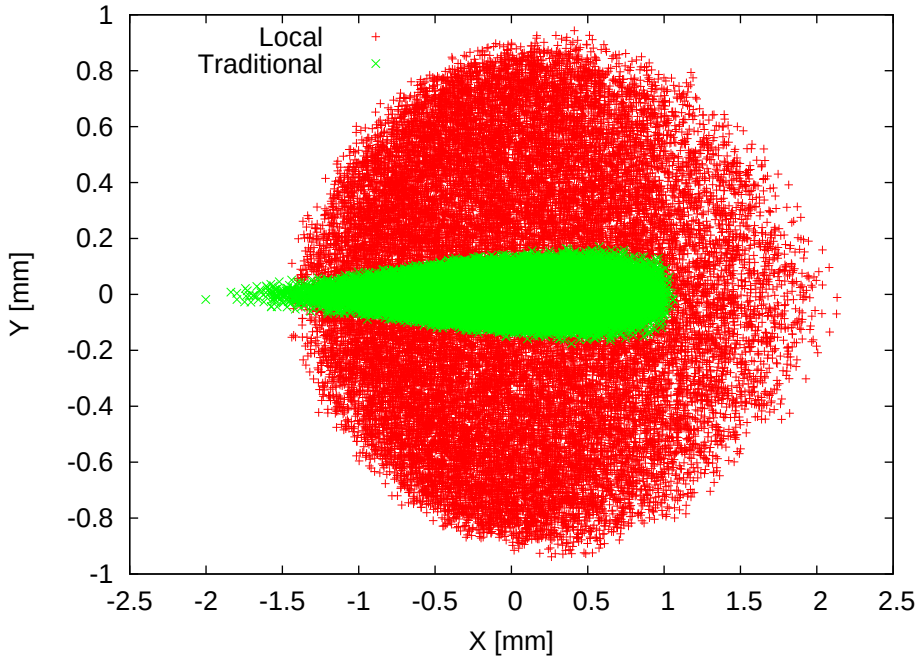

Figure 3.13: Beam at the entrance of the final doublet for the local and the traditional FFS for CLIC at 3 TeV c.o.m. energy. Particles of the incoming beam are placed on an ellipsoid of $15\sigma_x$ and $50\sigma_y$ and an flat energy distribution with $1.4\%E_0$ width.

Table 3.7: Example of optimized weights for 3 TeV lattices.

Scheme	Energy [GeV]	β	ω_1	ω_2
Local	3000	10	635	11
Traditional	3000	17	197	463

3.5 Tuning

The tuning procedure and the different techniques to recover nominal performance of the machine when realistic imperfections are introduced has been explained in chapter 2. In this section we describe the results obtained from tuning simulations for different designs of the CLIC FFS described above. The tuning simulations follow the same techniques applied in earlier designs of the CLIC and ILC FFS [26,64,65].

In simulations we assume that all the magnets of the FFS (except for the bending magnets) are randomly displaced in the two transverse planes with a Gaussian distribution of $\sigma = 10\,\mu$m, which is defined to be the prealignment tolerance for this study. This value is an estimate [67], which is very close to the value used in the main linac and in previous FFS tuning simulations [65]. In this study the electron and positron lines are identical. The techniques used to recover from the magnets displacements are: beam based alignment (BBA) combined with sextupole knobs. The BBA technique consists of the orbit correction followed by dispersion-free steering (DFS) in the vertical plane and target dispersion in the horizontal one like in [69]. In the orbit correction,the beam is steered through the center of the beam position monitors (BPMs). DFS is a technique that measures the dispersion along the line, using off-energy test beams, and corrects it to zero or the nominal value. An energy difference of $\pm 0.1\%$ is used to measure dispersion. The assumed BPM resolution in these simulations is 10 nm.

The possibility to use tuning knobs based on sextupole displacements has been already explored in CLIC [65], ILC [64] and ATF2 [26]. The knob creation procedure followed for this study is detailed in [65]. The algorithm applies sequentially a one-to-one correction, dispersion free steering, tuning knobs, a second dispersion free steering and a final tuning knobs pass. We have added three weights $(\beta, \omega_1, \omega_2)$ that avoid too large corrector kicks to be applied from singularities during the Singular Value Decomposition (SVD). They are introduced in the DFS algorithm in the following way,

$$\begin{pmatrix} \vec{b}_n \\ \vec{\eta} - \vec{\eta}_0 \\ 0 \end{pmatrix} + \begin{pmatrix} R_c \\ \omega D \\ \beta \mathcal{I} \end{pmatrix} \cdot \vec{C}_M = 0, \tag{3.3}$$

where we use $\omega = \omega_1$ for the first DFS and $\omega = \omega_2$ for the second one and $\mathcal{I}$ is the identity matrix. These three weights are optimized following a Simplex minimization taking the final beam size as the figure of merit. Table 3.7 summarizes the optimal values found in each case.

We have observed that after second DFS, luminosity decreases but the final luminosity is always higher than if we do not apply this step. This is due to the fact that DFS does not have luminosity as a figure of merit but the orbit flatness and the zero dispersion. This second dispersion correction is needed since sextupole positions have changed after the first iteration of tuning knobs and dispersion requires to be rematched at the sextupole locations. In Fig. 3.14 the evolution of luminosity after each step for different seeds is shown for the optimized Traditional scheme at 3 TeV. One can observe that the big luminosity gain is achieved when knobs are applied.

The final total luminosity obtained after the application of BBA and tuning knobs for the 100 machines are shown in Fig. 3.15 and Fig. 3.17 for 3 TeV and 500 GeV c.o.m. energy respectively.

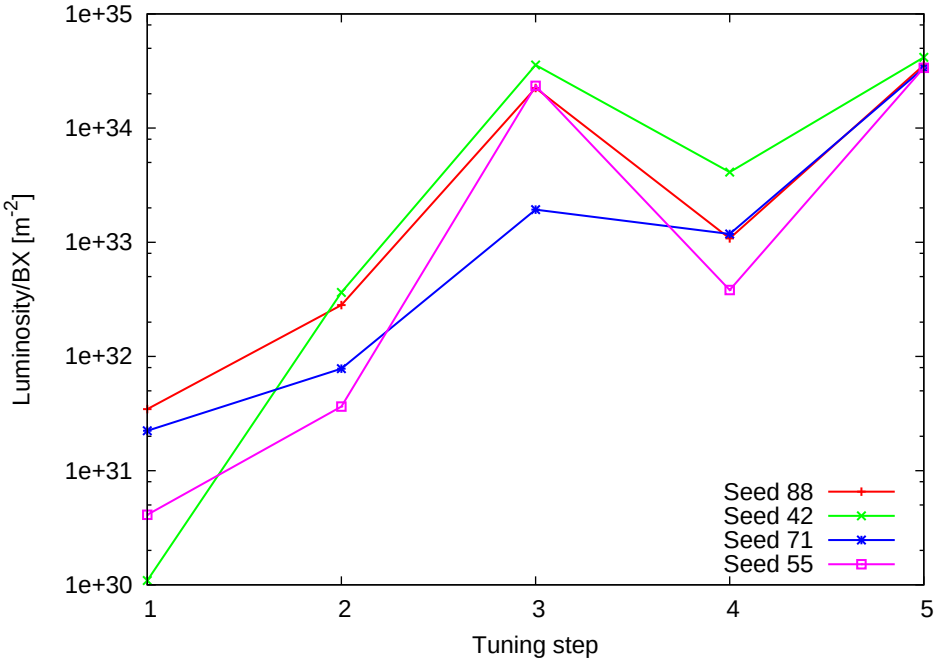

Figure 3.14: Luminosity evolution at each step of the algorithm during tuning simulation for the traditional scheme at 3 TeV. In the horizontal axis 1=One-to-one, 2=DFS, 3=Knobs, 4=DFS, 5=Knobs.

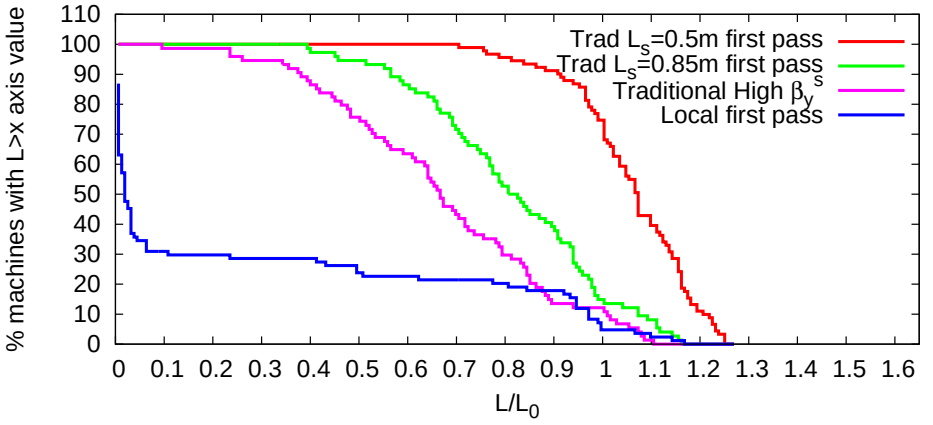

Figure 3.15: Luminosity distribution of 100 machines after BBA and Multiknob algorithm procedure for an initial prealignment of 10 μm for CLIC 3 TeV. Luminosity is normalized to the value given in Table 3.1.

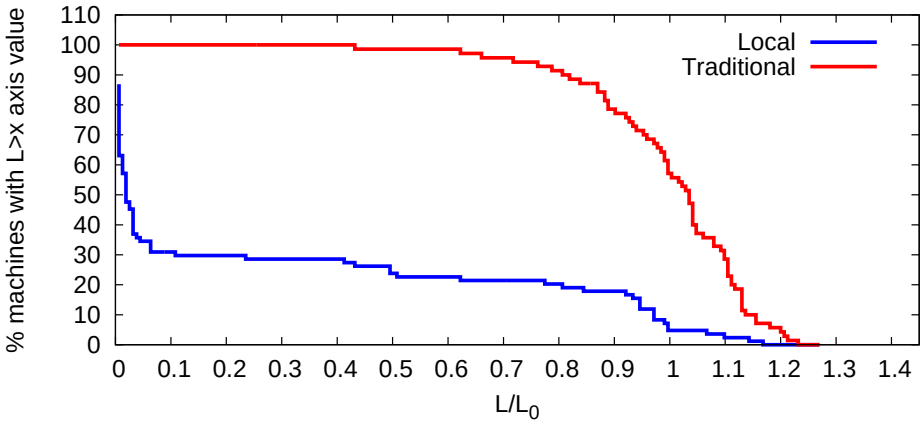

Figure 3.16: Luminosity distribution of 100 machines after BBA and Multiknob algorithm procedure for an initial prealignment of 10 μm for CLIC 3 TeV for the lattice with intermediate β_y-functions at the sextupoles and sextupoles of 70 cm. Luminosity is normalized to the value given in Table 3.1.

3.5.1 3 TeV results

Figure 3.15 shows the results of the tuning simulations after one iteration of the algorithm. In the vertical axis is the number of machines that reach at least the luminosity shown in the horizontal axis, which is normalized to the nominal value of the luminosity given in Table 3.1. We notice that the tuneability of the local scheme is very challenging. Almost 70% of the machines do not reach 10% of the nominal luminosity. However, the traditional scheme presents a much better tuneability, showing that 90% of the machines reach at least 90% of the nominal luminosity.

The number of luminosity measurements per iteration of the algorithm is about 300, that corresponds to a time span of about 5 minutes if a fast luminosity measurement takes 1 second [65]. Since the tuneability of the local scheme is not satisfactory more iterations of the algorithm and a Simplex optimization are required. This additional tuning steps increase the number of luminosity measurements by an order of magnitude [65], and therefore more time devoted to tuning not usable for physics. In [65] the full tuning simulation of the local scheme was done using a higher bunch charge, $4.0 \cdot 10^9$ particles per bunch instead of the nominal charge of $3.72 \cdot 10^9$ [66], where 90% of the machines reach at least 90% of the nominal luminosity. At the nominal charge, this performance might not be reachable even with further tuning. Due to dynamic imperfections luminosity drops by 10% after 30 minutes [68] and then a new tuning is required to recover the full luminosity. Therefore, a tuning time much shorter than the time at which the dynamic effects become important is crucial to ensure the optimal tuning performance and more time devoted to physics.

3.5.2 500 GeV results

For the 500 GeV case, the results for both schemes are shown in Fig. 3.17 for just one iteration of the algorithm in both cases. We see how the result is quite similar for both systems reaching the goal of 90% of the machines above the 90% of the nominal luminosity. Again, the local correction scheme delivers more total luminosity but the traditional scheme presents a slightly easier tuneability. In that case, differences between both schemes are smaller than at 3 TeV and the time to reach a reasonable luminosity is comparable. The tunning time is expected to be also around 20-30 minutes in both cases.

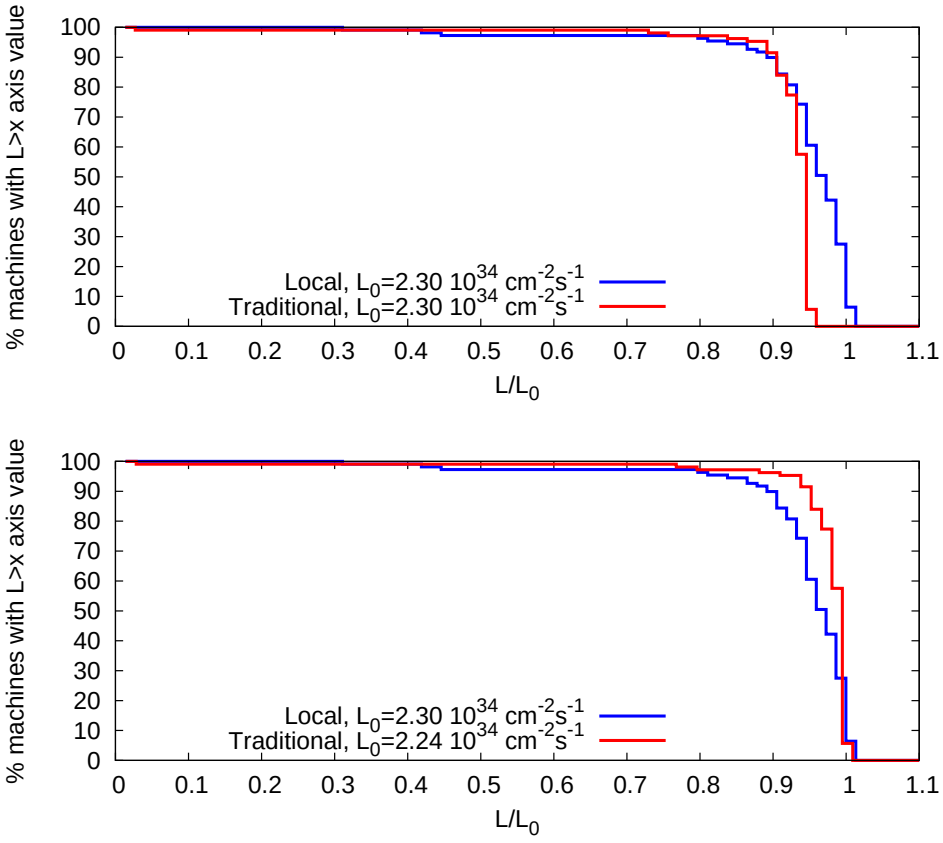

Figure 3.17: Luminosity distribution of 100 machines after BBA and Multiknob algorithm procedure for an initial prealignment of 10 μm for CLIC at 500 GeV). Luminosity is normalized to the nominal value present in Table 3.1 (top and to the maximum value obtained by each system (bottom).

3.6 Conclusions

We have compared the performance and tuning simulation of two different FFS schemes for CLIC at 3 TeV and 500 GeV center of mass energy. The study concludes that the traditional system is about 1 kilometer longer than the local system but only at high energies. At low energies both systems require a similar length. The compensation of nonlinearities by both systems yields a comparable luminosity. Also the difference in the energy bandwidth is relatively small in the range of interest. The main difference comes from the tuning simulation, where we have demonstrated that the Traditional FFS is much easier to tune at high energies, just one iteration of the proposed algorithm is needed to achieve the goal of 90% of the machines above 90% of the nominal luminosity while the local scheme would require more iterations and, in consequence a tuning time that exceeds rapidly one hour without guaranteeing that 90% of the machines are above 90% of the nominal luminosity. A faster tuneability translates into a larger integrated luminosity. Therefore, at high energies, the optimized traditional FFS features a higher performance and robustness than the local scheme that must be weighted against the cost of a longer tunnel.

Chapter 4

CLIC $\sqrt{s} = 500$ GeV β_x^* reduction

The determination of the IP horizontal β-function is mainly driven by the beamstrahlung emission during the collision of the electron and positron beams. This effect might yield to serious implications in the quality of the luminosity spectrum and its impact on the precision of the measurements. In this chapter we explore the possibility to reduce the horizontal β-function to half of the nominal value.

4.1 Motivation

There are several reasons to explore lower horizontal β-functions. The straightforward reason is of course to increase the luminosity value. Since luminosity $\mathcal{L}$ scales with $(\sqrt{\beta_x^*})^{-1}$, a reduction of a factor 2 in β_x^* implies a factor $\sqrt{2}$ more luminosity. Secondly, one could think of keeping the ratio N/σ_x^* constant, keeping also luminosity constant but reducing the number of particles per bunch and partly restoring the detrimental effects of beamstrahlung.

4.2 Ideal distributions

First of all we consider ideal distributions at the IP. By ideal distributions we mean distributions generated at the IP with the parameters present in Table 4.1 without tracking through the FFS. It means that the beam distributions do not suffer from beam dilution due to nonlinear aberrations or synchrotron radiation effects. In Fig. 4.1 the total luminosity for ideal distributions for three different values of β_x^* is shown as a function of the vertical beta function β_y^*. We observe that luminosity is higher for lower β_x^*. Also the reduction of β_y^* implies an increase of the luminosity until a certain value is reached, then luminosity starts to decrease. This reduction is due to the hourglass effect when the vertical beta function is comparable to the longitudinal beam size. Therefore the optimal value for β_y^* is close to 0.065 mm. This value is taken for the rest of the study.

4.3 Lattice optimization

The lattice optimization is performed using the techniques explained in previous chapters. Simulations using ideal distributions give an overall idea of how the system will perform. The vertical β-function at the IP is set to the optimal value found using ideal distributions, i.e. $\beta_y^* \approx 0.065$ mm. This change in β_y^* will not affect considerably the value of the luminosity as will be seen in the next section. The horizontal β-function is chosen to have three different values: 8, 6 and 4 mm.

The beam is affected by the strong focusing by the FD and chromatic effects must be taken into account. The chromatic compensation is carried out by means of sextupoles. In all cases we use five sextupoles for chromaticity correction. In Fig. 4.2 the beam size is sequentially optimized order by order until higher order contributions are negligible. One can see that beyond order 6 the beam size does

Table 4.1: CLIC Design parameters at two different stages of the program, 500 GeV and 3 TeV center of mass energy [12]. The energy spread σ_δ represents the full width of a flat distribution.

Parameter [Units]	500 GeV
Center of mass energy E_{CM}, [GeV]	500
Repetition rate f_{rep}, [Hz]	50
Bunch population N_e [10^9]	6.8
Number of bunches n_b	354
Bunch separation Δt_b, [ns]	0.5
Accelerating gradient G, [MV/m]	80
Bunch length σ_z, [μm]	72
IP beam size σ_x^*/σ_y^*, [nm]	200/2.26
Beta function (IP) β_x^*/β_y^*, [mm]	8/0.1
Norm. emittance (IP) ϵ_x/ϵ_y, [nm]	2400/25
Energy spread σ_δ, [%]	1.0
Luminosity $\mathcal{L}_{\mathrm{T}}$ [$10^{34}\mathrm{cm}^{-2}s^{-1}$]	2.3
Power consumption P_{wall}, [MW]	272
Site length, [km]	13.0

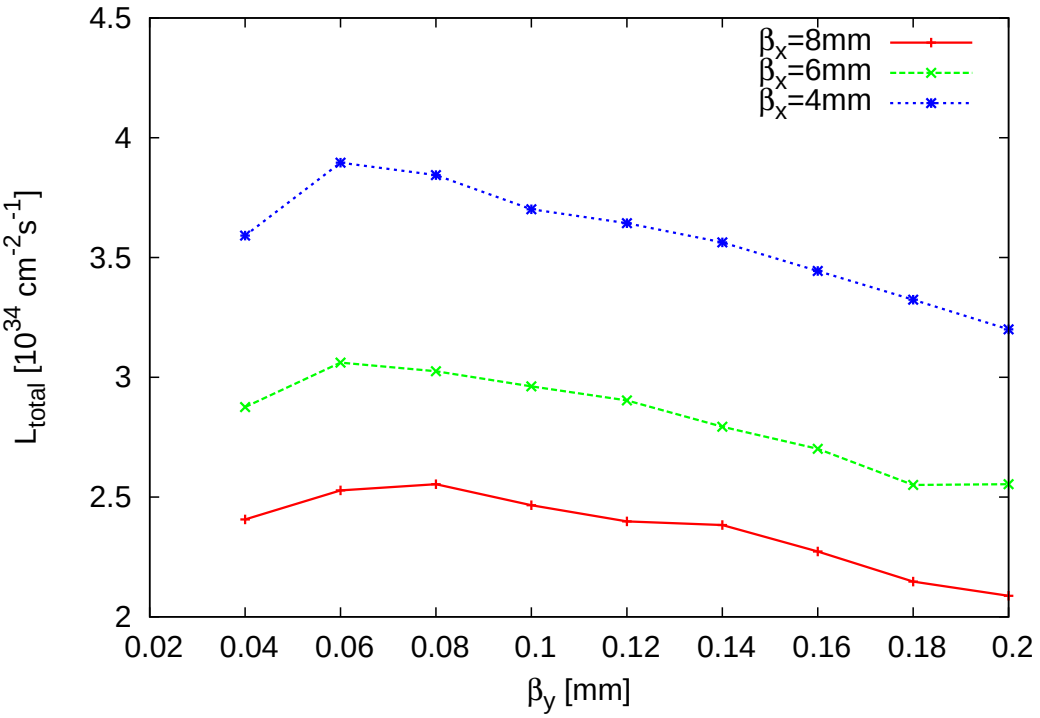

Figure 4.1: Total luminosity for different values of β_x^* asuming ideal distributions at the IP.

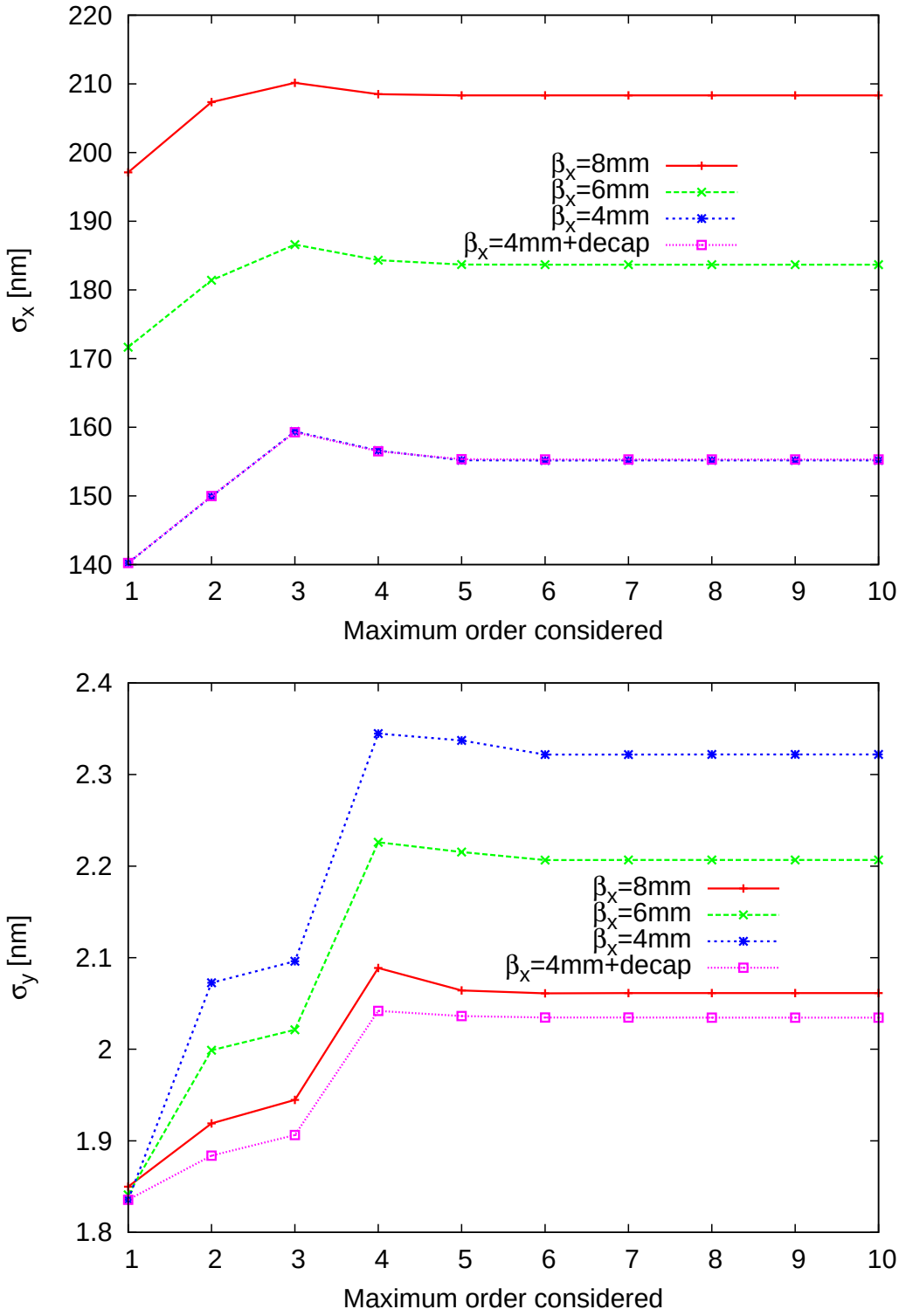

Figure 4.2: High order optimization using MAPCLASS for CLIC FFS for horizontal plane (top) and vertical plane (bottom).

Table 4.2: Beam size for different configurations at the IP taking into account synchrotron radiation effects.

β_x^* [mm]	σ_x^* [nm]	σ_y^* [nm]
8	210.1	2.51
8	213.3	2.20
6	189.2	2.36
4	163.6	2.84
4+decap	162.8	2.56
4+decap+high disp.	166.6	2.31

Table 4.3: Luminosity and emitted photons per particle during collision for different configurations at the IP. The first row represents the results of the nominal case considering CDR values.

β_x^* [mm]	$\mathcal{L}_T$ [10^{34}cm^{-2}s^{-1}]	$\mathcal{L}_{1\%}$ [10^{34}cm^{-2}s^{-1}]	$\mathcal{L}_{1\%}/\mathcal{L}_T$	n_γ
8*	2.31	1.40	0.61	1.32
8	2.34	1.45	0.62	1.30
6	2.70	1.56	0.58	1.47
4	3.12	1.61	0.52	1.74
4+decap	3.20	1.65	0.52	1.74
4+decap+h.disp.	3.28	1.71	0.52	1.71

not change substantially. Although the beam size decreases due to the change in the β-function, the nonlinear aberrations do not present more impact for smaller values of β_x^*. Nevertheless, the reduction of the horizontal β-function has an important impact on the vertical plane, where one can see that the beam size dilution becomes important for $\beta_x = 4$ mm. The impact of nonlinearities in the later case represents a 25% beam size increase. For that reason and regarding that the map term that mainly contributed to the beam size dilution was a decapolar term, we decided to add two decapole magnets in the FD area to correct this aberration. Also the bending angle was increased in order to better compensate the aberrations although increasing the synchrotron radiation effects. The result after reoptimization is also shown in Fig. 4.2 and one can see the big improvement that the decapoles and higher dispersion represent reducing the total impact of the aberrations to less than 10%. In Table 4.2 the RMS beam sizes are summarized taking into account synchrotron radiation effects in bending magnets and quadrupole magnets (Oide effect). It can be observed that the dispersion increase is translated in a horizontal beam size dilution because of synchrotron radiation but the vertical beam size reduction is larger and this will imply a luminosity increase as we explain in next section and it is reflected in Table 4.3.

In Table 4.3 the total luminosity and peak luminosity (luminosity delivered by particles with energies $\geq 99\%$) values are shown. Also the ratio between luminosities has been calculated and it gives an idea of the quality of the luminosity spectrum. As we will see in the next sections, smaller horizontal beam sizes yield to higher beamstrahlung emission and therefore a poorer luminosity spectrum.

First of all, a clear gain in luminosity is seen when β_x^* is reduced. If we compare the initial value for luminosity given by the CDR configuration with the best luminosity value when we consider $\beta_x^* = 4$ mm, higher dispersions and the decapoles, it represents a gain above 40% in total luminosity and a 22% gain in peak luminosity. Also it is clear that the reduction of β_y^* from its original value to 0.065 mm does not represent a big gain.

The luminosity spectrum is shown in Fig. 4.3. The peak luminosity (bin centered at 500 GeV) is lower for β_x^* as was shown in Table 4.3. The rest of the luminosity is spread in the long tail representing luminosity of particles with lower energies.

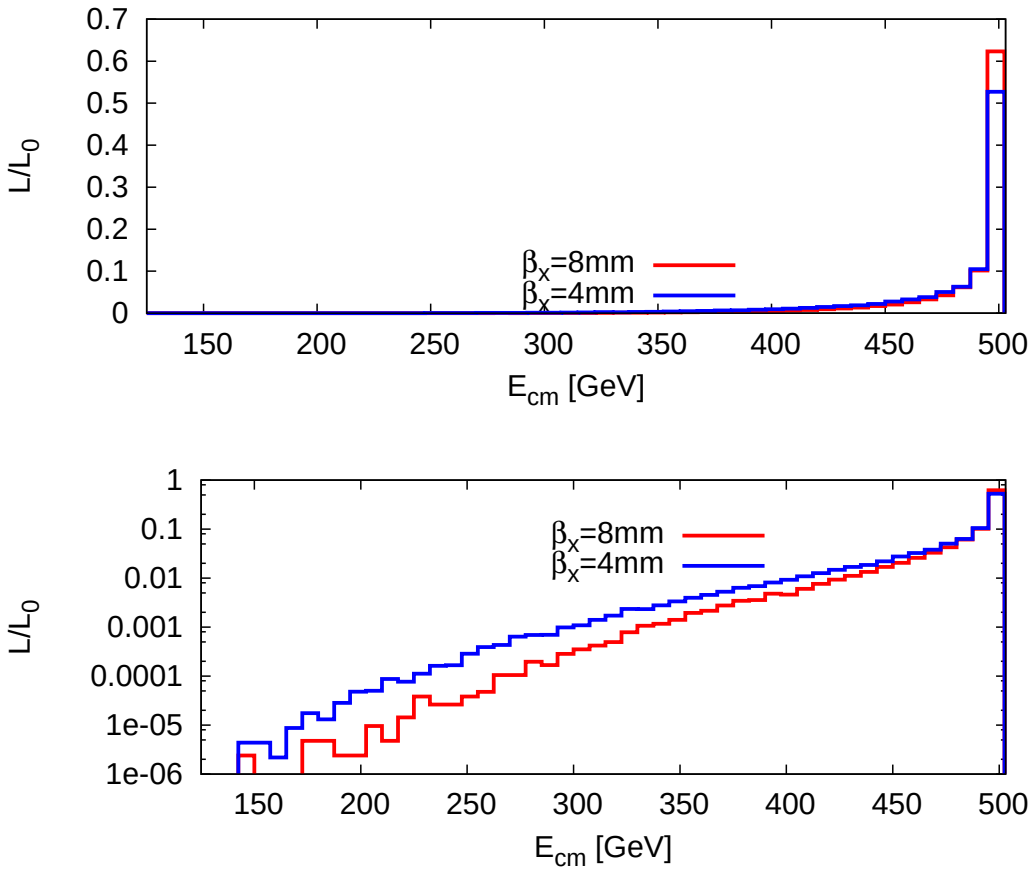

Figure 4.3: Luminosity spectrum for $\beta_x^* = 8$ mm and $\beta_x^* = 4$ mm with high dispersion and decapoles. Normal scale (top) and logarithmic scale (bottom).

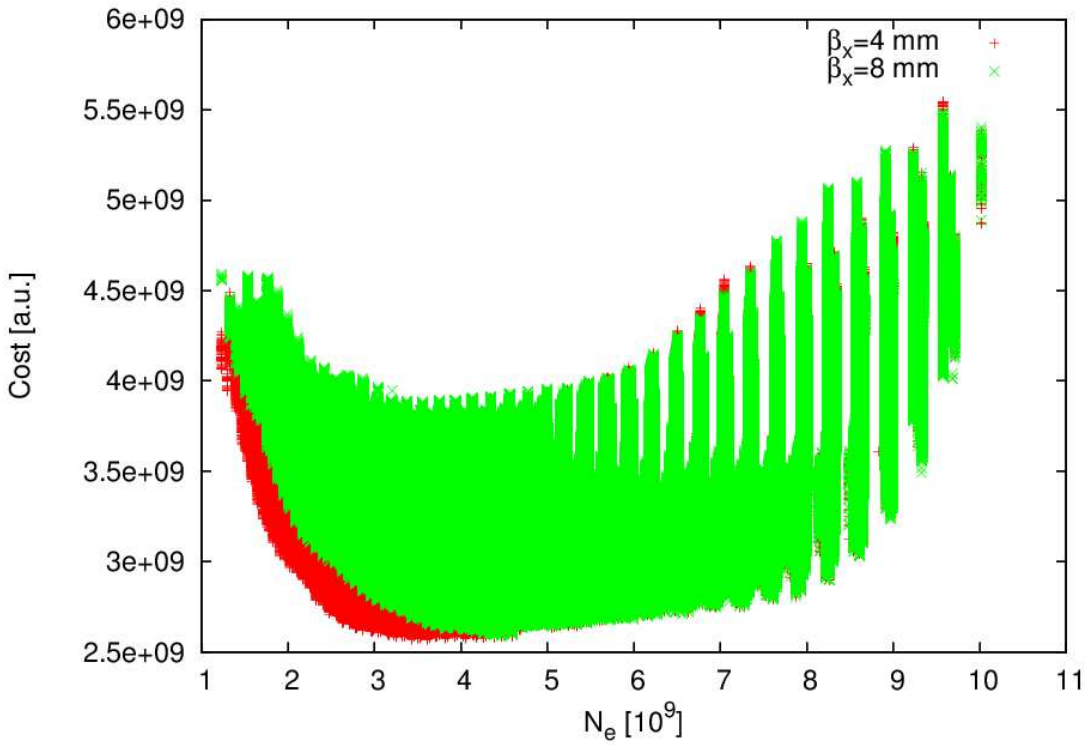

Figure 4.4: Cost after optimization as a function of the bunch charge for two different β_x^* functions. The observed beating represent the steps chosen in the horizontal axis.

4.4 Cost optimization

Apart from an increase in luminosity, the reduction of β_x^* can be used as an option to reduce the bunch charge while keeping the same luminosity value. We can rewrite Eq. (2.42) into

$$\mathcal{L} = \frac{1}{4\pi}\frac{N}{\sigma_x^*}\frac{P_{\text{beam}}}{\sigma_y}H_D \tag{4.1}$$

where P_{beam} is the beam power given by the product $P_{\text{beam}} = Nf_{\text{rep}}n_b$. It can be seen that, since $\sigma_x^* = \sqrt{\beta_x^*\epsilon_x}$, a reduction of a factor 2 in β_x^* could correspond to a reduction of a factor $\sqrt{2}$ in bunch charge while keeping approximately the same luminosity. Although total luminosity stays constant, the luminosity spectrum gets worse since the beam size is less flat and the photon emission increases as it has been explained in previous sections.

The cost optimization is an automatic procedure scanning over many structures, or different parameter sets like the length of the accelerating cells or their gradient among others. The results is the cost of each configuration and its relationship with some other parameters such as total and peak luminosity. For example, more expensive configurations might yield into a higher performance in terms of luminosity. In Fig. 4.4 the cost estimation in arbitrary units of the whole accelerator as a function of the bunch charge is shown for two different values of β_x^*: 8 and 4 mm. We can see that only a few configurations at low bunch charges are cheaper for the case at $\beta_x^* = 4$ mm with respect to $\beta_x^* = 8$ mm. In any case, there is a save in power consumption due to the lower charge which is not considered in the optimization.

4.5 Energy scaling

Another application of the β_x^* reduction is when we consider a scaling down of the energy. Since, due to linac considerations, the number of particles per bunch scales linearly with the beam energy, when we reduce energy we are forced to reduce the number of particles. Although this will imply also a luminosity reduction, this effect can be partially mitigated if we can reduce β_x^* for lower energies.

4.6 Conclusions

We have designed a lattice with a factor 2 reduction in β_x^* at the IP. Although this cannot redefine the design parameters, it shows that the design has some flexibility. We have explored the possibility to use this new lattice to increase luminosity and also to consider a bunch charge reduction although it does not yield a clear cost reduction.

Chapter 5

ILC Final Focus System Optimization

The beam delivery system constitutes several of the foremost challenges to be faced in any linear collider. This is a direct consequence of the extremely small beam size required for a single pass collider to attain a luminosity competitive with that of a storage ring running at the same energy where the high repetition rate presents the most important difference.

The ILC Final Focus System shares a lot of similitudes with the CLIC FFS. Both are based on the local chromaticity correction scheme [25]. In this chapter a reoptimization of the ILC β-functions at the IP is carried out for an energy of 500 GeV c.o.m. Taking into account the similarities of both colliders, we explore the possibility of using the CLIC FFS for ILC and its performance compared to the original one. We also recover the classical topic of the traveling focus scheme applied to ILC using different FFS configurations.

5.1 ILC Final Focus System

The role of the ILC Final Focus System [15] is to demagnify the beam to the required size (474 nm horizontal and 5.9 nm vertical) at the IP. The FFS optics creates a large and almost parallel beam at the entrance of the final doublet of strong quadrupoles. Since particles of different energies have different focal points, even with a relatively small energy spread of $\sim 0.1\%$ the beam size is diluted significantly, unless adequate corrections are applied. The design of the ILC FFS is mainly driven by the need to cancel the chromaticity introduced by the FD.

The ILC FFS is based on the local chromaticity correction using sextupoles interleaved with the FD [25]. A bend upstream generates dispersion accross the FD region required for the sextupoles to cancel chromaticity. The dispersion at the IP is zero and the angular dispersion is about $\eta'_x \sim 0.009$. Half of the horizontal chromaticity of the whole system is generated upstream of the bending section in order for the sextupoles to cancel the chromaticity and the second-order dispersion. The horizontal and vertical sextupoles are interleaved in this design, so they generate third-order geometric aberrations. Additional sextupoles upstream and in proper phases with the FD sextupoles partially cancel the third order aberrations. The residual higher-order aberrations are minimized further with octupoles and decapoles. A general layout of the 735 m long ILC FFS lattice and optical functions is shown in Fig. 5.1. The main difference of the ILC FFS design with respect to the CLIC FFS design is the presence of dedicated octupoles for the nonlinear handling of the beam tails in ILC. Hence, octupole doublets are present in the design to achieve this purpose. They would be located in the first high β-function peak from the left in Fig.5.1. The beam at that location must be parallel or divergent.

Synchrotron radiation from the bending magnets causes emittance dilution, so it is important to maximize the bending radius, especially at higher energies. The ILC FFS includes sufficient bending

Table 5.1: Key parameters of the ILC Beam Delivery System.

Parameter	Value	Unit
Length per side	2254	m
Length of the main extraction line	300	m
Max. Energy/beam	250	GeV
Distance from the IP to the first quad, L^*	3.51/4.5	m
Crossing angle	14	mrad
Normalized emittance, $\gamma\epsilon_x/\gamma\epsilon_y$	10000/35	nm
Nominal beam size, σ_x^*/σ_y^*	474/5.9	nm
Nominal beam divergence, η_x'/η_y'	43/12	μrad
Nominal beta-function, β_x^*/β_y^*	11/0.48	mm
Nominal bunch length, σ_z	300	μm
Energy spread $\delta p/p$, e^-/e^+	0.125/0.070	%
Nominal disrubption parameters, D_x/D_y	0.3/24.6	
Nominal bunch population, N	$2.0 \cdot 10^{10}$	
Repetition rate, f_{rate}	5.0	Hz
Number of bunches, n_b	1312	
Average beam power per beam	5.3	MW
Preferred entrance train to train jitter	< 0.5	σ_y
Preferred entrance bunch to bunch jitter	< 0.1	σ_y
Typical nomnal collimation aperture, x/y	8-10/60	
Final Focus System Lenght	735	m

magnets for 500 GeV center of mass energy and space for additional bend magnets which are necessary at energies above 500 GeV. With the reserved space filled with bends, the emittance dilution due to bends at 1 TeV is about a percent, and at 500 GeV, with only every fifth bend installed, about half of a percent [15].

5.2 β^* optimization

The optimization of the β-functions at the IP is a very critical step of the design of an accelerator. The β-functions determine in great part the beam size at the IP and the final value of luminosity. A reoptimization of $\beta_{x,y}^*$ was proposed for the Technical Design Report (TDR) [15] from the old values of the Reference Design Report (RDR) [14]. We modified the nominal values from $\beta_x^* = 20$ mm to $\beta_x^* = 11$ mm and from $\beta_y^* = 0.4$ mm to $\beta_y^* = 0.48$ mm. The optics optimization is done using MADX and the new β functions at the IP are achieved by mainly adjusting the four matching quadrupoles located at the beginning of the Final Focus System. Apart from the β functions, the α functions and the horizontal dispersion D_x^* are matched to be zero at the IP. In Table 5.3 the final values for these functions after linear optimization are summarized.

Since the β functions at IP and at the sextupole locations have been changed, the sextupole strengths must be rematched again in order to correct the nonlinear aberrations mainly coming from the quadrupole chromaticity. In the next section the nonlinear optimization of the sextupole strength is performed using the beam size at different orders as a figure of merit.

5.2.1 Nonlinear optimization

The nonlinear optimization of the beam size consists in the compensation of the chromaticity introduced by the strong final quadrupoles and correction of other aberrations due to the presence of nonlinear fields. The ILC optimization is carried out using MAPCLASS [48] to compute the beam size at different orders and five sextupoles are used (SD0, SF1, SD4, SF5, SF6) to reduce the beam size as much as possible.

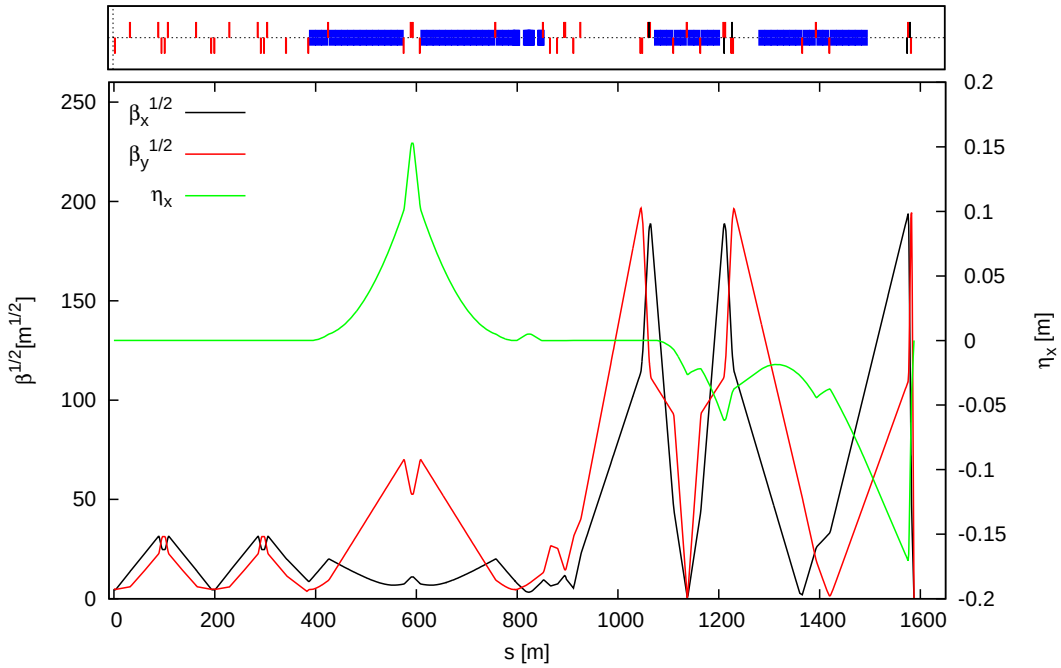

Figure 5.1: ILC BDS optics layout. The first 800 meters are dedicated to collimation section and the part from that point to the end represents the Final Focus System.

Table 5.2: CLIC and ILC Beam Delivery System parameters.

Parameter	**Units**	CLIC500	ILC500
Beam energy E_0	GeV	250	250
Bunches per beam n_b		354	1314
$e^{\pm}$ per bunch N	10^9	6.8	20
Repetition rate f_{rep}	Hz	50	5
Hor. emittance ϵ_x^N	μm	2.4	10.0
Vert. emittance ϵ_y^N	nm	25	35
Hor. beta β_x^*	mm	8.0	11.0
Vert. beta β_y^*	mm	0.1	0.48
Hor. beam size σ_x^*	nm	200	474
Vert. beam size σ_y^*	nm	2.26	6.0
Bunch length σ_z	μm	72	300
Energy spread δ_E	%	1.0	0.125
Main tunnel length	km	48.3	13.2
Luminosity $\mathcal{L}_T$	$10^{34} \cdot \text{cm}^{-2}\text{s}^{-1}$	2.3	1.47

Table 5.3: ILC optical functions at the IP for the two optics configurations $L^* = 3.51$ m and $L^* = 4.5$ m

L^* [m]	3.51	4.5
β_x^* [mm]	11.00	11.00
β_y^* [mm]	0.48	0.48
α_x^* [10^{-7}]	3.56	-2.93
α_y^* [10^{-6}]	-1.78	0.079
D_x^* [10^{-6} m]	4.48 10^{-5}	7.83

Table 5.4: Sextupole strengths after nonlinear optimization for the two optics configurations $L^* = 3.51$ m and $L^* = 4.5$ m

L^* [m]	SD0	SF1	SD4	SF5	SF6
	k [m^{-3}]	k [m^{-3}]	k [m^{-3}]	k [m^{-3}]	k [m^{-3}]
3.51	7.219	-4.810	3.151	-0.434	1.615
4.50	6.515	-5.914	2.920	-0.406	1.458

The optimization is done order by order until the beam size reaches the target value.

In Fig. 5.2 the order by order beam size is shown after sextupole optimization. One can see that, although the $L^* = 4.50$ m has larger chromaticity, the final correction is better performed compared to the $L^* = 3.51$ m case. In any case, the final beam size less than 10% larger than the linear beam size given by $\sqrt{\epsilon_{x,y}\beta^*_{x,y}}$.

The final strength of the five sextupoles for both configurations is summarized in Table 5.4.

5.2.2 Tracking results

Tracking simulations are done using Placet taking into account synchrotron radiation effects in bending, quadrupole and other multipole magnets. The contribution from synchrotron radiation must be small enough to do not dilute the beam emittance and therefore the luminosity.

In Fig. 5.3 the transverse beam profile at the IP is plotted for the two optics configurations. One can see how it fits perfectly with a Gaussian distribution. This means that the beam is not seriously affected by synchrotron radiation or nonlinearities that might modify the distribution enlarging the tails of the beam. We can see that the core vertical beam size (1σ of the fitted Gaussian) is larger for the $L^* = 4.5$ m case but this effect is overcompensated by a 4% smaller horizontal beam size and this is reflected in a larger luminosity as it is explained in the next section.

5.2.3 Luminosity performance

As we have seen, luminosity is the final figure of merit of a collider and therefore the parameter that must be finally optimized. Luminosity simulations are done using GuineaPig [71] after a simulation of

Table 5.5: Total luminosity and peak luminosity for ILC with $L^* = 3.51$ m and $L^* = 4.50$ m.

L^* [m]	3.51	4.50
$\mathcal{L}_T[10^{34}\text{cm}^{-2}s^{-1}]$	1.38	1.54
$\mathcal{L}_{1\%}[10^{34}\text{cm}^{-2}s^{-1}]$	0.867	0.934

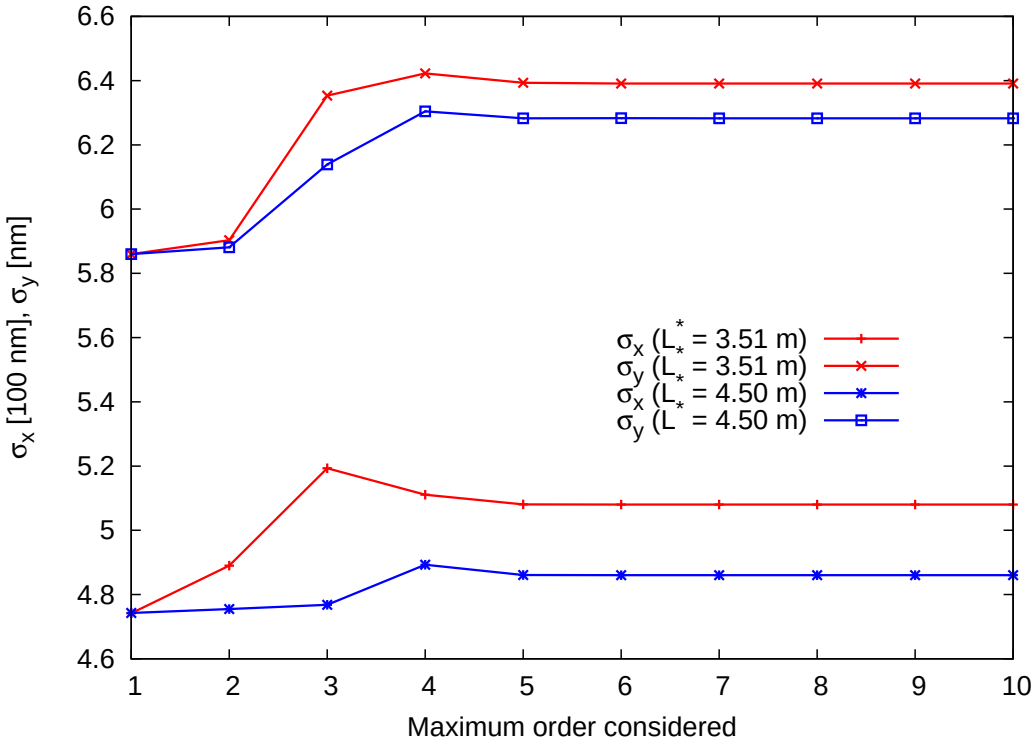

Figure 5.2: Nonlinear optimization of the ILC beam horizontal and vertical beam size for $L^* = 3.51$ m and $L^* = 4.50$ m.

the beam tracked through the Final Focus System with Placet [73].

In Table 5.5 the value of the total and peak luminosity for both configurations is shown. If we compare the value obtained with GuineaPig to the TDR value in Table 5.2 we see that for $L^* = 3.51$ m the value is below the nominal one by a 6% while the value for $L^* = 4.50$ m is above that value by almost a 5%. It is possible that the 3.51 m lattice needs further optimization using octupoles in order to reduce the beam size and increase the total and peak luminosities.

5.3 CLIC Final Focus System for ILC

Due to the synergies of the CLIC and ILC Final Focus Systems, it should be possible to use a common solution for both systems. Since the CLIC β^* are smaller than the ILC β^* we explore the possibility of using the CLIC FFS for ILC beam. The performance of such system after nonlinear optimization can be compared to the ILC FFS performance. In Fig. 5.4 a comparison of the nonlinear optimization for CLIC 500 GeV c.o.m. energy FFS lattice as ILC FFS, i.e. with ILC β^* values, and ILC $L^* = 3.51$ m option. One can see that the CLIC FFS performance is better, delivering smaller beam sizes. Exact values for core beam sizes and total and peak luminosity are shown in Table 5.7. A substantial reduction of the core beam size can be observed and it is translated in a total luminosity gain of almost 6%. Notice that the luminosity delivered by this system fulfills the requirements shown in Table 5.2, not fulfilled by the ILC FFS. The total length of the system is about 180 m shorter for the CLIC-based Final Focus System. This length reduction might also imply a cost reduction.

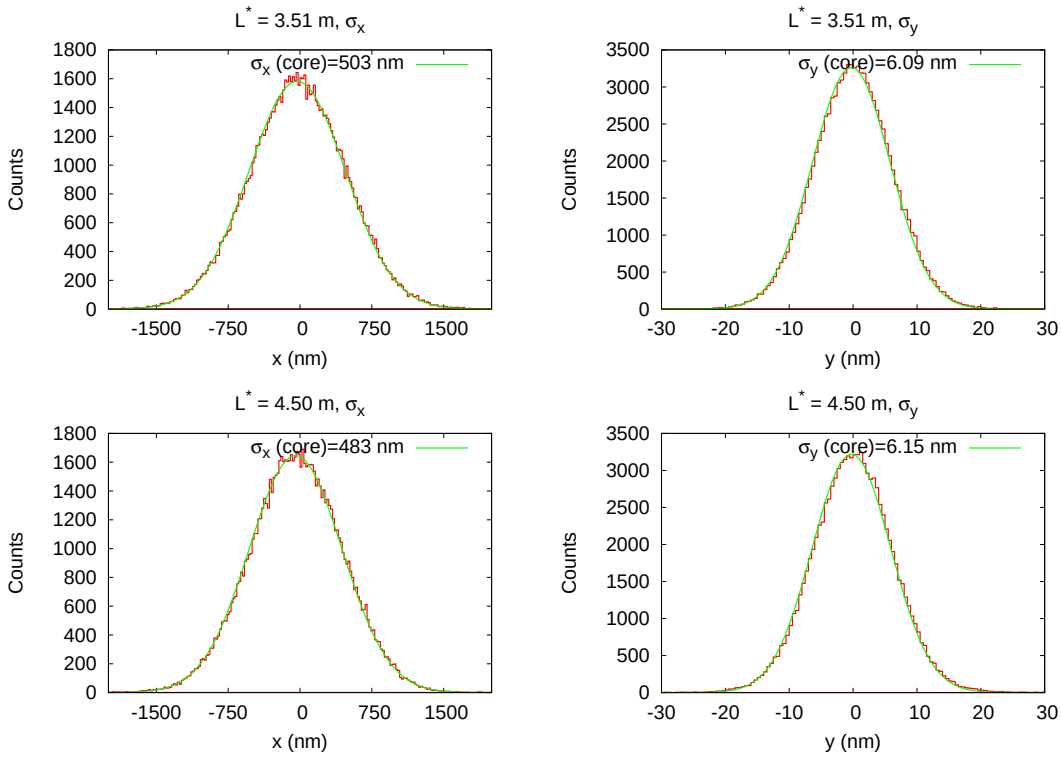

Figure 5.3: Transverse beam profile and Gaussian fit for both optics configurations $L^* = 3.51$ m (top) and $L^* = 4.5$ m (bottom).

Table 5.6: Final doublet comparison for ILC lattices and CLIC-based lattice

QD0

	L^*	L_{quad}	β_x	β_y	$KL_{\text{quad}}[\text{m}^{-1}]$
ILC	3.51	2.2	2247	37776	-0.167
ILC	4.50	2.2	3285	56318	-0.152
CLIC	4.30	3.35	9387	62914	-0.129

QF1

	L^*	L_{quad}	β_x	β_y	$KL_{\text{quad}}[\text{m}^{-1}]$
ILC	3.51	2.0	37583	16156	0.072
ILC	4.50	2.0	32017	26206	0.080
CLIC	4.30	4.0	69747	20642	0.054

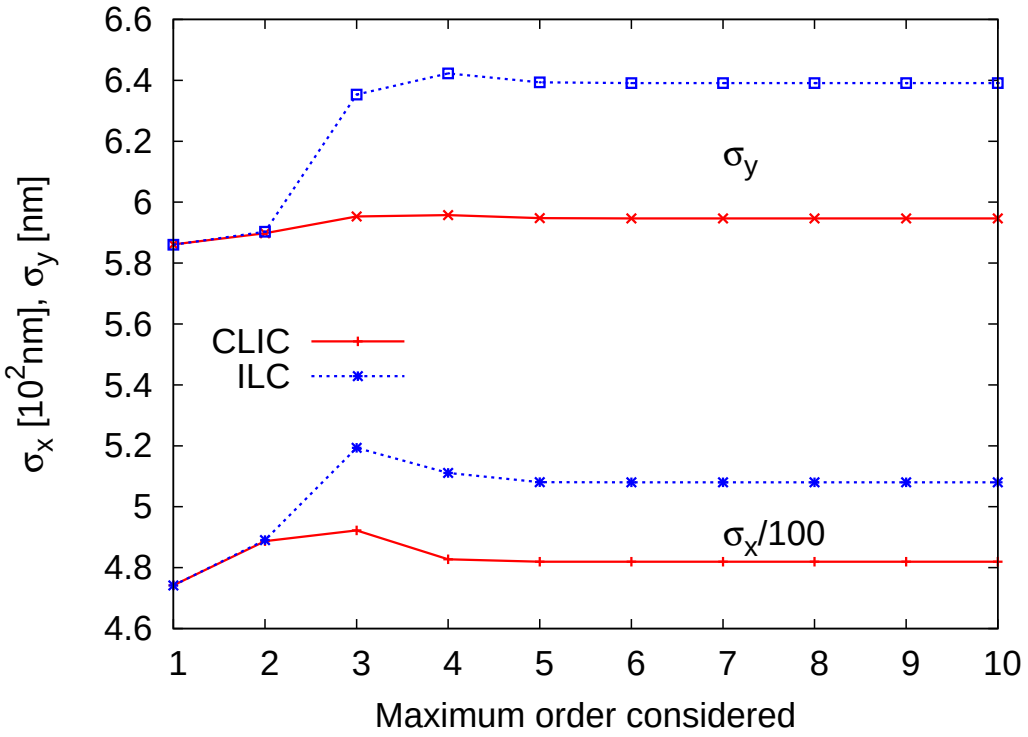

Figure 5.4: Beam size at different orders for ILC beam using the CLIC and ILC ($L^* = 3.51$ m) Final Focus lattices.

Table 5.7: Beam size and luminosities comparison for ILC and CLIC-based Final Focus lattices.

Parameter	ILC	CLIC-based
Length [m]	735	553
β_x^*/β_y^* [mm]	11/0.48	11/0.48
σ_x^{core} [nm]	503.0	483.7
σ_y^{core} [nm]	6.09	5.89
$\mathcal{L}_T$ [$10^{34}\,\text{cm}^{-2}\text{s}^{-1}$]	1.38	1.47
$\mathcal{L}_{1\%}$ [$10^{34}\,\text{cm}^{-2}\text{s}^{-1}$]	0.86	0.89

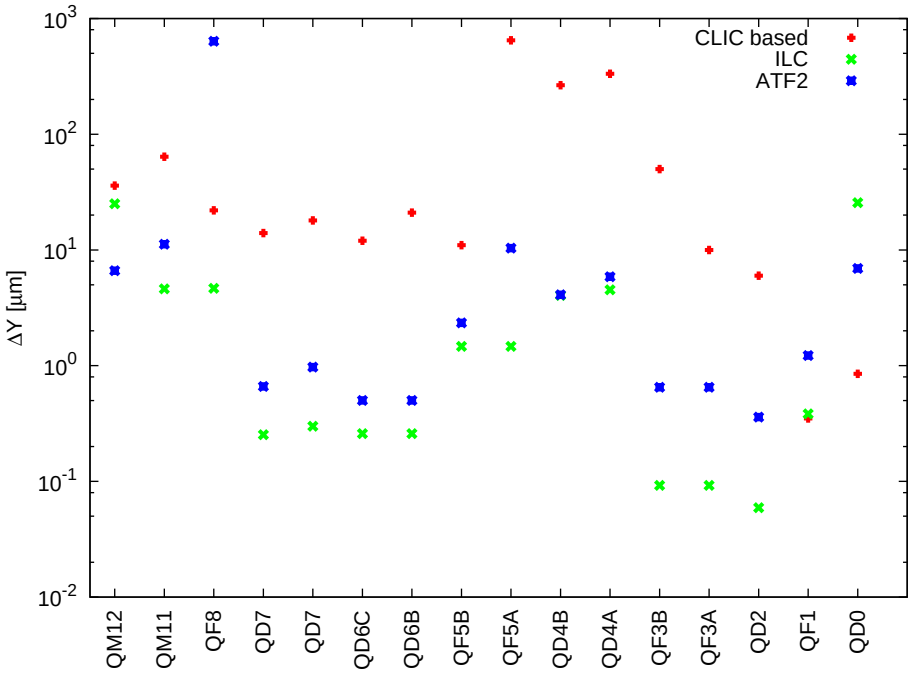

Figure 5.5: Alignment tolerances for CLIC-based, ILC and ATF2 quadrupoles.

5.3.1 Tolerances

If we consider the CLIC FFS lattice as an option for the ILC FFS one has to consider that the alignment and magnetic field quality tolerances may change. In Fig. 5.5 and Fig. 5.6 a comparison of the tolerances in quadrupole static alignment and quadrupole field sensitivity for ILC, CLIC-based lattice and ATF2 FFS is shown. These tolerances correspond to the values that give an increase of the beam size of 2%. We can observe that the tolerances on the alignment seem to be more relaxed for the CLIC-based lattice except for the Final Doublet. The magnetic field tolerances are in general also more relaxed for the CLIC-based lattice except for some magnets like QD2, but the value is similar to that of ILC.

5.4 Traveling focus

The traveling focus was first introduced by Balakin in [75] with the aim to increase the luminosity of the VLEPP linear collider. In head on collisions there is a unique and static focal point where the beam reaches its minimum size (waist) and the collision probability is maximum. Since the beam has a certain length, namely σ_z, some slices of the beam will collide out of the IP reducing its luminosity due to the fact that the beam size at these locations is always larger than at the IP. In the traveling focus scheme the focal point for the different slices is at different longitudinal positions. Usually the position to which a given slice is focused is chosen to coincide with the collision of that slice with the center of the other beam. So each slice will have its smallest size in the very moment when it collides with this specific slice of the other beam. The focusing beam-beam force will then keep the size of this slice small. Usually the focal point is $1\sigma_z$ before the center of the oncoming bunch, also called waist shift. In the case of a traveling focus, the optimum waist position is close to the center of the collision.

Due to the mutual attraction of the bunches explained above in the IP region, there exists an extra focusing of the beams. Due to this effect, the optimal focal point is changed. The focal point can be changed introducing a waist shift. The waist shift w_y, is a shift in the vertical plane in this case, that changes the focal point. This parameter can be adjusted varying the QD0 strength. The waist shift

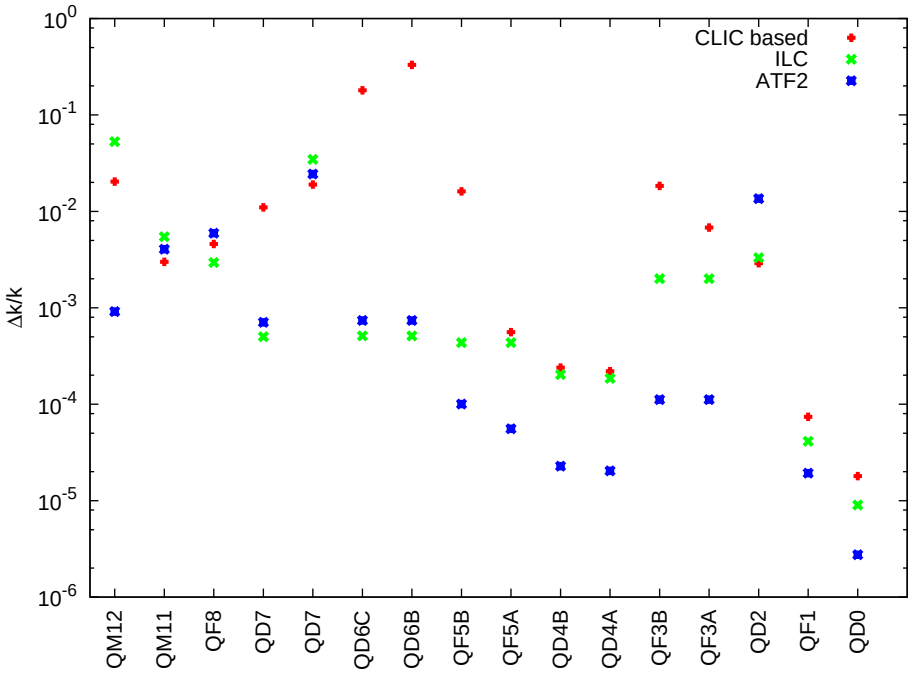

Figure 5.6: Magnetic field jitter tolerances for CLIC-based, ILC and ATF2 quadrupoles.

together with the pinch effect when the two beams approach each other, increases the overall luminosity. The traveling focus described above is given by the parameter $\partial w_y/\partial z$. This parameter introduces a displacement of the waist along the bunch increasing the effectiveness of the collision and consequently the luminosity is increased [76]. This effect is introduced by crab cavities and sextupoles following the expression,

$$\frac{\partial w_y}{\partial z} = -\beta_y^* \sum_i^{\text{sext}} \sum_j^{\text{CC}} R_{12}^{\text{CC}_j - \text{sext}_i} \xi_c \beta_{y_i} K_{s_i} L_{s_i}, \tag{5.1}$$

where β_y^* is the vertical beta function at the IP, $R_{12}^{\text{CC}_j-\text{sext}_i}$ is the matrix element between the crab cavity and the different sextupoles and β_{y_i}, K_{s_i} and L_{s_i} are the vertical beta function at the sextupole location, the sextupole strength and length respectively. The parameter ξ_c is given by,

$$\xi_c = \frac{\omega_{\text{rf}} q}{c} \frac{V_{\text{CC}}}{E_0} \tag{5.2}$$

where ω_{rf} is the rf frequency, c the speed of light, q the particle charge, V_{CC} the crab cavity voltage and E_0 the nominal energy.

5.4.1 Traveling focus implementation

Before considering the implementation of the traveling waist in CLIC or ILC lattices the study with ideal distributions (distributions not affected by nonlinear aberrations introduced by the FD) the potential of this scheme is computed. This allows to obtain an estimation of the traveling focus impact on the final luminosity and also to estimate the traveling waist $\partial w_y/\partial z$ and waist shift w_y needed for a later implementation in the FFS. This idea has been explored for CLIC at 3 TeV c.o.m. in [76].

Initially taking head-on distributions at the IP we transform the vertical coordinate following the relation,

$$y = y_0 + \frac{\partial w}{\partial z} z_0 y_0' + w_y y_0'. \tag{5.3}$$

Adjusting the two free parameters $\partial w_y/\partial z$ and w_y an optimal correlated distribution can be found. Concretely, for the w_y parameter, this is expected to be comparable to the bunch length σ_z as it has been demonstrated in [77] if we do not consider further effects.

We focus the study in the CLIC FFS for ILC, that means, ILC beam running through the CLIC FFS lattice. First of all and to cross check the results obtained in Fig. 5.7 a CLIC lattice configuration with $\beta_x^* = 9.52$ mm and $\beta_y^* = 0.6$ mm is considered. For this lattice configuration and head on collision we obtain $\mathcal{L}_T = 1.8 \cdot 10^{34}\,\mathrm{m}^{-2}$ per bunch crossing. In Fig. 5.8 luminosity is shown as a function of these two parameters. After scanning of $\partial w_y/\partial z$ and w_y the following values are found to give a maximum luminosity,

$$\frac{\partial w_y}{\partial z} = 0.4, \quad w_y = 300\,\mu\mathrm{m}, \tag{5.4}$$

where we see that the waist shift is exactly the bunch length. For these values, the luminosity with the traveling focus scheme is $\mathcal{L}_T = 2.48 \cdot 10^{34}\,\mathrm{m}^{-2}$ representing a gain of about 55% with respect to the nominal value.

The next step is to introduce the traveling focus parameters into a realistic lattice. The waist shift w_y can be adjusted varying slightly the strength of QD0 following the relation,

$$w_y = -\alpha^* \beta_y^* \tag{5.5}$$

and

$$\frac{\Delta K_{\mathrm{QD0}}}{K_{\mathrm{QD0}}} = \frac{w_y}{\sqrt{\beta_y^{\mathrm{QD0}} \beta_y^*}}. \tag{5.6}$$

Scanning the QD0 strength we find the maximum gain is found to be for $\Delta K_{\mathrm{QD0}}/K_{\mathrm{QD0}} = 3.0 \cdot 10^{-5}$ that corresponds to $w_y = 216\,\mu$m. The value of the traveling waist $\frac{\partial w}{\partial z}$ is mainly determined by the exact location of the single crab cavity since its value depends on the distance to the IP. The optimal position is found to be located between the last bend and SF5 with a value $\frac{\partial w}{\partial z} = 0.329$. Once the crab cavity and QD0 strength are set to the optimal, the luminosity per bunch crossing is,

$$\mathcal{L}_T = 2.43 \cdot 10^{34}\,\mathrm{m}^{-2}, \quad \mathcal{L}_{1\%} = 1.43 \cdot 10^{34}\,\mathrm{m}^{-2} \tag{5.7}$$

which represents a 50% gain with respect to the head on collisions and are in agreement with the prediction of the ideal scan shown using ideal distributions.

5.4.2 Traveling focus optimization

In the previous section the traveling focus has been applied to the ILC beam with a CLIC-based β-functions at the IP but, as Fig. 5.7 shows, the β_y^*-function is too low and hourglass effect reduces luminosity. A more optimal value for the vertical β-function at the IP is $\beta_y^* = 0.25$ mm keeping the value of $\beta_x^* = 9.00$ mm. The head-on total and peak luminosities per bunch crossing in this new configuration are,

$$\mathcal{L}_T = 2.54 \cdot 10^{34}\,\mathrm{m}^{-2}, \quad \mathcal{L}_{1\%} = 1.45 \cdot 10^{34}\,\mathrm{m}^{-2}, \tag{5.8}$$

that is already above the nominal ILC luminosity even before the traveling waist implementation. To introduce the crab cavity the same procedure described above is followed. The voltage needed is $V_{\mathrm{CC}} = -0.38$ MV and it is located in between QD2 and QF1 that corresponds to a traveling waist parameter of $\frac{\partial w}{\partial z} = 0.35$. To create a $1\sigma_z$ waist shift a change in the QD0 strength of $\Delta K/K = 5 \cdot 10^{-6}$ is required. With these parameters the final luminosities per bunch crossing are,

$$\mathcal{L}_T = 3.07 \cdot 10^{34}\,\mathrm{m}^{-2}, \quad \mathcal{L}_{1\%} = 1.74 \cdot 10^{34}\,\mathrm{m}^{-2}, \tag{5.9}$$

or in terms of luminosity taking into account the number of bunches and the revolution frequency,

$$\mathcal{L}_T = 2.01 \cdot 10^{34}\,\mathrm{cm}^{-2}\mathrm{s}^{-1}, \quad \mathcal{L}_{1\%} = 1.14 \cdot 10^{34}\,\mathrm{cm}^{-2}\mathrm{s}^{-1}, \tag{5.10}$$

that represents more than a 20% luminosity gain with respect to the nominal value shown in Table 5.2.

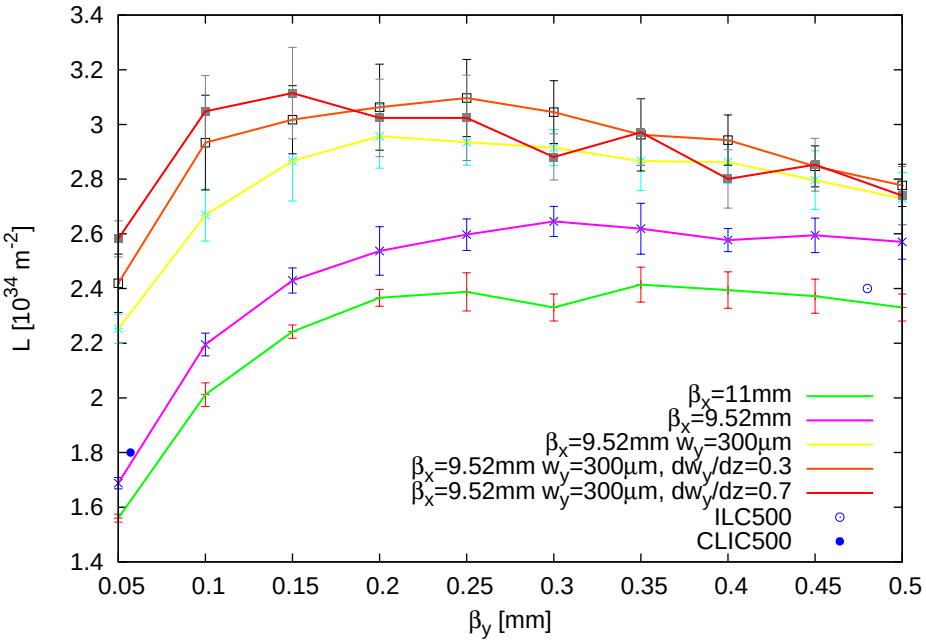

Figure 5.7: Total luminosity per bunch crossing for different values of β_x^* and β_y^* and different values of the waist shift z_w and traveling waist dw. CLIC and ILC nominal points are also represented.

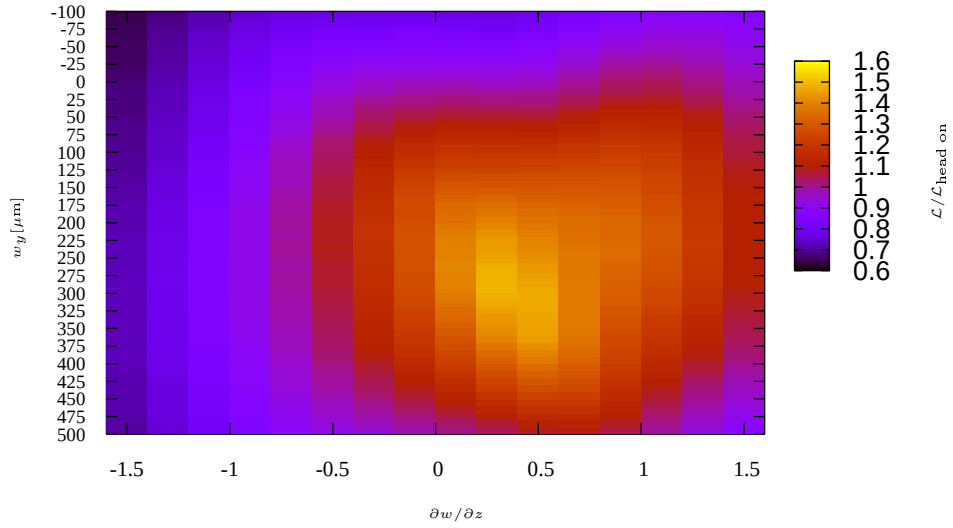

Figure 5.8: Traveling waist parameter scan

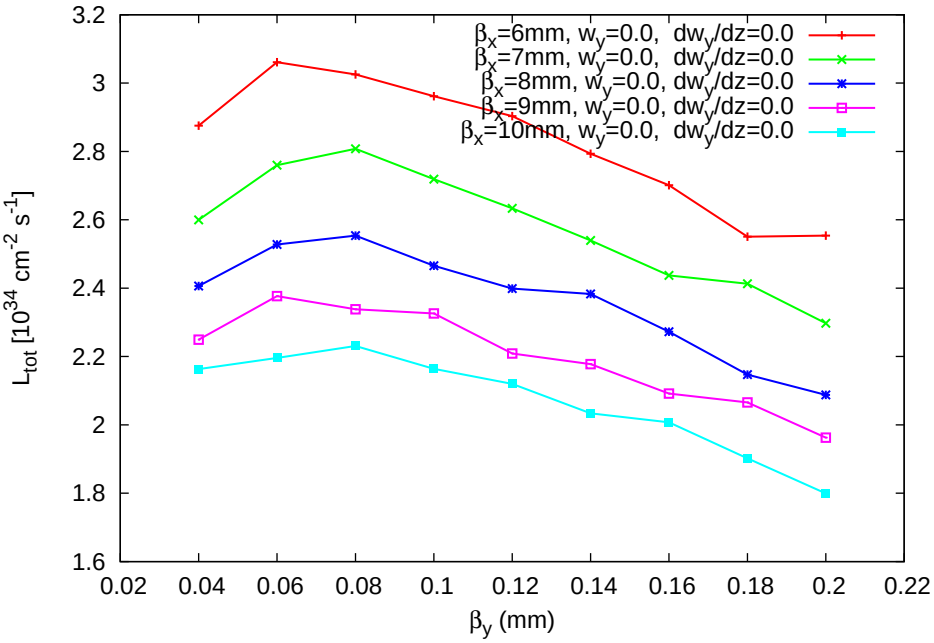

Figure 5.9: Total luminosity for different β_x^* and β_y^*.

5.4.3 Possible implementation of traveling focus in CLIC at 500 GeV c.o.m. energy

It is shown in Table 5.2 that the bunch length of the CLIC beam is much smaller than the ILC one and therefore the traveling waist has almost no effect on the luminosity gain if we consider current configuration of the FFS. Nevertheless, if we reduce the vertical β-function at the IP to make it comparable to the bunch length ($\sigma_z = 72\,\mu$m) this effect might become important. The problem arises when the beam quality is reduced due to beamstrahlung emission when the horizontal beam size is small enough. A compromise needs to be found in order to get a notable effect due to the traveling focus scheme without reducing the beam quality drastically. In Fig. 5.9 the total luminosity is scanned for different values of β_x^* and β_x^*. If we consider a $\beta_x^* = 9$ mm the maximum effect is obtained for $\beta_y^* = 0.06$ mm with a 10% luminosity gain coming mostly from the waist shift as it is shown in Fig.5.10 (top). For $\beta_x = 4$ mm (Fig. 5.10 (bottom)) a similar result is found, where almost all the luminosity increase is also due to the waist shift.

5.5 Conclusions

In this chapter we have explored different facts of the ILC Final Focus System. A reoptimization of the system has been carried out to fulfill the new requirements for two different $L^* = 3.51$ m and $L^* = 4.5$ m. The results are in agreement with the nominal requirements. We have also explored the possibility of introducing a traveling waist in the ILC collisions. We have demonstrated that a gain of about 20% in luminosity can be achieved although most of this gain comes from the effect of the waist shift. If we reduce the β^* functions at the IP, an even larger gain is achieved. Finally we have explored the possibility of introducing a traveling focus for CLIC at 500 GeV. The results show that the gain in luminosity is smaller than the previous case also being the waist shift the effect with the larger contribution.

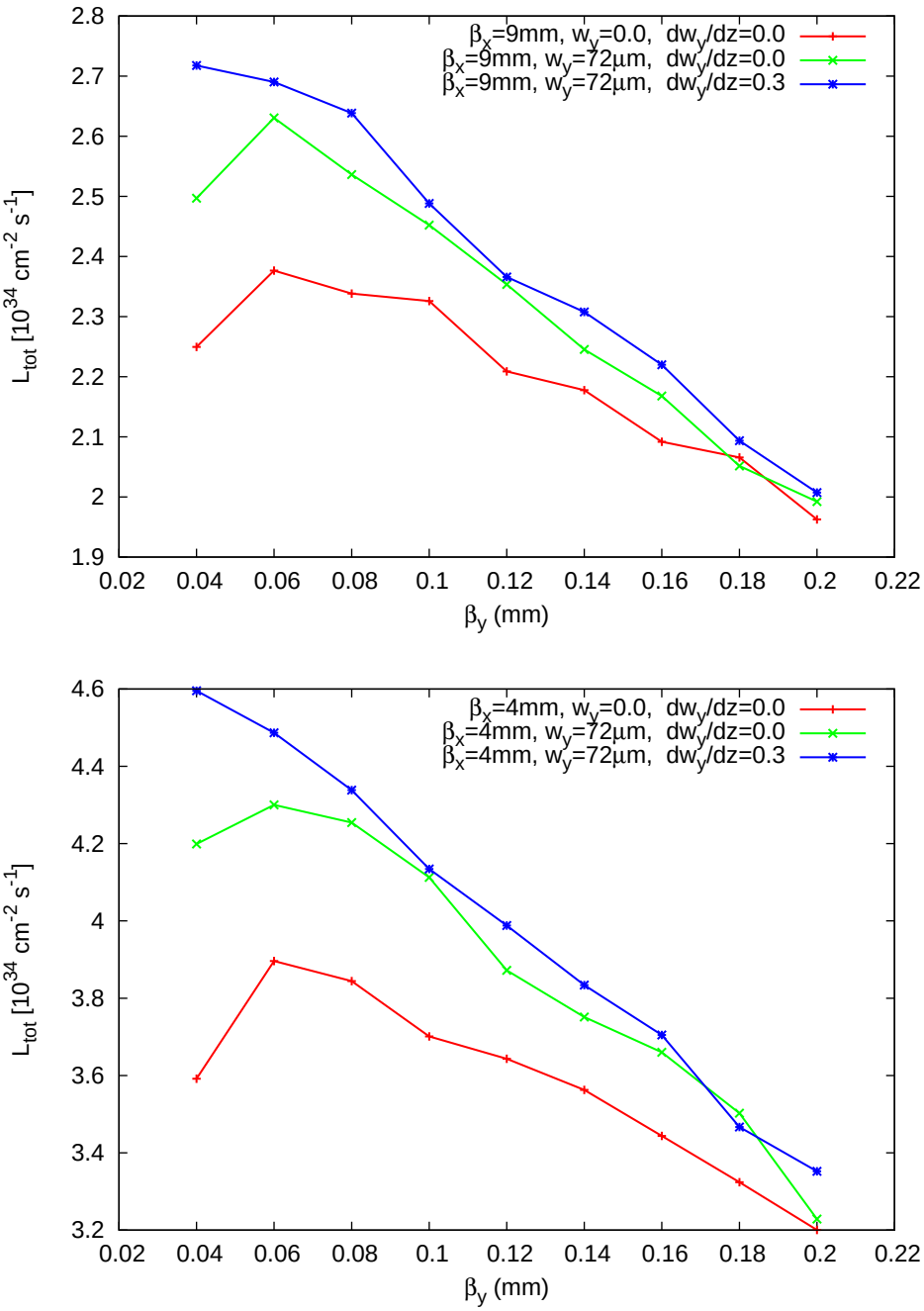

Figure 5.10: Ideal traveling focus implementation for two different horizontal β_x^*-functions ($\beta_x^* = 9$ mm (top) and $\beta_x^* = 4$ mm (bottom) for different β_y^* for CLIC at 500 GeV c.o.m. energy.

Conclusions

It has been demonstrated that optimized traditional designs of the optics configuration of the FFS, like the one used in FFTB and currently considered in Super-KEKb, are easier and faster to tune than the baseline design based on the local chromatic correction scheme, for CLIC at high energies (3 TeV). A faster tuneability translates into a larger integrated luminosity devoted to physics. The drawback is that such systems are relatively longer than the local scheme by about 1 km, thus increasing the cost of the tunnel and the accelerator. At 500 GeV c.o.m. energies, a similar performance of both designs is expected. These studies have opened the door to the reconsideration of such reoptimized traditional systems. [1]

Studies concerning the reduction of the horizontal β-function at the IP for CLIC at 500 GeV reveal that the design parameters are flexible to adopt even lower optical functions at the IP. Also, if intermediate stages at lower energies (350 GeV) are considered, a reduction of the horizontal β-function is possible and it is useful to avoid luminosity reduction due to the energy decrease.

An optimization of the ILC FFS has been performed at its nominal energy (500 GeV). In this optimization it has been considered the possibility of using CLIC FFS design for ILC and it can be observed an important increase of performance due to a more exigent configuration. This is translated into a tighter tolerances in the Final Doublet. Moreover, the implementation of the traveling focus for the ILC has also been explored. The results reveal that reducing the β-functions at the IP with respect to the nominal values, a luminosity gain of about 20% is observed, mostly coming from the effect of the waist shift. The implementation of the traveling focus for CLIC at 500 GeV using ideal distributions shows that, due to the shorter bunch length, the luminosity gain would be of about 10% mostly due also to the waist shift.

Bibliography

[1] H.Garcia and R.Tomas, "Final-focus systems for multi-TeV linear colliders", Phys. Rev. ST Accel. Beams 17, 101001 (2014).

[2] CMS Collaboration, "A New Boson with a Mass of 125 GeV Observed with the CMS Experiment at the Large Hadron Collider", Science Vol. **338** (2012).

[3] ATLAS Collaboration, "A Particle Consistent with the Higgs Boson Observed with the ATLAS Detector at the Large Hadron Collider", Science Vol. **338** (2012).

[4] J.Garra, private communication (2013).

[5] LHCb Collaboration, Phys.Rev.Lett. **110**, 2, (2013)

[6] S.Kraml, "SUSY status after one year of LHC", arxiv:1206.6618v1[hep-ph] ,(2012)

[7] G.Feldman, "Prospects Physics at e^+e^- Linear Colliders", SLAC-PUB-4563 (1988).

[8] J.T.Seeman "The Stanford Linear Collider", SLAC-PUB-5607 (1991).

[9] J.Ellis, "The Physics Prospects for CLIC", arxiv:0811.1366v1, (2008).

[10] "Physics at the CLIC multi-TeV Linear Collider" arXiv:hep-ph/0412251v1, (2004)

[11] G.Guignard, "A 3TeV e^+e^- Linear Collider Based on CLIC Technology", CERN 2000-008,(2000)

[12] CLIC Conceptual Design Report, http://project-clic-cdr.web.cern.ch/project-CLIC-CDR/ (2012).

[13] R.Tomás, "Overview of the Compact Linear Collider", Phys.Rev. STAB, **13**, 014801, (2010).

[14] Nan Phinney, Nobukasu Toge, Nicholas Walker, et al., "ILC Reference Desing Report", https://www.linearcollider.org/ILC/Publications/Reference-Design-Report, (2007)

[15] T. Behnke et al. "The International Linear Collider Technical Design Report", arXiv:1306.6327, (2013).

[16] R.Corsini, "Experimental verification of the CLIC two-beam scheme, status and outlook", CLIC-Note-962 (2012).

[17] R.Ruber et al. "The CTF3 Two-beam Test Stand ", Nucl.Instr.Meth.A. 729, (2013).

[18] P.Tenenbaum, "The Final Focus Test Beam", Beam Line (Spring 1995).

[19] V. Balakin et al., Phys. Rev. Lett. **74**, 13 (1995).

[20] D.Burke, "Results from the Final Focus Test Beam", SLAC-PUB-6609, (1994).

[21] K.Oide, "Design optics for the Final Focus Test Beam at SLAC", SLAC-PUB-4953 (1989).

[22] http://atf.kek.jp

[23] Y.Honda, Phys. Rev. Lett. **92**, 054802, (2004).

[24] ATF2 Proposal Vol-1, ATF2 Group, http://lcdev.kek.jp/ATF2/proposal/ATF2proposal1.pdf . August 2005 (Revised 2006)

[25] P.Raimondi and A.Seryi, "Novel Final Focus Design for Future Linear Colliders", Phys. Rev. Lett. **86**, 3779 (2001).

[26] G.White et al,. "Experimental validation of a novel compact focusing scheme", Phys.Rev.Lett. **112**, 034802 (2014).

[27] K.Kube and ATF2 collaboration, "Towards and International Linear Collider: Experiments at ATF2", IPAC14 (2014).

[28] S.Kuroda and ATF2 collaboration, "ATF2 for Final Focus Test Beam for Future Linear Colliders", talk on ICHEP14, (2014).

[29] H.Wiedemann, "Particle Accelerator Physics", Springer, (2007).

[30] J.Irwin, "The Application of the Lie Algebra Techniques to Beam Transport Design", SLAC-PUB-5315, (1990)

[31] A.Chao, "Lie algebra techniques for Nonlinear Dynamics", USPAS lecture notes (2012).

[32] F.Zimmermann, R.Helm, J.Irwin, "Optimization of the NLC Final Focus System", SLAC-PUB-6791, (1996)

[33] T.O. Raubenheimer, F.Zimmermann, "Final Focus systems in linear colliders", Rev.Mod.Phys.**77**, 1, (2000).

[34] K.Oide, "JLC Final Focus System", KEK Preprint 89-190 (1990).

[35] A.Seryi, "VLEPP Final Focus System" Proceedings LC90 (1990).

[36] T.Raubenheimer et al. "Zeroth order design report for the Next Linear Collider", SLAC-R-474 (1996).

[37] O. Napoly, B. Zotter, "Progress report on the CLIC final focus design", (1990).

[38] A.Seryi, M.Woodley, P.Raimondi, "A recipe for Linear Collider Final Focus System Design", RPAB018, PAC13 (2013).

[39] A. Chao and M. Tigner. "Handbook of Accelerator Physics and Engineering", World Scientific (1999).

[40] K.Yokoya, P.Chen, "Beam-beam phenomena in Linear Colliders", (1991).

[41] O.Blanco, R.Tomás and P.Bambade, "CLIC 3TeV Beamsize Optimization with Radiation Effects", CLIC-Note-1014 (2014).

[42] K. Oide, "Synchrotron-Radiation Limit on the Focusing of Electron Beams", Phys. Rev. Lett. **61**, 1713-1715 (1988).

[43] M.G.Minty, F.Zimmermann, “Measurement and control of charged particle beams”, Springer, (2003).

[44] R.Assmann et al. "Quadrupole alignment and trajectory correction for future linear colliders", SLAC-PUB-10485, (1995).

[45] O.Napoly, B.Dunham, "FFADA: Computer Design of Final Focus Systems for Linear Colliders", EPAC'94 (1994).

[46] MAD-X, http://mad.web.cern.ch/mad/.

[47] R.Tomas, "Nonlinear optimization of beam lines", Phys.Rev. STAB **9**, 081001 (2006).

[48] R.Tomas, "MAPCLASS : a code to optimize high order aberrations", CERN-AB-Note-2006-017, (2006).

[49] Martínez D. et al, "MAPCLASS2: a code to aid the optimisation of lattice design",CERN-ATS-Note-2012-087 TECH, (2012).

[50] "Summary of the BDS and MDI CLIC08 working group", CLIC-Note-776, (2008).

[51] E.Marin, "Design and higher order optimisation of Final Focus Systems for Linear Colliders", PhD Thesis, Universitat Politècnica de Catalunya, Barcelona, 2012; CERN-THESIS-2012-218 (2012).

[52] E.Forest et al, Introduction to the PTC Code, KEK Report 2002-3. (2002).

[53] `http://clicr.web.cern.ch/CLICr/MainBeam/BDS/Traditional_3TeV/`

[54] `http://clicr.web.cern.ch/CLICr/MainBeam/BDS/Traditional_500GeV/`

[55] R.Brinkmann, "Optimization of the Final Focus System for Large Momentum Bandwidth", DESY-M-90-14, (1990).

[56] K.Oide, "Final focus system with odd dispersion scheme", Int.J.Mod.Phys.Proc.Suppl. A2 (1993).

[57] `http://clicr.web.cern.ch/CLICr/MainBeam/BDS/`

[58] `http://clicr.web.cern.ch/CLICr/MainBeam/BDS_500GeV/Nominal500GeV.dis_CDR/`

[59] M.Modena, "Magnet Studies", CLIC Workshop, (2014).

[60] F.Zimmermann et al., "A Final Focus System for the Next Linear Collider", SLAC-PUB-6789, (1995).

[61] N.J.Walker, J.Irwin and M.Woodley, "Global tuning knobs for the SLC final focus",*Presented at the 1993 Particle Accelerator Conference (PAC 93): Washington DC, 17-20 May 1993.*

[62] Y.Nosochkov, P.Raimondi, T.O.Raubenheimer, A.Seryi, M.Woodley, “Tuning Knobs for the NLC Final Focus”, EPAC’02 Paris (2002).

[63] D.Schulte, private communication (2013).

[64] G.White, "ATF and LC FFS tuning", ECFA LC13 (2013).

[65] B. Dalena et al., "Beam delivery system tuning and luminosity monitoring in the Compact Linear Collider", Phys.Rev.STAB, **15** (2012).

[66] B. Dalena et al., Erratum on [65] to be submitted to PRSTAB.

[67] H.Mainaud, "Pre-alignment status", ECFA LC13 (2013).

[68] J. Pfingster et al., "Ground motion optimized orbit feedback design for the future linear collider" , Nucl. Ins. and Meth. A. 703, (2013).

[69] A.Latina, "A Novel Alignment Procedure for the Final Focus of Future Linear Colliders", LINAC10, (2010).

[70] V.A.Alexandrof et al. "Results of Final Focus Test Beam", KEK-95-31 (1996).

[71] D.Schulte, "Study of Electromagnetic and Hadronic Background in the Interaction Region of the Tesla Collider", Ph.D thesis DESY/Universitat Hamburg, (1996).

[72] D.Schulte, "Beam-beam simulations with Guinea-Pig", CLIC-Note-387 (2002).

[73] D.Schulte, "Evolution of the tracking code PLACET", CERN-ACC-2013-0083 (2013).

[74] P.Raimondi et al., "Low emittance and final focus design for a SuperB project", SLAC-PUB-12716, (2007).

[75] V.E.Balakin, 3rd International Workshop on Linear Colliders (LC91), Protvino, USSR, (1991).

[76] J.Barranco, E.Marin, R.Tomás, "Luminosity studies in a crab cavity scheme in the CLIC Final Focus", Phys. Rev. ST Accel. Beams 16, 041001 (2012).

[77] D. Schulte and R. Tomas, ICFA Beam Dyn. Newslett. 52, 149 (2010)